Ancient TL

www.ancienttl.org · ISSN: 2693-0935

Issue 33(2) - December 2015
https://doi.org/10.26034/la.atl.v33.i2

ISSN 0735-1348

Ancient TL

A periodical devoted to Luminescence and ESR dating

Department of Physics, East Carolina University, 1000 East 5th Street, Greenville, NC 27858, USA
http://www.ecu.edu/cs-cas/physics/ancient-timeline/

December 2015, Volume 33 No.2

Comparison of DosiVox simulation results with tabulated data and standard calculations 1
Loïc Martin, Sébastien Incerti and Norbert Mercier

Evaluation of soil-moisture content for OSL dating using an infiltration model 10
Ravid Rosenzweig and Naomi Porat

Induced thermoluminescence dating of basalts 15
Derek W.G. Sears

Thesis abstracts 20

Bibliography 26

Announcements 51

Ancient TL

Started by the late David Zimmerman in 1977

Ancient TL

Comparison of *DosiVox* simulation results with tabulated data and standard calculations

Loïc Martin[1,*], Sébastien Incerti[2,3], Norbert Mercier[1]

[1]Institut de Recherche sur les Archéomatériaux, UMR 5060 CNRS - Université Bordeaux Montaigne
Centre de Recherche en Physique Appliquée à l'Archéologie (CRP2A)
Maison de l'archéologie, 33607 Pessac Cedex, France

[2]CNRS, IN2P3, CENBG, UMR 5797, 33170 Gradignan, France
[3]Université de Bordeaux, CENBG, UMR 5797, 33170 Gradignan, France

[*]Corresponding Author: loic.martin@u-bordeaux-montaigne.fr

Received: August 14, 2015; in final form: November 17, 2015

Abstract

The *DosiVox* software allows modeling various situations of dosimetric interest for trapped charge dating methods. Simulation of α-, β- and γ-dose rates are considered here in adapted modeling. The results of numerical simulations are compared with tabulated data of dose attenuation in layers and grains usually used in the dating community. Good agreements are found with the tabulated data, and some limits of usual approximations are highlighted.

Keywords: *DosiVox*, dose rate modeling, software, Geant 4

1. Introduction

DosiVox is a Geant4 based software for simulating dose rates in various contexts encountered in trapped charge dating methods. It is freely available[1] and has already been used in two studies: in the first one (Martin et al., 2015a) its features were illustrated by a series of selected examples, while in the second, Martin et al. (2015b) presented dose rate modeling of a complex sediment sample previously characterized by numerous analytical techniques. Meanwhile, considering the diversity of samples and dosimetric contexts that can be encountered in trapped charge dating and for which numerical simulations can be of interest to assess the effect of distinct parameters on the dose rates, it is difficult to evaluate the reliability of the modeling results because of the lack of comparative data. We propose in this paper to test *DosiVox* in dosimetric layouts described in the literature for which tabulated data are available. The relevance of the compared data will be discussed as well as the limits of the usefulness of these modelings.

[1]http://www.iramat-crp2a.cnrs.fr/spip/spip.php?article144

2. Procedure

The *DosiVox* software allows modeling samples by constructing a voxelised (3D) volume where the material and the associated radioactivity can be defined in each voxel. The emission of α-, β- and γ-particles from the natural radioactive elements can be simulated and the corresponding dose rates can be recorded by different detector types (Martin et al., 2015a). The software does not need any programming skills, all the parameters used to construct the simulation being defined with a "pilot" text file. For the purpose of this study, *DosiVox* version 1.03 was used. A new feature of particle reflection on the walls of the volume, not yet available in the online version of the software, was sometimes used in the simulations in order to speed them up and to increase the statistical counting. However, all the results reported here were first tested without this option, to ensure that it has no effect on the exactness of the results.

We propose to arrange this study in three parts, each of them considering a particular *DosiVox* detector type with its own utility and purpose. The simulations, results and discussions of each case are presented in the corresponding part for a better consistency.

In the first part, the dose rate profiles generated by a juxtaposition of layers differing by their radioactivity are investigated. The results concerning the γ-dose rates are compared to the data gathered by Aitken (1985). Simulations of the β-dose attenuation in a silica layer of variable thickness have been carried out in a similar way as Brennan (2006)'s calculations. At last, the attenuation of the α-dose rate in calcite layers calculated by *DosiVox* is compared to the data from Grün (1987). All these dose rates were recorded with the "Probe" detector of *DosiVox*, a detector composed of a cylinder crossing through the height of the modeled volume and divided in several parts, each one recording the dose deposits.

The second part explores the modeling of dose attenuation effects in sedimentary grains, using the grain packing detectors of *DosiVox*. These detectors were mainly set in an almost infinite matrix layout because the majority of the available data had been calculated for this situation. Both internal and external dose deposits were calculated for 100 μm grains using α- and β-radiations, and for 1 mm grains as well in the case of the β-particles. The results are compared to the tabulated data from Bell (1980), Guérin et al. (2012) and Martin et al. (2014). The effect of water content and matrix material are also briefly investigated in the case of the β-dose rate, for a comparison with Nathan & Mauz (2008) data. In addition, a test to check for the complementarity of the internal and external β-dose rates is presented for a packing of 400 μm grains.

The last part of the study focuses on the subvoxelised detector of *DosiVox* that allows detailing an object with a finer level of resolution. Voxelised sphere modelings were used for these tests because several data concerning the attenuation of dose in spherical volumes can be found in the literature, for α- (Bell, 1980; Martin et al., 2014) β- (Mejdahl, 1979; Fain et al., 1999; Guérin et al., 2012) and γ-radiations (Mejdahl, 1983; Aitken, 1985). The possibilities offered by *DosiVox* for visualizing the dose deposits are used to illustrate the kind of information that simulations can bring for apprehending dose rate distributions.

Some of the simulation results presented in this paper are normalized to the quantity of energy carried by the primary particles emitted by unit of mass (*EmMass*) in the material used as a reference. This value is homogeneous with a dose, and corresponds to the infinite matrix dose of the reference material. Meanwhile, as the main purpose of *DosiVox* is to investigate dose rates in cases which are far away from the infinite matrix case, the *EmMass* term can be considered more adapted to this context. Normalizing the dose results provided by the simulation by the *EmMass* term is a convenient way to proceed because it allows representing them as values relative to a calculable annual dose. This ratio (simulated dose divided by *EmMass*) is therefore proportional to a dose rate as it only requires to be multiplied by the corresponding specific annual dose of the radioelement present in the reference material, taken from Guérin et al. (2012) for instance.

3. Layer to layer variation

3.1. Variation of dose rate from a radioactive layer to an inert one

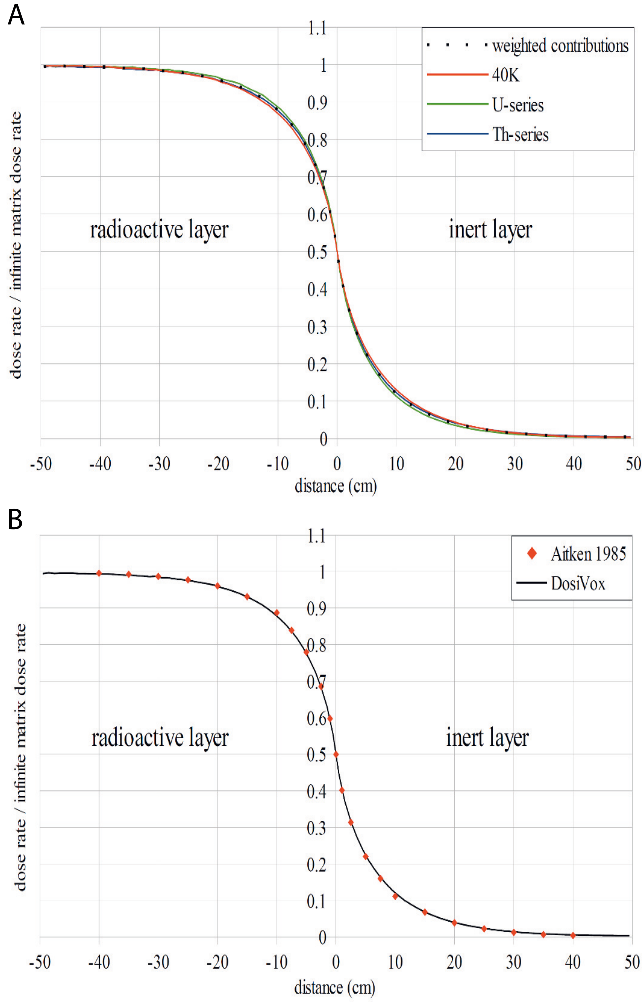

Figure 1. γ-dose rate in a radioactive layer next to an inert layer.

This first simulation layout is presented in appendix H of Aitken's book (Aitken, 1985). A radioactive layer of soil is next to an inert layer of an identical soil. The γ dose rate profile from the ^{40}K, U- and Th-series spectra are investigated at the interface of the two media. The different spectra are taken from the *DosiVox* data (Martin et al., 2015a), the decay chains of the U- and Th-series being in secular equilibrium. The chemical composition of the soil is taken from Aitken: O 50 %, Si 36 %, Al 6.9 %, Ca 0.5 %, Fe 3.5 %, Mg 0.4 %, K 1.5 %, Na 0.6 %, Ti 0.6 %. The dry soil density is 1.6 g cm^{-3}, and the moisture represents 25 % of the dry mass which leads to a total density of 2 g cm^{-3} for the moist sediment. Figure 1 shows the dose rate profiles of the γ emissions from the different spectra, and the weighted mean of their contribution for contents of 1 % in mass of K, 3 ppm of U and 10 ppm of Th (which corresponds to weights of 20 % for the ^{40}K dose rate, 30 % for the U-series and 50 % for the Th-series). These proportions were also used by Aitken (1985).

Aitken's results are represented on Fig. 1 for comparison.

We can observe that the results of the *DosiVox* simulations match very well the data from Aitken (1985). Few difference can be observed and likely result from the evolution of γ-spectra and cross section values since 1985.

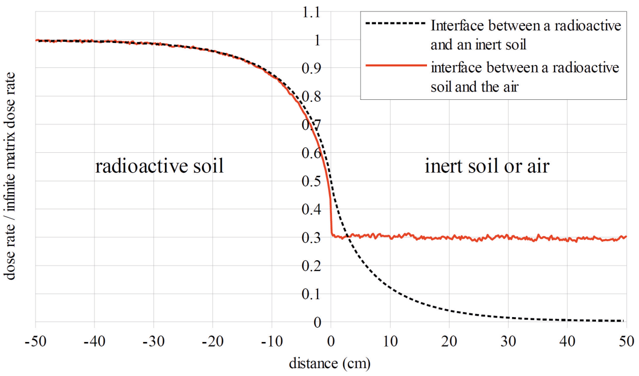

Figure 2. γ-dose rate next to the surface of a soil.

Aitken estimated that the curve part representing the dose rate in the radioactive layer (from -50 to 0 cm on the horizontal axis) could be used to calculate the dose rate at the surface of a soil, considering that the inert part is replaced by air. However, by replacing the one meter-thick inert soil layer, by an equal volume of air (N 78 %, O 22 %, density = 0.00129 g cm^{-3}, water content = 0 %), the *DosiVox* simulation result presented on Fig. 2 indicates a profile significantly different. The lower dose rate observed from -15 cm to 0 cm results from a lack of back-scattered γ-particles from the meter of air next to the soil, in comparison with the quantity of particles back-scattered by the inert soil in the previous simulation. The assumption of Aitken was yet not wrong because if a length of air superior to the γ-range in this material had been simulated, the back-scattered γ-particles in air would have compensated the lower dose rate in the first fifteen centimeters of soil. But in a real case of measurement, this back-scattered γ-flux is mixed with all the γ-rays coming from adjacent sediments, as they have a long range in air. Considering the very different ranges of the direct γ-self-irradiation of the soil and of the back-scattered particles in the air, it could be more pertinent to take in account separately these two contributions to the total γ-dose rate at the surface of the sediment.

We can observe in Fig. 1A that the Th-series γ-dose rate profile is very close to the weighted γ-dose rate profile. Therefore, the Th-series γ-spectrum will be used for the next simulations of γ-rays, because it is directly available in *DosiVox* and can be considered as representative of an average behavior of γ-radiations.

A similar situation is considered now for the β-dose rate, but we replaced the soil material by pure silica. This layout corresponds to the geometry considered by Brennan et al. (1997) for calculating β-dose rate attenuation in a silica layer of variable thickness. The silica material is composed of SiO_2 100% with a density of 2.65 g cm^{-3} and no moisture. The β-doses deposited in the inert layers for the ^{40}K, U-series and Th-series spectra are given in Fig. 3. The x-axis represents the thickness of the inert silica layer, and the dose rates are expressed as the percentage of the dose rate in an infinitely thin inert layer next to a radioactive one. These results were obtained by averaging the dose recorded in the segments of the "Probe" detector overlaying the inert part of the model for the considered thickness. The *DosiVox* results are compared with the data calculated by Brennan et al. (1997) using the ROSY software and the Monte-Carlo calculations of Cross et al. (1992), and with the data from Grün (1986) reported by Brennan et al. (1997) in his paper.

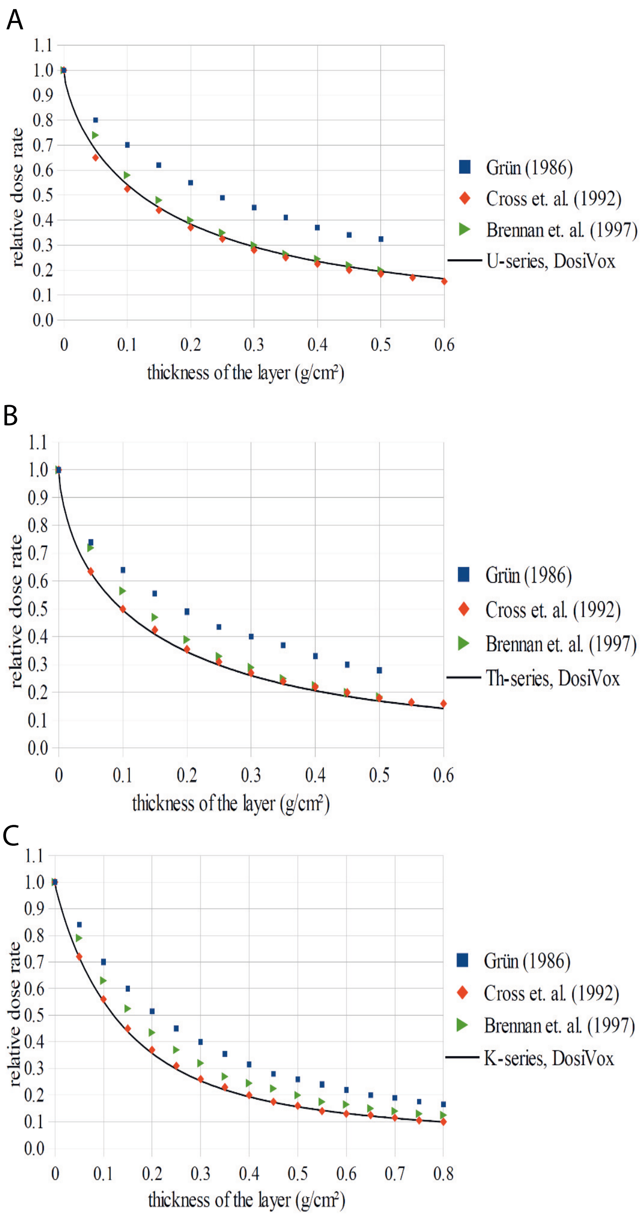

Figure 3. β-dose rate in a silica inert layer next to a radioactive layer

The *DosiVox* results are consistent with the data obtained by Brennan et al. (1997) by applying the table of Cross et al. (1992) on a silica medium. This agreement makes sense since as for *DosiVox*, the Cross tables were calculated using Monte-Carlo simulations and Brennan considered the different contributions of the natural β emitters.

A similar approach using planar geometries had been carried out by Grün (1987) for calculating the attenuation of α-dose rate in mollusc shells: a radioactive sediment next to a layer of calcite (representing the shell) had been studied. We reproduced these calculations using a similar modeling to the one used for the γ- and β-dose rate simulations, but in the present case, the radioactive part was filled with a typical dry clay sediment (SiO_2 54 %, Al_2O_3 46 %, density: 1.8 g cm^{-3}) and the inert part with pure calcite ($CaCO_3$, density: 2.7 g cm^{-3}). As previously, the dose rate in a layer of a particular thickness was calculated by averaging the dose recorded in the corresponding “Probe“ segments, and by dividing this number by the *EmMass* value of the sediment. The *DosiVox* results are compared to those of Grün (1987) in Fig. 4. The *DosiVox* dose rates follow the trend of Grün's results, and are in quite good agreement even if they are slightly lower. This small difference could be explained by a difference in the sediment composition or in the equations describing the interaction of α-particles with calcite at different energies.

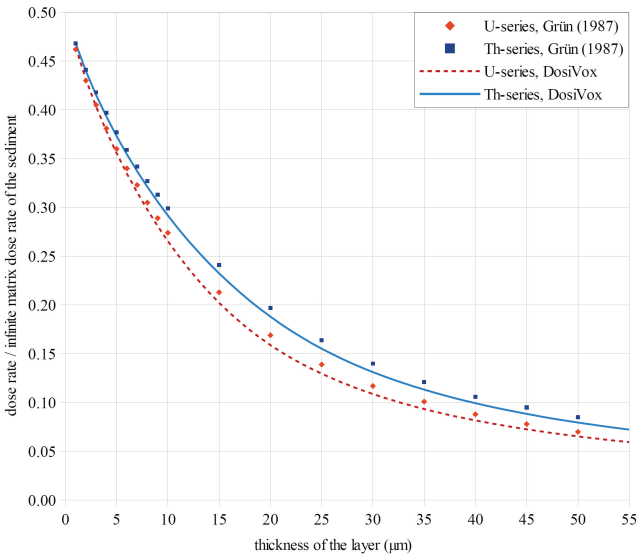

Figure 4. α-dose rate in a calcite inert layer next to a radioactive sediment layer.

3.2. γ-dose rate in a radioactive layer between two less radioactive media

We are now considering a little more complex layout of a soil layer sandwiched between two less radioactive media. This case was also presented by Aitken (1985) in the appendix H of his book: the internal layer was two times more radioactive than the surrounding soils. We considered two cases, when the internal layer is 4 cm thick and when it is 40 cm thick. The Th-series γ-spectrum was used, and the chemical composition, density and moisture of the soils are identical to those of section 1.1. The dose rate profiles were calculated separately for the internal layer and for the twice less radioactive soils, and are presented in Fig. 5. For both thicknesses, the sum of these two contributions are also indicated, as well as the data from Aitken. In the case of a 4 cm thick internal layer, a simulation in one shot of both the radioactivity of the layer and the surrounding soils was also carried out and the results are presented on Fig. 5A.

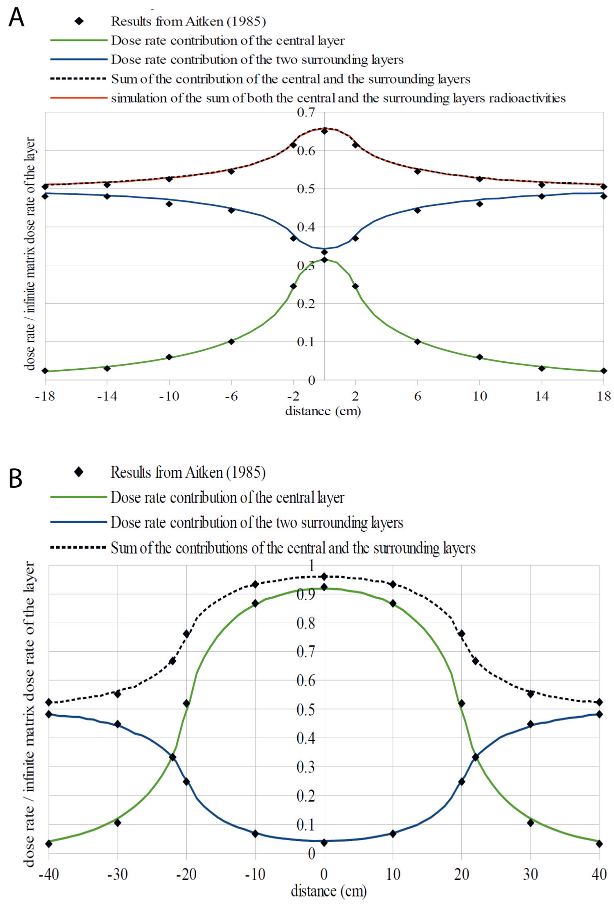

Figure 5. γ-dose rate in a layer between two soils having half as much radioactivity

As we can see, there is excellent agreement in both cases with the Aitken calculations. In the case of the 4 cm layer, the dose rate from the surrounding layers, and consequently the sum of the dose rates, is just a little bit lower compared to Aitken's data. This effect may be due to the use of the Th-series spectrum instead of a weighted spectrum resulting from a combination of ^{40}K, U- and Th-series spectra, but the difference is very small. We can also observe in this case that the sum of the dose rate from the two contributions perfectly matches the dose rate profile obtained by simulating in one shot both the radioactivities of the layers and of the two soils, suggesting that these two ways of calculation are consistent with each other. In other words, the principle of superposition of dose rates is conserved by *DosiVox*.

In addition to these dose rate profiles, Aitken (1985) also investigated the variation of the dose rate at the center of the layer, surrounded by non-radioactive levels, with its thickness. The results obtained for various thickness values with *DosiVox* are compared to Aitken's calculations in Fig. 6. These results are also in good agreement: only small differences can be observed, which may be caused by the use of only the Th-series spectrum, or to changes in the nuclear data since Aitken's publication.

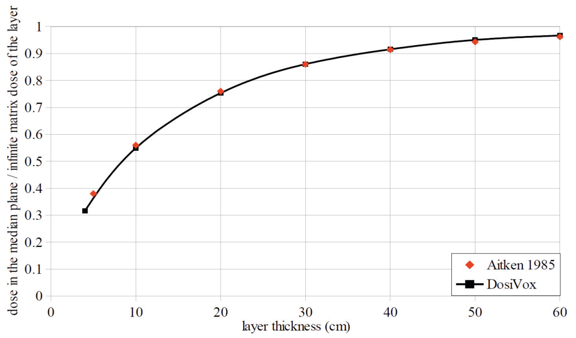

Figure 6. γ-dose rate in median plane of radioactive layer between two inert regions.

4. α- and β-dose rates in spherical grains

The sedimentary grains can be considered as the most frequently dated objects with paleodosimetric methods. We propose in this part to test the reliability of *DosiVox* for representing the dose rate affecting quartz grains in standard cases. Considering that the grain sizes usually used are significantly smaller than the mean range of the γ-rays (which limits the dosimetric effects that can be induced by the presence of grains), the following simulations are focused on the α- and β-dose rates only.

4.1. α- and β-dose rate in infinite matrix conditions

In most cases, a sedimentary grain is considered as a small heterogeneity in a uniform and infinite matrix. According to this model, the dose received by a grain depends on the infinite matrix dose rate (which is replaced by the *EmMass* in this study) corrected by an attenuation factor corresponding to its size (Fleming, 1970) and by the moisture of the surrounding matrix (Zimmerman, 1971). The self-dose of the grain can also be considered, but it is only affected by the size of the grain; this self-dose is then the exact complement of that of the matrix (because of the principle of superposition) if the grain and the matrix are made of the same components. This configuration has been reproduced in *DosiVox* by modeling a single grain, surrounded by a matrix that is uniform in terms of chemical composition, density, moisture and radioactivity. The grain self-dose and the dose from the matrix were calculated for different radiations and configurations. The volume of the model has been adapted in each case in order to have in all directions a matrix whose dimensions are larger than the maximum range of the particles considered in the medium.

The results of the α-dose rate simulation for the U- and Th-series spectra are shown in Fig. 7. The attenuation factors in a 100 μm diameter quartz grain for the self-dose and the dose from the matrix have been obtained by dividing the dose recorded in the grain by the *EmMass* values, respectively of the grain and the surrounding matrix. The grain is composed of SiO_2 with a density of 2.65 g cm^{-3}, which corresponds to quartz, and the matrix is also made of SiO_2 but with a density of 1.8 g cm^{-3} in order to represent a siliceous sediment. The moisture is zero.

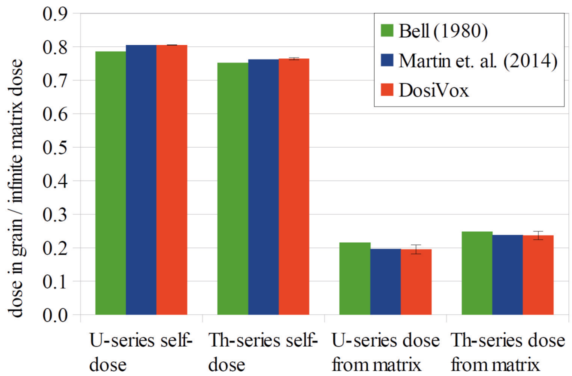

Figure 7. α-dose attenuation in 100 μm diameter quartz grain.

The *DosiVox* results are compared to the data calculated by Bell (1980) and Martin et al. (2014) for α-dose attenuation. The data from Martin et al. were obtained with a specific Geant4 code and are corrected for the matrix effect i.e. in taking into account the siliceous composition of the matrix. One can see on Fig. 7 that the *DosiVox* results match the data from Martin et al. and are close to Bell's calculations, what suggests a good reliability of the software for simulating α-particles.

The β-dose rate attenuation factors for self-dose in 100 μm and 1 mm grains, as the dose from the matrix in the case of a 1 mm grain, are given in Fig. 8. The β-spectra available in *DosiVox* for ^{40}K, U-series and Th-series have been used. The grains are composed of quartz, and both a silica matrix (SiO_2 100 %) and a clay matrix (SiO_2 54 %, Al_2O_3 46 %), both with density 1.8 g cm^{-3}, have been considered. The results are compared to the data from Guérin et al. (2012) concerning the β-dose rate attenuation for various grain sizes, deduced from the self-dose in quartz grains. A good agreement is found between the Guérin and *DosiVox* results. Small differences can be observed but remain lower than 3 %. They could possibly be explained by different assumptions made in the simulation. For the *DosiVox* simulations performed with a 1 mm grain, one can observe a perfect complementarity of the self-dose and the dose in the case of the silica matrix in agreement with the principle of superposition. It is also noticeable that a non-negligible difference can be observed between the dose rate from the silica and the clay matrix. Similar observations were made by Martin et al. (2014) for the α-dose rate in grains resulting in an attenuation factor depending on the matrix chemical composition. This effect on the β-dose rate could result in significant systematic errors in age calculation if not taken into account. In particular, it could be important for fine grains whose β-self-dose contribution is smaller than coarse grains, or for matrices whose chemical composition is significantly different from silica (since pure silica was the material usually used for calculating β-dose attenuation factors).

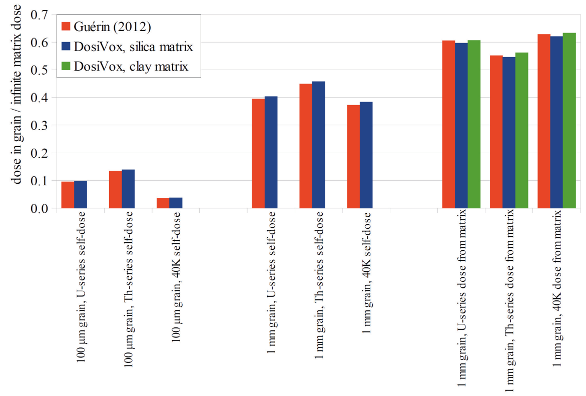

Figure 8. β-dose attenuation in 100 μm and 1 mm diameter quartz grains.

It is also well known that the sediment moisture content has a considerable impact on the attenuation of the dose rates because of the higher probability of interaction of the ionizing particles with water in comparison to the solid materials present in sediments (Aitken, 1985). Taking in account the effect of moisture on dose rates has a significant impact in dating. In order to assess this effect with *DosiVox*, different contents of water have been added to the previously used silica and clay matrices. The attenuated dose rates obtained are showed in Fig. 9.

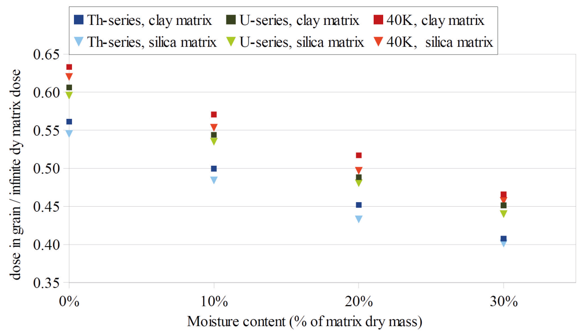

Figure 9. Impact of the matrix moisture content on the β-dose in 1 mm quartz grain.

Considering the equation of Zimmerman (1971) for taking into account the effect of water on the β-dose rate in a sediment, it is possible to use the results of these simulations to calculate the χ-factor which represents the ratio of β-dose absorption between the water and the sediment. If an equal contribution of the ^{40}K, Th- and U-series β-emissions is considered, values of $\chi = 1.20 \pm 0.02$ are calculated for the β-dose rate in both the silica and clay matrices. It is noticeable that, since these materials have different β-dose absorptions, they should lead to different χ-values, as it was already noticed by Martin et al. (2014) about the effect of moisture on the α-dose rate. But as one can observe on Fig. 9, this difference remains small for β-radiations. Moreover, the χ-value obtained with the *DosiVox* simulations is consistent with the value of 1.19–1.20 calculated by Nathan & Mauz (2008) for carbonate-rich sediments (Notice that these authors used another Monte-Carlo code -MCNP- for their simulations). Finally, if the emission of the ^{40}K is considered as the main contribution of the β-dose rate in the clay matrix, the χ-value calculated by the *DosiVox* simulations is closer to 1.19.

4.2. Complementarity of external and internal β-dose rates

The modeling of a single grain embedded in an infinite homogeneous matrix is not representative of sediments presenting a relative high proportion of grains. Dosimetric effects can be induced by the presence of grains next to each other. A common way to model these effects is to create a random packing of spheres, representing the grains, in order to simulate the dose rate in this geometry (Guérin et al., 2012). *DosiVox* offers this possibility by including a grain-packing algorithm, each grain created being an independent detector recording the dose it receives during the simulation. It is difficult to have a point of comparison for this kind of results because of the lack of similar calculations. The modeling of Nathan et al. (2003), Brennan (2006) or Guérin et al. (2012) focused on polymineral grain packings, with different radioactive contents, a situation not possible to reproduce in *DosiVox*: only one grain composition can be defined in a packing, and the particle emission can originate either from the matrix or from the grains. We then propose to test a more basic assumption in order to contribute to the validation of this kind of modeling: the principle of superposition of the dose rate. According to this principle, if two different parts of the dose rate are calculated separately, the total dose rate should be the sum of the two calculated ones.

The modeling that we consider here is composed of a grid of $3 \times 3 \times 3$ cubic voxels of 5 mm in size each one (for a total grid size of $15 \times 15 \times 15$ mm), filled with silica (SiO_2, density: 2.65 g cm^{-3}). In the central voxel, 400 μm diameter silica grains, representing 30 % of the voxel volume (about one thousand grains), are separated from the surrounding matrix (Fig. 10). All the volume is homogeneous in terms of material and radioactivity. The β-particles emitted from the grains or from the surrounding matrix and the adjacent voxels are simulated separately. One considers here the β-spectrum of the Th-series only. The doses deposited in the grains, originating from the grains or from the surrounding environment respectively, were recorded and compared to the infinite matrix dose rate (corresponding respectively to the grain *EmMass* and to the matrix *EmMass*). The average dose deposited in the grains and originating from the grains corresponds to 37 ± 1 % of the infinite matrix dose rate. The average dose deposited in the grains, but originating from the surrounding environment, corresponds to 63 ± 1% of the infinite matrix dose rate. The sum of the two dose rates is then compatible with 100, which fully satisfies the principle of superposition.

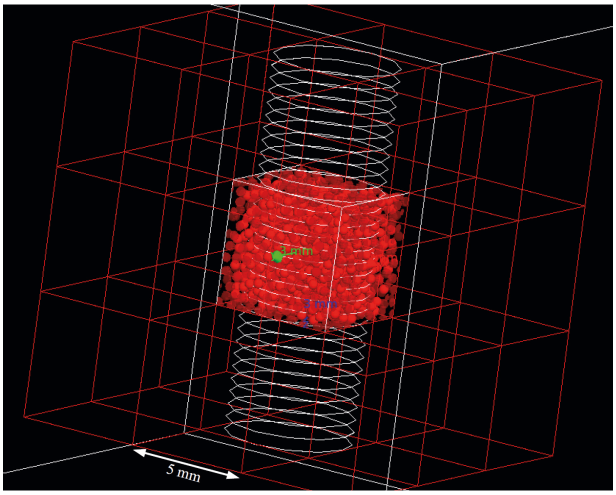

Figure 10. Visualization of the random packing of 400 μm grains for the β-dose rate complementarity test.

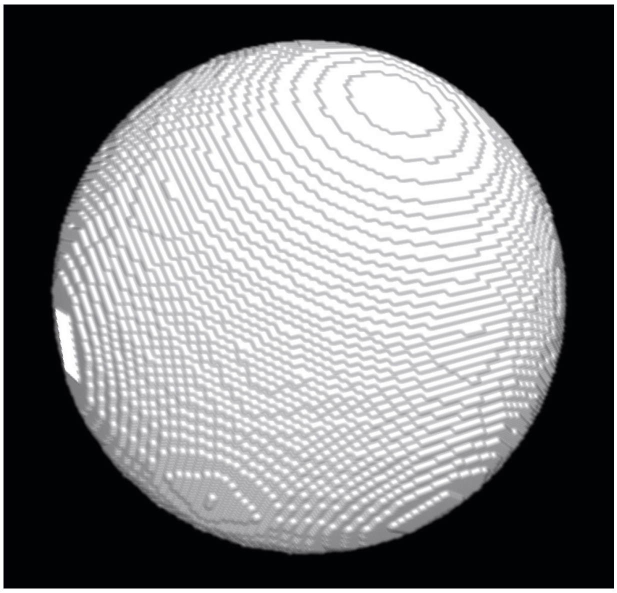

Figure 11. Voxelised modeling of a sphere.

5. Dose rate attenuation in a voxelised sphere

This last simulation layout purpose is to test the reliability of a voxelised modeling to represent an object for dose rate calculation. More precisely, the sub-voxelised detector of *DosiVox* was used to represent a 100 voxels diameter sphere. This modeling was constructed by loading a 3D image of a sphere in the *DosiVox* interface for the creation of a "pilot" text file (Martin et al., 2015a) (Fig. 11). As the size of the voxels can be changed, the total size of the sphere can be adjusted for different modelings. The results of the simulations of α-, β- and γ-dose rates in spheres of various dimensions, and various materials in the case of the γ-emissions, are presented in Table 1 and compared to standard attenuation factors for these configurations.

The results of the dose rates simulated with *DosiVox* using the voxelised modeling of spheres are in good agreement with the reference data. However, a non-negligible bias can be observed for the γ-self-dose compared to the data from Aitken (1985), derived from Mejdahl (1983) and presented as approximations to evaluate the γ-dose rate in a sphere. These differences may result from the incomplete γ-spectrum used by Mejdahl or by the fact that Aitken approximated the data rather than using an exact equation. Moreover, the *DosiVox* simulations of the self-doses in a non-voxelised 10 cm sphere (i.e. in the same layout as for section 3 calculations) gave results identical to the simulations of the voxelised spheres within the range of 1 %. We can then conclude that voxelised modeling with reasonable resolution can be considered as representative of non-voxelised modeling.

In addition to the average self-dose rate in a sphere, the sub-voxelised detector of *DosiVox* creates a three-dimensional mapping of the dose deposited in the form of successive text files containing a matrix of dose values, each file representing the dose deposited in a slice of the model. It is possible to read this series of text files with an image processing software, like *ImageJ* (Rasband, 1997; Schneider et al., 2012), to visualize and study the dose in each slice, or to reconstruct the 3D-mapping of the dose deposited (Fig. 12). Using this process or the records of the "Probe" detector of *DosiVox*, one can obtain the dose profile through simulation (Fig. 13). The various dosimetric data collected by voxelised modeling in *DosiVox* could bring useful information for better understanding the dosimetric phenomena encountered in paleodosimetric dating.

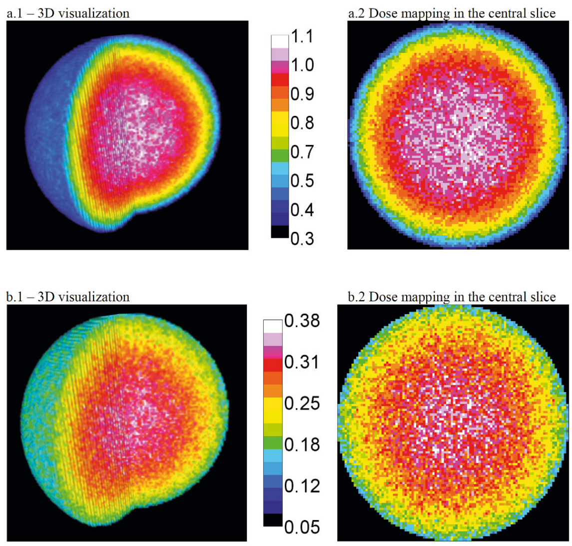

Figure 12. Self-dose mapping in voxelised spheres.

Radiation (Series)	Diameter of the sphere	Density (g cm^{-3})	Material	*DosiVox* (Selfdose/*EmMass*)	Reference value	Reference publication	Difference
α (Th)	100 μm	2.65	Silica	0.765	0.764	Martin et al. (2014)	0.02 %
β (Th)	100 μm	2.65	Silica	0.136	0.134	Guérin et al. (2012)	-1.57 %
β (Th)	1 mm	2.65	Silica	0.455	0.449	Guérin et al. (2012)	-1.30 %
γ (Th)	10 cm	2.65	Silica	0.242	0.265	Aitken (1985)	9.46 %
γ (Th)	10 cm	2	Clay	0.186	0.200	Aitken (1985)	7.43 %

Table 1. : α-, β- and γ-self-doses in the voxelised modeling of a sphere.

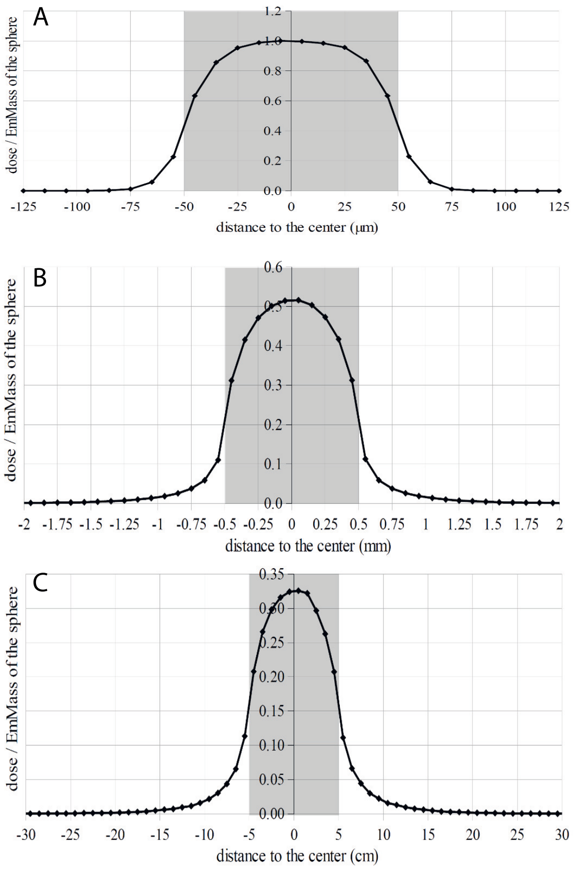

Figure 13. Dose rate profiles along the middle axis of voxelised radioactive spheres.

6. Conclusion

The results of the *DosiVox* simulations for the cases presented here are consistent with the already published data. Some differences can be observed but may be due to nuclear and cross sections data updates, or to small differences between the modelings in *DosiVox* and the previous representations. More important is the fact that the principle of superposition has been successfully tested in different modeling cases. Moreover, *DosiVox* offers tools allowing accessing spatially detailed information about the dose rates, in clusters of grains, or through three-dimensional dose rate mapping.

In addition to the comparison with usual data, the *DosiVox* results highlight the limits of some assumption frequently used: the γ-dose rate close to the surface of a sediment does not perfectly match the half of the infinite matrix dose rate in real environment conditions. We also observed that a non-negligible difference is observed between the attenuation of the matrix β-dose in grain and the usual way to calculate it by taking the complement of the self-dose factor of the grain. This observation had already been made by Martin et al. (2014) about the effects of the matrix composition on the α-dose rate in grains. These observations demonstrate that, since it is impossible to gather dosimetric data about all the possible cases to be encountered in paleodosimetric dating, Monte-Carlo simulations are of great help for dose rate investigations. *DosiVox*, by its accessibility, could bring easy solutions for dose rate calculations in the cases exceeding the infinite matrix hypothesis.

Comparisons with the tabulated data, often obtained by numerical calculations and Monte-Carlo simulations, is only a first step for testing the reliability of *DosiVox*. The various possibilities of modeling available exceed the dosimetric layout documented in the literature. A most pertinent validation would be to compare the results of *DosiVox* obtained in complex dosimetric cases with experimental measurements. However, this way is difficult to implement because of the need to use detectors for dose measurements, which could represent a bias compared to a modeling and add a necessary step of calibration with a potential uncertainty when calculating doses. A special care has to be taken to achieve both experimental measurements and corresponding modeling but these comparisons need undoubtly to be done.

Acknowledgments

The authors are grateful to the Aquitaine Region Council for funding this research through the program: DOSI-ART - DOSe reconstruction In archaeological ARTefacts and sediments. This work was also supported by the French National Research Agency via the LaScArBx Labex (project number ANR-10-LABX-52).

References

Aitken, M J. *Thermoluminescence dating*. Studies in archaeological science. Academic Press, 1985. ISBN 9780120463817.

Bell, W T. *Alpha dose attenuation in quartz grain for thermoluminescence dating*. Ancient TL, 12(1): 1–5, 1980.

Brennan, B J. *Variation of the alpha dose rate to grains in heterogeneous sediments*. Radiation Measurements, 41: 1026–1031, 2006.

Brennan, B J, Rink, W J, McGuirl, E L, Schwarcz, H P, and Prestwich, W V. *Beta doses in tooth enamel by "one-group" theory and the ROSY ESR dating software*. Radiation Measurements, 27 (2): 307–314, 1997. doi: 10.1016/S1350-4487(96)00132-1.

Cross, W G, Freedman, N O, and Wong, P Y. *Tables of beta-ray dose distributions in water*. Technical Report AECL-10521, Chalk River Laboratoris, Chalk River, Onario, 1992.

Fain, J, Soumana, S, Montret, M, Miallier, D, Pilleyre, T, and Sanzelle, S. *Luminescence and ESR dating Beta-dose attenuation for various grain shapes calculated by a Monte-Carlo method*. Quaternary Science Reviews, 18(2): 231–234, 1999. doi: 10.1016/S0277-3791(98)00056-0.

Fleming, S J. *Thermoluminescent dating: refinement of the quartz inclusion method*. Archaeometry, 12(2): 133–143, 1970.

Grün, R. *Beta attenuation in thin layers*. Ancient TL, 4: 1–8, 1986.

Grün, R. *Alpha dose attenuation in thin layers*. Ancient TL, 5: 6–8, 1987.

Guérin, G, Mercier, N, Nathan, R, Adamiec, G, and Lefrais, Y. *On the use of the infinite matrix assumption and associated concepts: A critical review*. Radiation Measurements, 47(9): 778–785, 2012. doi: 10.1016/j.radmeas.2012.04.004.

Martin, L, Mercier, N, and Incerti, S. *Geant4 simulations for sedimentary grains in infinite matrix conditions: The case of alpha dosimetry*. Radiation Measurements, 70: 39–47, 2014. doi: 10.1016/j.radmeas.2014.09.003.

Martin, L, Incerti, S, and Mercier, N. *DosiVox: Implementing Geant 4-based software for dosimetry simulations relevant to luminescence and ESR dating techniques*. Ancient TL, 33(1): 1–10, 2015a.

Martin, L, Mercier, N, Incerti, S, Lefrais, Y, Pecheyran, C, Guérin, G, Jarry, M, Bruxelles, L, Bon, F, and Pallier, C. *Dosimetric study of sediments at the beta dose rate scale: Characterization and modelization with the DosiVox software*. Radiation Measurements, 81: 134–141, 2015b. doi: 10.1016/j.radmeas.2015.02.008.

Mejdahl, V. *Thermoluminescence dating: beta-dose attenuation in quartz grains*. Archaeometry, 21: 61–72, 1979.

Mejdahl, V. *Feldspar inclusion dating of ceramics and burnt stones*. PACT, 9: 351–364, 1983.

Nathan, R P and Mauz, B. *On the dose-rate estimate of carbonate-rich sediments for trapped charge dating*. Radiation Measurements, 43(1): 14–25, 2008. doi: 10.1016/j.radmeas.2007.12.012.

Nathan, R P, Thomas, P J, Jain, M, Murray, A S, and Rhodes, E J. *Environmental dose rate heterogeneity of beta radiation and its implications for luminescence dating: Monte Carlo modelling and experimental validation*. Radiation Measurements, 37(4-5): 305–313, 2003. doi: 10.1016/S1350-4487(03)00008-8.

Rasband, W S. *ImageJ, U.S. National Institutes of Health, Bethesda, Maryland, USA*. Technical report, 1997. URL http://imagej.nih.gov/ij/.

Schneider, C A, Rasband, W S, and Eliceiri, K W. *NIH Image to ImageJ: 25 years of image analysis*. Nature Methods, 9(7): 671–675, 2012. doi: 10.1038/nmeth.2089.

Zimmerman, D W. *Thermoluminescent dating using fine grains from pottery*. Archaeometry, 13(1): 29–52, 1971. doi: 10.1111/j.1475-4754.1971.tb00028.x.

Reviewer

Nigel Spooner

Ancient TL

Evaluation of soil-moisture content for OSL dating using an infiltration model

Ravid Rosenzweig[1*] and Naomi Porat[1]

[1]Geological Survey of Israel, 30 Malkhei Israel St., Jerusalem 95501, Israel

[*]Corresponding Author: rravid@gsi.gov

Received: September 12, 2015; in final form: December 3, 2015

Abstract

Uncertainty in soil-moisture content estimation can introduce large errors into calculation of OSL ages. In the current paper we evaluate the soil-moisture content by using an infiltration model which encompasses site-specific information regarding the climatic conditions and soil properties. The model provides the variation of the soil-moisture content with depth and time. It also provides clear uncertainty bounds for the estimated soil-moisture profile which serves as a measure for model reliability. The current approach is implemented to calculate the soil-moisture profile of a Late-Holocene, open-structure soil section subjected to Mediterranean climate in which hot and dry summers and cool and wet winters generate large variation in the moisture-content. We show that the model can improve soil-moisture estimation, reducing the associated uncertainty and accounting for the depth from the soil surface. These estimates can then be used to better constrain uncertainties in OSL dose rate calculations.

Keywords: moisture content

1. Introduction

The importance of estimating time-averaged moisture contents for accurate OSL dating cannot be underestimated. Large uncertainties in moisture contents introduce large errors into the ages. For example, assumption of a moisture fraction of 20% instead of 10% g/g of sample, will decrease dose rate to 'coarse grains' and increase the calculated age by $\sim$10% (Aitken, 1985, p. 76).

Mediterranean climate typically has large differences between summer and winter, with hot and dry summers and cool and moist winters, resulting in great variability in soil moisture. A single sample cannot capture the average annual moisture contents due to these large variations in precipitation and evaporation, particularly as the beginning and end of the rainy season vary greatly from year to year.

While our ability to reconstruct soil moisture contents for past climates is limited, we can in the least get a good handle on current seasonal variations. Lowick & Preusser (2009) have reconstructed the soil-moisture of saturated samples that have desiccated, but no attempt was made to assess the mean moisture content in the unsaturated zone. Recently, Nelson & Rittenour (2015) used grain-size distribution and maps of the annual mean water state (mean matric head) to calculate the mean moisture content of Holocene sediments from Kebab Creek, Utah for OSL dating.

While the work of Nelson & Rittenour (2015) provides a simple way to calculate soil moisture content based on large-scale soil properties maps, we take a different approach and obtain soil moisture content by using an infiltration model which incorporates site-specific climatic data combined with grain size and density measurements. The addition of bulk density measurements to the grain size data improves by a great deal the assessment of the water content (Schaap et al., 2001). We also give uncertainty bounds to the calculation, providing a confidence interval for the soil-moisture. The model provides the full variability of soil moisture in time and space, thus allowing to specifically consider the effect of depth on the moisture content. We demonstrate the use of the procedure by applying it to predict the moisture content of anthropogenic soil within archaeological farming terraces of Late Holocene age, with open-structure soil prone to evaporation (Gadot et al., 2015). The results are then used in the age calculations to assess the impact of the moisture content on the ages.

	Jan	Feb	Mar	Apr	May	June	July	Aug	Sep	Oct	Nov	Dec
Rainfall (mm)	133.2	118.3	92.7	24.5	3.2					15.4	60.8	105.7
Rainy days	9.7	8.7	7.6	2.7	0.7					1.9	5.5	7.9
Daily evaporation (mm)	2.5	2.8	4.2	5.7	6.5	6.9	7.1	6.5	5.6	5	4	2.8

Table 1. Climatic conditions near Har-Eitan (evaporation and rain data averaged for 1988-2000 and 1970-2000, respectively)

2. Research site

The area is the limestone highlands of central Israel located within the Mediterranean climate zone. The study was conducted at Har (Mount) Eitan, a hilly spur almost 800 m high about 10 km west of Jerusalem. In this area, the limestone slopes are covered with archaeological bench terraces, created from stone walls back-filled with soil. Pits were excavated for OSL dating within the framework of a larger study on the terracing of the Judea Mountains (Gadot et al., 2015). For accurate dating of terrace construction, we needed to know the average annual moisture content for samples located at depths from 0.25 to 2.0 m.

The climatic data used in the model were taken from the database of the Israeli Meteorological Service (`http://www.ims.gov.il`). Precipitation data were taken from a meteorological station in Jerusalem located 10.5 km east of Har-Eitan while evaporation data was taken from Rosh-Zurim meteorological station located 11 km south east to Har-Eitan; both stations are the closest to the study area. The monthly-averaged climatic conditions for Har-Eitan are given in Table 1. The rainy period lasts from November to April with an average of 45 rainy days and an average annual rainfall of 554 mm. Mean daily class A pan evaporation (potential evaporation; Jarraud, 2008) varies from 7.1 mm in July to 2.5 mm in January.

Figure 1. A typical soil profile of one of the pits in Har-Eitan. The holes in the profile represent the locations where undisturbed soil or other samples were taken. Insert: The sampling ring and ring holder used to take the undisturbed samples.

3. Methods

Twenty four samples taken at different depths along the open excavated pits (Fig. 1) were analyzed for particle size distribution (PSD; smaller than 2 mm). The average soil PSD for the sand, silt and clay fractions and their respective standard deviation, and the PSD of two additional samples that were used to evaluate the sensitivity of the model to soil texture, are presented in Table 2.

	% Sand	% Silt	% Clay
Average	38.3 (11.4)	55 (11)	6.7 (1.9)
Highest silt	11.4	80.4	8.2
Lowest silt	58.4	35.7	5.9

Table 2. Particle size distribution ($<$ 2 mm) for soil samples from Har-Eitan terraces. Values in parentheses represent standard deviation.

Gravimetric water content (or mass fraction moisture) was measured in winter (about a week after a rain event) and in the summer by the gravimetric method (Dane & Topp, 2002) on samples taken at different depths in the pits. The average gravimetric water content in the summer was 5.5% $\pm$ 1.2% g/g (N=5) whereas the average gravimetric water content after rain was 24% $\pm$ 2% g/g (N=6; Table 3). Bulk density was measured on undisturbed soil samples of known volume. The average bulk density for this particular area was found to be 1.10 ± 0.12 g/cm^3 (N=5). Bulk density is important since it is directly related to cosmic radiation attenuation (Prescott & Hutton, 1994) and indirectly to both beta and gamma dose rates through soil moisture content.

Pit	Depth (cm)	Gravimetric water content (g/g)
A4	60	0.20
A4	33	0.26
A4	27	0.27
A1	75	0.24
A1	22	0.23
A1	50	0.23
Average	44.5 (20.7)	0.24 (0.02)

Table 3. Measurements of gravimetric water content at Har-Eitan. Samples were taken during the winter of 2014-15, approximately one week after a rain event. Values in parentheses represent standard deviations.

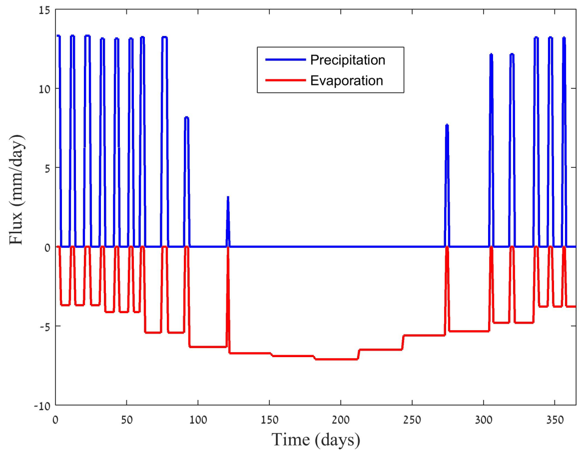

Figure 2. Precipitation and evaporation fluxes specified for the model over a year. Evaporation is defined as a negative flux.

4. Model Setup

In this work we use a one dimensional (1D) infiltration model to evaluate the mean annual water content in the soil. The model allows calculation of variation in water content with depth by solving the soil-water dynamics while incorporating data of the soil PSD and climatic conditions. The model provides the water content profile with much higher certainty than the one obtained from one or two measurement at random points in time, as it provides the full temporal and spatial variations.

We use Hydrus 1D (`http://www.pc-progress.com/en/Default.aspx?hydrus-1d`), a free code developed by the US salinity lab to model water flow and water content within the soil (Šimůnek et al., 2008). Hydrus 1D describes variably-saturated water flow by solving the Richard's equation

$$\frac{\partial \theta}{\partial t} = \frac{\partial}{\partial z} \cdot \left(K(h) \frac{\partial h}{\partial z} \right) + \frac{\partial K}{\partial z} \tag{1}$$

where θ is the volumetric water content, h the matric head, t the time, z the vertical coordinate and $K(h)$ the unsaturated hydraulic conductivity which is a function of the matric head. We note that the volumetric water content (volume of water per total volume of soil in units of cm^3/cm^3) commonly used in infiltration models is a different measure of soil moisture than the gravimetric water content (water weight per dry soil weight in units of g/g) used in dose rate calculations for luminescence dating. The conversion from gravimetric to volumetric water content is given by $\theta = \omega \cdot \rho_b / \rho_w$ where ω is the gravimetric water content, ρ_b is the bulk soil density and ρ_w is the density of water, commonly taken as 1 g/cm^3 .

To solve Equation 1, relations for the hydraulic conductivity function and for the soil water-retention curve $(\theta(h))$ are needed. We use the van Genuchten and van Genuchten-Mualem models (Mualem, 1976; van Genuchten, 1980) for the soil water retention curve

$$Se = [1 + (\alpha \mid h_m \mid)^n]^{-m} \tag{2}$$

and hydraulic conductivity, respectively,

$$K = K_S \sqrt{Se} \left[1 - \left(1 - Se^{1/m} \right)^m \right]^2 \tag{3}$$

where α, n and $m = 1 - 1/n$ are empiric parameters which depend on the soil pore size distribution, K_S is the saturated hydraulic conductivity and $Se = (\theta - \theta_r)/(\theta_s - \theta_r)$ is the effective saturation where θ_s is the porosity and θ_r is the irreducible water content. The porosity and irreducible water content represent the upper and lower bounds of the water content in soil, respectively.

The modeled domain represents a profile of 10 m depth of homogeneous soil. Although Har-Eitan consists of bedrock at 2 m depth at most, it was decided to ignore it since it is highly fractured and the fractures are filled with the natural soil. Thus, the bedrock is not expected to impede water flow downwards. Boundary conditions for the model were assigned as atmospheric boundary condition at the soil surface and free-drainage condition (i.e., $\frac{\partial \theta}{\partial z} = 0$) at the lower boundary. The atmospheric boundary condition represents either an evaporation flux out of the soil surface or a precipitation flux into the soil surface. Daily fluxes were calculated from the daily average of potential evaporation, the monthly average of precipitation and the average number of rainy days for each month (Table 1). It was assumed that each rain event lasts for 3 days and that on rainy days the potential evaporation is zero. The daily evaporation and precipitation fluxes put into the model are shown in Figure 2.

The value of the soil hydraulic parameters (α, n, m and K_S) presents the greatest uncertainty in unsaturated flow models. In the current work, the hydraulic parameters of the soil were determined as follows (Table 4): the porosity θ_s and irreducible water content θ_r were assigned as constants. The porosity was calculated using the relation $\theta_s = 1 - \rho_b/\rho_s$ where ρ_s is the grain density. Porosity was calculated based on the measured bulk density and by assuming a grain density of 2.65 g/cm^3 .

The irreducible water content was assigned as the minimal value in the range of water content measured in summer at the surface of the open holes (5%). Summer water content was also used as the minimum water content by Burbidge et al. (2014). The other parameters α, n, and K_S were predicted by ROSETTA (`http://www.ars.usda.gov/News/docs.htm?docid=8953`), a free computer program developed by the US salinity lab that predicts the soil hydraulic properties using a neural network analysis based on the soil grain size distribution and bulk density (Schaap et al., 2001). The program uses a large dataset which contains properties of more than 2000 soils. It provides average values and uncertainty bounds for each parameter.

The soil profile was discretized into 201 nodes where the grid was refined near the soil surface and spacing was gradually increased towards the deeper sections of the profile. The model was left to run for 300 years to achieve a temporally

Soil structure	θ_r cm^3/cm^3	θ_s cm^3/cm^3	$\alpha(1/m)$			n			K_S m/day		
			Average	High	Low	Average	High	Low	Average	High	Low
Average	0.055	0.58	0.51	0.637	0.4063	1.6608	1.736	1.588	1.422	2.095	0.9654
Highest-silt			0.43	0.631	0.293	1.745	1.878	1.621	1.2167	2.386	0.621
Lowest-silt			1.58	1.88	1.33	1.452	1.518	1.393	1.7084	2.44	1.1962

Table 4. Soil hydraulic properties used in the model for the three soil structures. Average, high and low values of α, n and K_S represent the average, the high and the low bounds predicted by ROSETTA.

periodic condition where no change in the results was observed from one year to the next.

To evaluate the sensitivity of the mean annual water content to the hydraulic parameters and soil composition, hydraulic parameters were predicted for 3 PSD's (Table 2). The first was obtained by averaging all 24 soil samples taken from the terraces, the other two represent individual samples having the highest and lowest silt fraction and the lowest and highest sand fraction, respectively (Highest silt and Lowest silt in Table 2). Hydraulic parameters were predicted for each soil structure (Table 4) and models were run for sets of hydraulic parameters which represent combinations of the average/ lowest/ highest or intermediate values predicted for the different parameters. The water content measured on samples taken during winter was considered as the maximal water content (Burbidge et al., 2014) and was used to calibrate the models such that only runs that yielded a winter (after rainfall) water content of 26% $\pm$ 2% cm^3/cm^3 at a depth of 50 cm were included in the analysis. This range corresponds to the average volumetric water content $\pm$ one standard deviation measured at an average depth of ~50 cm (Table 3). We note that since measurements of winter water content were taken once in 2015 while the model is based on multi-year average climatic data, some flexibility in the maximal water content is allowed by specifying this range.

5. Results and Discussion

The profile of the average annual water content is displayed in Figure 3. The water content profile was obtained for the three investigated soil compositions and for combination of different sets of soil-hydraulic properties that lie within the uncertainty bounds for each soil type. It is shown that near the soil surface the water content and its variability ($\pm$ 1.5%) are lower than in the deeper sections of the profile since the water content is influenced by water evaporation from the soil. At larger depths, there is a greater variability in water content (approx. $\pm$ 2%, at 2 m) that depends on soil composition and soil-hydraulic properties. It is shown that for each curve, the annual average water content for a given soil composition, under present conditions, is approximately constant at depths greater than 0.6 m. This is because deeper in the section evaporation no longer affects soil moisture. This "constant moisture" depth is expected to change with the soil type and the value of potential evaporation.

For the average soil composition, the water content measured after rain limited the saturated hydraulic conductivity

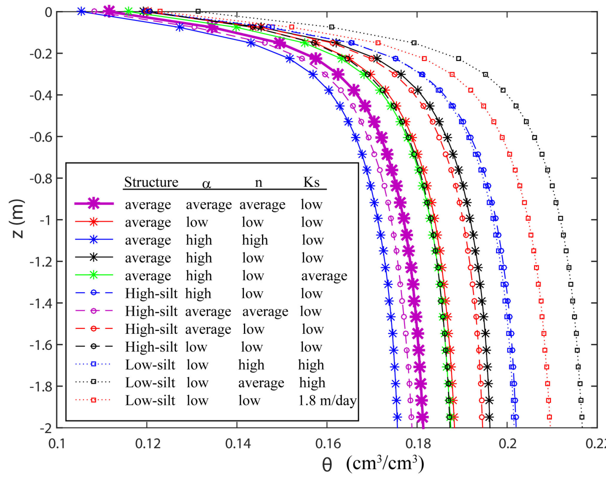

Figure 3. Average annual water content profile obtained for the three soil compositions and for different sets of soil hydraulic properties. Asterisks and solid lines - average soil; circles and dashed lines - highest-silt soil; squares and dotted lines - lowest silt water soil. The purple, solid, thick curve represents the water content profile which was obtained for the predicted average α and n values for the average soil composition.

to the low-to-average values of the predicted range. The water content obtained for the average α and n values and low K_S (the thick purple curve on Fig. 3) is 0.170 cm^3/cm^3 and 0.177 cm^3/cm^3at depth of 0.5 and 1 m, respectively. Considering all the curves obtained for the average soil composition, the annual average water content can be estimated as 0.174 $\pm$ 0.01 cm^3/cm^3 and 0.182 $\pm$ 0.01 cm^3/cm^3 at depth of 0.5 and 1 m, respectively. This corresponds to gravimetric water content (as used in dose rate calculations for luminescence dating) of 0.158 $\pm$ 0.009 g/g and 0.165 $\pm$ 0.009 g/g at depth of 0.5 and 1 m, respectively.

Naturally, when taking into account the Highest-silt and Lowest-silt soil compositions, the uncertainty in predicting the water content increases. Figure 3 shows that the Lowest-silt soil yields higher water content. This is the result of the larger α values predicted for this soil structure. Generally speaking, larger values result in a lower infiltration rate which leaves the soil wetter. Still, the range of the water content remains rather small with the volumetric water content estimated as 0.180 $\pm$ 0.016 cm^3/cm^3 and 0.192 $\pm$ 0.02 cm^3/cm^3 at depth of 0.5 and 1 m, respectively. The corresponding gravimetric water contents are 0.163 $\pm$ 0.0145 g/g and 0.174 $\pm$ 0.018 g/g. These estimated values have much lower uncertainty bounds than the uncertainties commonly used in OSL dating.

Using this range of values to calculate dose rates and ages for a typical sample from Har-Eitan at a depth of 0.5 m, we obtain an age range of 1780-1800 or 1770-1800 years for the better or less constrained soil composition, respectively, well within any error range of an OSL age.

Naturally, this model has several limitations. First, as most conventional models of flow in unsaturated conditions, it does not directly consider effects such as water repellency and swelling. To account for these, one would have to measure the soil water retention curve to directly calibrate the soil hydraulic properties. In most studies, however, these effects are traditionally ignored.

Second, the model is based on modern climatic conditions. Long-term changes in rainfall, temperature and vegetation (affecting evapotranspiration) will obviously affect soil moisture content. However, given the limited data on past conditions and its low resolution, our starting point is modern climatic conditions. Using paleoclimate data, one could extrapolate the results to past conditions; however this is beyond the scope of the current paper.

6. Conclusions

Average annual soil moisture profiles were calculated using an infiltration model encompassing climatic data and soil properties. This estimation has several advantages over the conventional way water content is estimated for OSL dating and over recent contributions in the field. First, it is physically based and encompasses data of the site-specific climatic conditions and soil structure. Second, it accounts for variation of the water content with the soil depth; and last, it provides clear uncertainty bounds and reduces the variability in the water content estimation and thus in the luminescence age. Furthermore, bulk density (or at least porosity) measurements can also improve estimates of the cosmic dose rate contribution to the dose rate.

To predict moisture contents, monthly average data of rainfall and evaporation are needed together with soil grain size distribution, bulk density and water content measurement in winter and summer. If no bulk density and summer water content measurements are available, one can predict the soil hydraulic properties based on the grain size distribution alone (using ROSETTA). This is, however, not recommended as the associated uncertainty of this prediction is much larger.

The model shows two regions within the soil profile; the upper part in which moisture content is more dependent on evaporation and less on soil type, and the lower part in which moisture content is mostly a function of soil properties and is relatively constant with depth. In our study area, the transition between these two regions occurs roughly at 0.6 m. This depth, however, is expected to be site-specific and related to the soil type and evaporation rate.

Acknowledgments

The research was supported by an Israel Science Foundation grant (Grant 0606714492) awarded to Naomi Porat and Yuval Gadot.

References

Aitken, M.J. *Thermoluminescence dating*. Studies in archaeological science. Academic Press, 1985.

Burbidge, C., Trindade, M., Dias, M., Oosterbeek, L., Scarre, C., Rosina, P., Cruz, A., Cura, S., Cura, P., and Caron, L. *Luminescence dating and associated analyses in transition landscapes of the alto ribatejo, Central Portugal*. Quaternary Geochronology, 20: 65–77, 2014.

Dane, J.H. and Topp, C.G. *Methods of soil analysis, part 4- physical methods. p. 1692*. Soil Science Society of America, Madison, 2002.

Gadot, Y., Davidovich, U., Avni, G., Avni, Y., and Porat, N. *The formation of terraced landscapes in the Judean Highlands, Israel*. Antiquity, 346, 2015. URL http://antiquity.ac.uk/projgall/gadot346. Project Gallery article.

Jarraud, M. *Guide to meteorological instruments and methods of observation (wmo-no. 8)*. World Meteorological Organisation: Geneva, Switzerland, 2008.

Lowick, S. and Preusser, F. *A method for retrospectively calculating the water content for silt-dominated desiccated core samples*. Ancient TL, 27: 1–5, 2009.

Mualem, Y. *New model for predicting hydraulic conductivity of unsaturated porous-media.* Water Resources Research, 12: 513–522, 1976.

Nelson, M.S. and Rittenour, T.M. *Using grain-size characteristics to model soil water content: Application to dose-rate calculation for luminescence dating.* Radiation Measurements, 81: 142–149, 2015.

Prescott, J.R. and Hutton, J.T. *Cosmic ray contributions to dose rates for luminescence and esr dating: Large depths and long-term time variations*. Radiation Measurements, 23: 497–500, 1994.

Schaap, M.G., Leij, F.J., and van Genuchten, M.Th. *Rosetta: A computer program for estimating soil hydraulic parameters with hierarchical pedotransfer functions*. Journal of Hydrology, 251: 163–176, 2001.

Šimůnek, J., van Genuchten, M.T., and Šejna, M. *Development and applications of the hydrus and stanmod software packages and related codes*. Vadose Zone Journal, 7: 587–600, 2008.

van Genuchten, M.T. *A closed-form equation for predicting the hydraulic conductivity of unsaturated soils*. Soil Science Society of America Journal, 44: 892–898, 1980.

Reviewer

Chris Burbidge

Ancient TL

Induced thermoluminescence dating of basalts

Derek W.G. Sears[1]*

[1] Space Science and Astrobiology Division and Bay Area Environment Research Institute, NASA Ames Research Center, Mountain View, California 94035

*Corresponding Author: derek.sears@nasa.gov

Received: December 7, 2015; in final form: December 11, 2015

Abstract

Several attempts to date basalts using natural thermoluminescence methods have failed because the phosphor, feldspar, displays anomalous fading. In the late nineteen-seventies R.D. May reported an increase in induced TL with age for Hawaiian basalts. Studies of meteorites have shown that induced TL can increase with time (or heating) due either to production of the phosphor by crystallization of glass or the diffusion of impurity quenchers out of the phosphor. The increase can be many orders of magnitude. I therefore propose that induced TL is a potential new method of thermoluminescence dating of basalts. I also suggest that it may be possible to make the method absolute, i.e. not dependent on empirical calibration, by performing the appropriate laboratory kinetic studies.

Keywords: Keywords: Basalts, induced thermoluminescence, dating

1. Introduction

Not long after the development of the fine-grain method of using natural thermoluminescence (TL) to date archeological artifacts, it was proposed that the method might be applicable to dating fairly young volcanic rocks (e.g. Aitken et al., 1968). However, almost immediately it was realized that volcanic feldspars, the TL phosphor in volcanic rocks, displayed anomalous fading and therefore the method was not practical (Wintle, 1973). Since then, while there have been some successes the approach has been to try to look at the TL produced at alternative (non-visible) wavelengths and other physical methods of avoiding the problem (e.g. Tsukamoto et al., 2011).

Here I propose an entirely different method for dating volcanic rocks, namely to use the time-dependency of the induced TL signal that is present in many rocks. This dependency is caused by the fact that volcanic rocks, for instance, are non-equilibrium systems in many respects. They cool rapidly; so much of the feldspathic component is glassy, or otherwise amorphous, with little or no induced TL. Similarly, they are out of equilibrium compositionally, they may contain impurities that quench the TL. However, in approaching equilibrium, induced TL levels will increase in a time-dependent way and if the kinetics can be quantified then a new and independent method of dating will be possible.

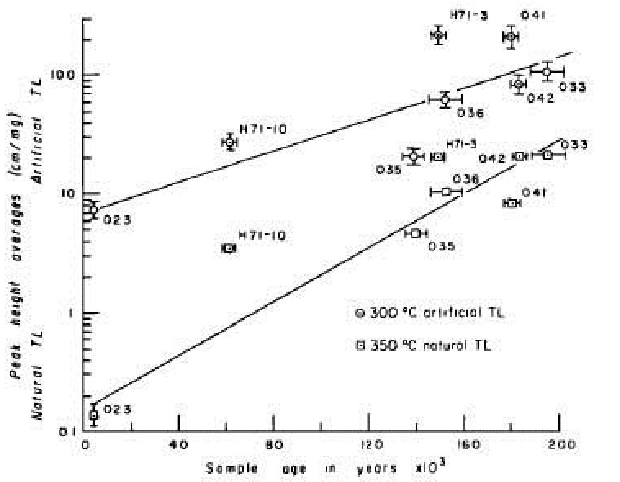

Figure 1. Figure from May (1977, 1979) comparing induced TL (which he called "artificial TL", upper line), and natural TL (lower line), with sample age for Hawaiian basalts.

2. R.D. Mays study of 1977

May (1977, 1979) attempted to date lavas from the Hawaiian islands using the conventional methods of TL dating based on natural TL. He used the fine-grained matrix method that is so successful in dating archeological artifacts, calculating the dose from the composition of the samples and assuming a nominal cosmic ray dose. He claimed success, despite the problem of anomalous fading.

However, somewhat surprisingly he found that the induced TL, which he called the "artificial TL", also increased with time (Fig. 1). He suggested that the samples were undergoing radiation damage that was producing traps.

3. Correlation between induced TL and age

Shortly before May's study, a Swiss group (Houtermans & Liener, 1966), following up on work performed in Russia (Komovsky, 1961), showed that the induced TL of meteorites increased with potassium-argon age and they also attributed this to the production of traps by radiation damage. May cited their work.

The present writer made similar measurements on a suite of ordinary chondrite meteorites, the largest class of meteorites, and also found a correlation between induced TL and potassium-argon age (Sears, 1980). However, in my case the explanation was very clear. The low induced TL meteorites were heavily shocked by an impact between asteroids in space, while the high induced TL meteorites were effectively unshocked. Impacts generate shock waves that compress the material and heat it, so while some minerals show the effect of compression others show the effect of heat. For example feldspar is melted by the heating, so is the metal and sulphides which form eutectics that spread through the meteorite, especially along cracks also formed by the shock event. The effect of these kinds of shock on meteorite and feldspar induced TL have been studied in some detail by Haq et al. (1988), and Hartmetz et al. (1986).

To further confirm that radiation damage is not causing the age-related induced TL changes, meteorites have been exposed to radiation doses comparable or greater than would have been experienced in the age of the solar system. Alpha, beta, and gamma radiation have been used, so have fluxes of protons, and no change in induced TL was produced (Sears, 1980).

It is clear that the correlation between induced TL and age reported by four groups in the 1960s to 1980s is not due to radiation damage, but physical and mineralogical changes in the meteorites that coincidentally include argon loss. Thus instead of thinking of the TL properties as being dependent on radiation and thermal history, as for natural TL, the induced TL is better considered as a petrographic or mineralogical tool, especially when used conjunction with cathodoluminescence. The CL observations can also be combined with microscopic and electron microprobe studies for a better understanding of the geological processes experienced by the samples.

4. Case study I: Induced TL increases due to the production of feldspar

When a suite of ordinary chondrites that had not experienced any significant shock was examined a spectacular range of induced TL levels was observed, the values covered a factor of about 10^5 (Sears et al., 1980). In this case, the values correlated very strongly with parent body metamorphism (Fig. 2).

Metamorphism, heating of rocks in the solid state, usually by virtue of burial, is an important feature of ordinary chondrites and has been recognized in meteorites since the early sixties (Van Schmus & Wood, 1967). Most meteorites have been highly metamorphosed and the internal properties resulting from their original formation have been largely wiped out. However, a few meteorites have escaped this process and contain within them material that was present in the solar nebula before the Sun and planets formed. They constitute a powerful witness of conditions and processes in the early solar system.

Cathodoluminescence and other studies quickly showed the reason for this correlation with metamorphism. The major TL phosphor, feldspar, was absent in the low TL meteorites and present in the high TL meteorites. When the meteorites formed, the feldspathic elements, calcium, aluminum, sodium and so on were in glass that was located in solidified droplets that are characteristic of these solar system materials. During metamorphism this glass crystalizes to form crystals of feldspar.

What is remarkable is not just that this trend exists, but the remarkable sensitivity of the relationship at the low end of the metamorphic sequence. Induced TL is thus a remarkably sensitive effective indicator of the lowest levels of metamorphism which is also most important when trying to disentangle primary properties from the metamorphic overprint.

The changes brought about by metamorphism are both time and temperature sensitive so that what is really measured is the net alteration. Nevertheless, this is useful information. In fact, the induced TL does a little more since there are systematic changes in the shape of the glow curve which depend on the temperature at which the feldspar crystalized and the post metamorphic cooling rate. So there is considerable information by combining the induced TL level and the shape of the glow curve.

Basalts are glass-rich rocks, and thick gloves are worn when handling them. Thus one working hypothesis is that Mays samples were increasing in induced TL with time since the glassy phase was crystalizing over time and this was creating more of the TL phosphor.

5. Case study II: Induced TL increases due to the composition of the feldspar

The eucrites are a class of meteorites quite different from the ordinary chondrites. In fact, they are essentially basalts. They are widely thought to have been formed on the large asteroid Vesta, which has a basaltic surface and metal core

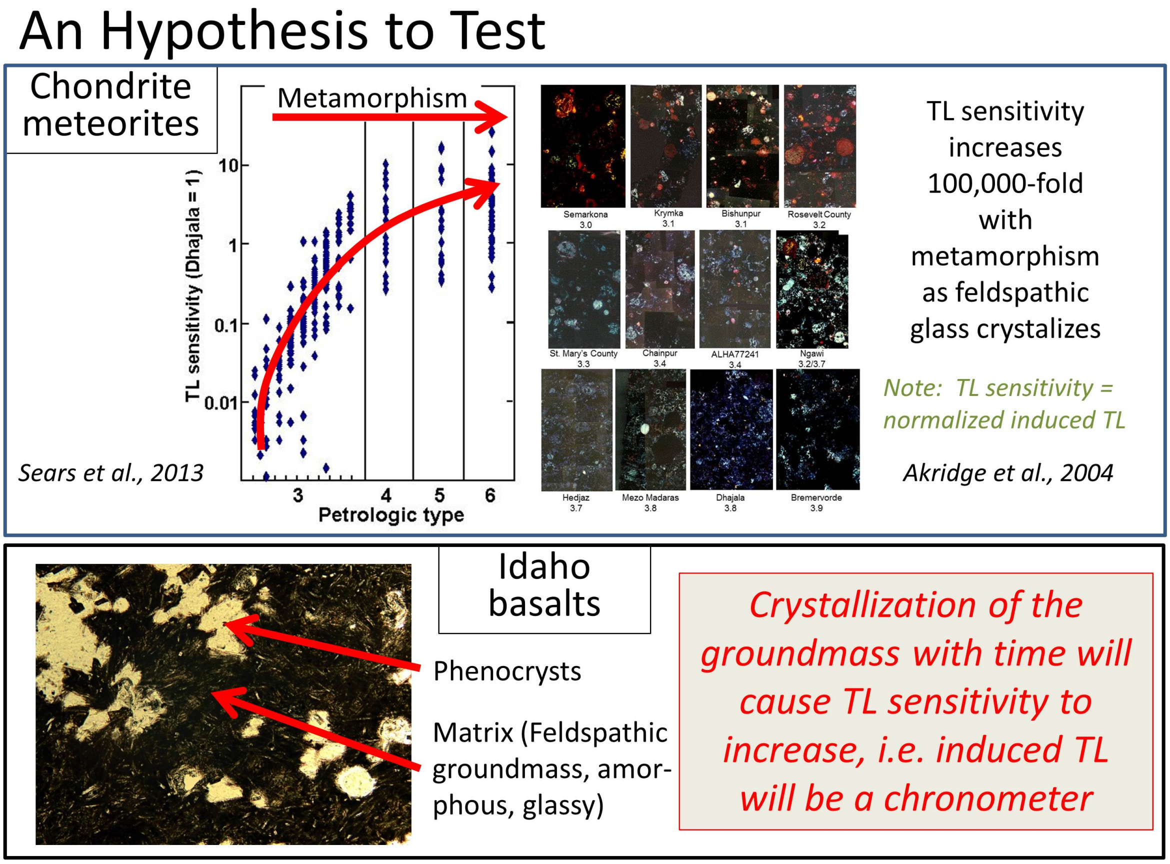

Figure 2. The ordinary chondrite meteorites display a range of alteration due to parent body metamorphism which is described by the "petrologic types", 3 low, 6 high. Thermoluminescence sensitivity increases by a factor of 10^5 over this range of petrologic types (Sears et al., 1980). Cathodoluminescence and other observations indicate that this is due to the formation of the phosphor, feldspar, by the crystallization of glass with feldspathic composition (Akridge et al., 2004; Sears et al., 2013). The analogous situation for the basalts would be the glassy groundmass crystalizing to produce feldspar. This process would be time-dependent and provide a chronometer. The term "TL sensitivity" is used in this and Fig. 3 to mean induced TL of the sample divided the induced TL of a standard meteorite, Dhajala.

(Drake, 2001). In some respects it resembles the Moon, although the details of its igneous history are quite different. However, it is difficult to be sure because of the heavily impacted nature of Vesta's surface. Closely related meteorites are the howardites and diogenites and it is believed the suite of meteorites originated on Vesta, eucrites on the surface, diogenites at depth, perhaps the upper mantle, and the howardites are a mechanical mixture of the two.

Like the chondrites, the eucrites appear to constitute a metamorphic sequence and this has been documented and described in terms of eight "petrologic types". Type 1 has least metamorphic overprint and very heterogeneous mineral compositions; type 8 is most metamorphosed and has homogeneous mineral compositions (Takeda et al., 1983).

The induced TL of a number of eucrites varies over a factor of 100 and correlates with petrologic type (Fig. 3). In this instance, cathodoluminescence and other studies indicated that the cause was not the production of feldspar, but its compositional changes reflecting mineralogical changes caused by metamorphism. In fact, the CL of feldspar in the low type TL was brown/yellow and blotchy while the CL in the high TL samples was a uniform bright yellow. Detailed mineralogical studies showed that that the feldspar in the unmetamorphosed eucrites contained a few percent iron, a known quencher of the TL of feldspar (Geake et al., 1973). With metamorphism, the iron diffused out of the feldspar and moved into other silicate minerals where it was a thermodynamic equilibrium.

Thus we have a second mechanism for explaining May's correlation between induced TL and age. The feldspar in the young basalts contains incompatible quencher elements which diffuse out of the feldspar with time as the rock "equilibrates".

6. Discussion and Conclusions

It is important to keep in mind that rapidly cooled lavas are essentially non-equilibrium assemblages. Thus they contain abundant glass, for instance. Time and elevated temperatures will drive them towards equilibrium, which in our

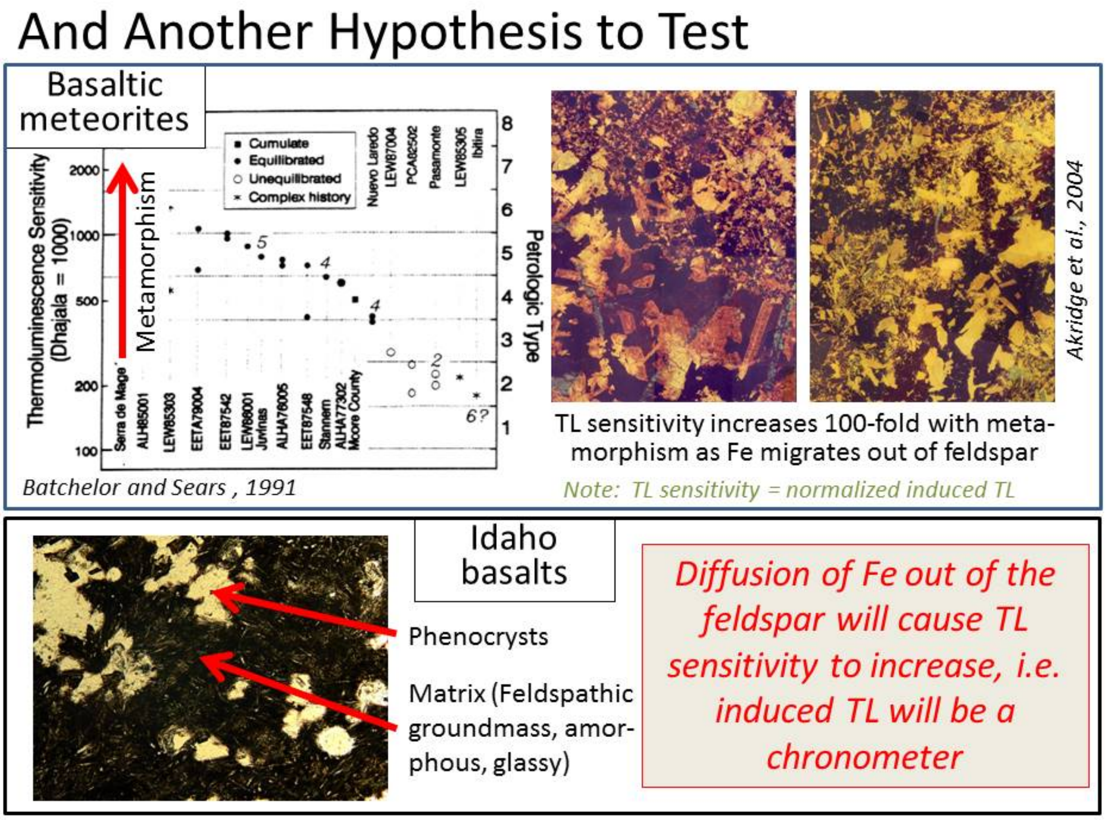

Figure 3. The basaltic meteorites (eucrites, thought to originate on the asteroid Vesta) show a range of metamorphic alteration described by the "petrologic type", 1 low, 6 high. Thermoluminescence sensitivity (induced TL normalized to that of the Dhajala meteorite) shows a factor of 100 range which correlates with petrologic type (Batchelor & Sears, 1991). Catholuminescence images and other data show that this increase in TL sensitivity with metamorphism is a result of Fe diffusing out of the feldspar, little metamorphosed meteorites have feldspar with weak blotchy yellow/brown cathodoluminescence, and highly metamorphosed meteorites have uniform bright yellow cathodoluminescence. Crystals of feldspar in the matrix of terrestrial basalts might increase in induced TL with time as Fe diffuses out of the feldspar.

case means the glass will crystallize and the minerals will achieve "purer" compositions. In the case of terrestrial lavas, once cooled they stay at low temperatures, below 200^{o}C say, so the prime factor controlling the degree of equilibration is time.

It is perfectly possible that both crystallization of the glass and purification the feldspar are playing a part in the time-dependency of the induced TL observed by May. This would not preclude its use as a chronometer. It is possible that by collecting enough data from a variety of sites one could derive an empirical calibration on which to base a technique. Such approaches have been used in the past.

However, it should be possible by performing detailed mineralogical and petrological studies on the basalts of a range of ages to determine whether one of the proposed mechanisms dominates.

It should also be possible to perform laboratory measurements of the kinetics of the process by which induced TL increases. From the kinetics then an absolute dating method should be possible. A variety of sampling sites for the basalts is important because there are many factors that control the rate of equilibration. The amount of water present in the rocks is one, and the composition of the feldspar is another. There are studies of the induced TL properties of the full range of feldspar compositions (Benoit et al., 2001), but not of the kinetics of devitrification of feldspathic glasses.

These are tasks for the future. For the moment I simply wanted to point out that an induced TL procedure might exist for dating lavas that have proved difficult to date using their natural TL because of anomalous fading. Furthermore, this correlation should not be a surprise because similar processes have been found to exist in meteorites, both ordinary chondrites and basaltic meteorites that are, on the face of it, very different rocks. What they have in common is that they all contain feldspar and that feldspar is the dominant luminescent phase in most silicate rocks.

Acknowledgments

I am pleased to acknowledge Scott Hughes who encouraged me in this study, taught me about plains volcanism, and is leading the field work necessary to collect samples and the geological measurements in the laboratory, Yvonne

Pendleton and Jennifer Heldmann who created an environment whereby I could resurrect these long-suppressed ideas and perform some serious work, Hazel Sears and the FINESSE team who helped in the field work, and Hazel also for reviewing and proofing the article. This work was funded by NASA's Solar System Exploration Research Virtual Institute through the FINESSE team, Jennifer Heldmann PI.

References

Aitken, M.J., Fleming, S.J., Doell, R.R., and Tanguy, J.C. *Thermoluminescent study of lavas from Mt Etna and other historic flows: preliminary results.* In *Thermoluminescence of Geological Materials*, pp. 359–366, London and New York, 1968. Academic Press.

Akridge, D.G., Akridge, J.M.C., Batchelor, J.D., Benoit, P.H., Brewer, J., DeHart, J.M., Keck, B. D., Jie, L., Meier, A., Penrose, M., Schneider, D.M., Sears, D.W.G., Symes, S.J.K., and Yanhong, Z. *Photomosaics of the cathodoluminescence of 60 sections of meteorites and lunar samples*. Journal of Geophysical Research, 109: CiteID E07S03, 2004.

Batchelor, J.D. and Sears, D.W.G. *Thermoluminescence constraints on the metamorphic, shock and brecciation history of basaltic meteorites*. Geochimica et Cosmochimica Acta, 55: 3831–3844, 1991.

Benoit, P.H., Hartmetz, C P., Batchelor, D.J., Symes, S.J.K., and Sears, D.W.G. *The induced thermoluminescence and thermal history of plagioclase feldspars*. American Mineralogist, 76: 780–789, 2001.

Drake, M.K. *The eucrite/Vesta story*. Meteoritics and Planetary Science, 36: 501–513, 2001.

Geake, J.E., Walker, G., Telfer, D.J., and Mills, A.A.and Garlick, G.F.J. *Luminescence of lunar, terrestrial, and synthesized plagioclase caused by Mn2+ and Fe3+*. Proceedings of the Lunar Science Conference, 4: 3181–3189, 1973.

Haq, M., Hasan, F.A., and Sears, D.W.G. *Thermoluminescence and the shock and reheating history of meteorites - IV: The induced TL properties of type 4-6 ordinary chondrites*. Geochimica et Cosmochimica Acta, 52: 1679–1689, 1988.

Hartmetz, C.P., Ostertag, R., and Sears, D.W.G. *A thermoluminescence study of experimentally shock-loaded oligoclase and bytownite*. Proc. 17th Lunar and Planet. Sci. Conf., Part 1, J. Geophys. Res., 91: E263–E274, 1986.

Houtermans, F.G. and Liener, A. *Thermoluminescence of Meteorites*. Journal of Geophysical Research, 71: 3387–3396, 1966.

Komovsky, G.F. *Thermoluminescence of stony meteorites*. Meteoritika, 21: 64–69, 1961. (in Russian).

May, R.D. *Thermoluminescence dating of Hawaiian alkali basalts*. Journal of Geophysical Research, 82: 3023–3029, 1977.

May, R.D. *Thermoluminescence dating of Hawaiian basalt*. Geological Survey Professional Paper, 1093: pp47, 1979.

Sears, D.W. *Thermoluminescence of meteorites; relationships with their K-Ar age and their shock and reheating history*. Icarus, 44: 190–206, 1980.

Sears, D.W., Grossman, J.N., Melcher, C.L., Ross, L.M., and Mills, A.A. *Measuring the metamorphic history of unequilibrated ordinary chondrites*. Nature, 287: 791–795, 1980.

Sears, D.W.G., Ninagawa, K., and Singhvi, A.K. *Luminescence studies of extraterrestrial materials: Insights into their recent radiation and thermal histories and into their metamorphic history*. Chemie der Erde - Geochemistry, 73: 1–37, 2013.

Takeda, H., Mori, H., Delaney, J.S., Prinz, M., and Harlow, G.E. *Mineralogical comparison of antarctic and non-antarctic HED (howardites-eucrites-diogenites) achondrites*. In *National Institute of Polar Research, Symposium on Antarctic Meteorites, 8th, Special Issue, no. 30*, pp. 181–205, 1983.

Tsukamoto, S., Duller, G.A.T., Wintle, A.G., and Muhs, D. *Assessing the potential for luminescence dating of basalts.* Quaternary Geochronology, 6: 61–70, 2011.

Van Schmus, W.R. and Wood, J.A. *A chemical-petrologic classification for the chondritic meteorites*. Geochimica et Cosmochimica Acta, 31: 747–765, 1967.

Wintle, A.G. *Anomalous Fading of Thermo-luminescence in Mineral Samples*. Nature, 245: 143–144, 1973. doi: 10.1038/245143a0.

Reviewer

Regina DeWitt

Thesis Abstracts

Index

Alma Arnaboldi	p. 20
Michela Cantù	p. 20
Daniela Constantin	p. 21
Robert R. Hendricks	p. 21
Daniel N. Livsey	p. 22
Loïc Martin	p. 23
Thays Desiree Mineli	p. 23
Ana Luísa Rodrigues dos Santos	p. 24
Kirk F. Townsend	p. 24

Alma Arnaboldi

TL dating applied to Palazzo Raimondi and Palazzo Pallavicino Soldi, Cremona (Italy)

October 2015

Dipartimento di Scienza dei Materiali, Università degli Studi di Milano-Bicocca, and Dipartimento di Fisica, Università degli Studi di Milano (Italy)

Degree: Masters
Supervisors: Anna Galli, Marco Martini, Ivan Veronese

Since the stratigraphic techniques initially developed for archaeology have been extended to the history of architecture, the relative internal sequence of the various building phases of a monument can be usually precisely determined. Their absolute chronology is however sometimes problematic or controversial. In such cases, the contribution of TL dating could be conclusive. It must be remembered, however, that care has to be taken when associating the TL age of a brick to that of its building structure because the date determined is the last firing of the sample. In case of reuse of materials from pre-existing structures, dates are older than the building; in case of upkeep or mimetic restoration, dates are younger. The main advantages of the TL dating of building are the availability of large quantities of material, the homogeneity of environmental radioactivity and the lesser extent of humidity fluctuation.

A recent conservation campaign at the Palazzo Raimondi and Palazzo Pallavicino Soldi, Cremona (Italy) gave the opportunity to sample bricks and mortars belonging to different structures (basement, ground floor and main floor). The relevance of these sites is due to the very old tradition in Cremona in using earthen mortars, materials and execution techniques very rarely employed and studied. This thesis work was aimed at dating the bricks to support the study of the earthen mortars.

TL dating was performed following the standard fine-grain technique using a home-made system based on the photon counting technique with a photomultiplier tube (EMI 9635QB) coupled to blue filters (Corning BG12). Artificial irradiations were carried out by a 1400 MBq ^{90}Sr-^{90}Y beta source (Nominal dose-rate: 1.4 Gy/min) and a 37 MBq ^{241}Am alpha source (Nominal dose-rate: 14.8 Gy/min). Internal annual alpha and beta dose-rates were obtained by total alpha counting with ZnS scintillator discs and flame photometry analysis.

For what concerns Palazzo Raimondi, the calculated ages span in a huge range (300-750 years BP), the Bayesian statistical approach has been applied. The experimental results, all obtained from the basement structure, have been combined in a single formal analysis with the historical boundary corresponding to the foundation. In this way it has been possible to ascribe the fabrication of bricks to the second part of the fifteenth century.

For what concerns Palazzo Pallavicino Soldi the samples belong to different historical periods: the Middle Age (12th century), Renaissance (15th century) and the seventeenth century. The older samples are coeval to a pre-existing structure; the younger samples refer to restoration works documented in archives.

Michela Cantù

Characterization and dating of ancient mortars with additives

December 2015

Università degli Studi di Pavia, Dipartimento di Scienze della Terra e dellAmbiente, Pavia, Italia
and
Dipartimento di Scienza dei Materiali, Univesità degli Studi milano-Bicocca, Milano, Italy

Degree: Ph.D.
Supervisors: Maria Pia Riccardi, Serena Chiara Tarantino, Emanuela Sibilia

In the town of Cremona (Northern Italy) it is very common to find masonries both in rural and historic edifices made of bricks and earthen mortars with good physical and mechanical properties. Aim of this thesis was to carry out an archaeometric study of the earthen mortars from five edifices in Cremona (15th - 19th century) to deepen our information on well-established tradition of production and use of earthen mortars and its evolution throughout centuries. A combination of mineralogical, petrographic and geochemical analyses was used together with the information from historical documents, the latter allowing a precise dating of the analysed samples.

The characterization of the raw materials was carried out by means of optical and electronic microscopy, XRPD and FTIR measurements. The archaeometric investigation allowed the identification of two recipes, differing in the amount of lime (and sometimes sand) added to the basic mixture of earth: the widespread lime-poor earthen mortars and the lime-rich earthen mortars, recognised only in the masonries of Palazzo Magio Grasselli (end of 18^{th} century). Moreover, a two-step technological change in earthen mortars manufacturing that took place between the 17^{th} and 18^{th} century has been recognised: it consisted in the addition of larger amount of lime (from the 17^{th} century) and of organic additives (from the 18th century). This was likely done to improve the mechanical properties of the earthen mortars.

The application of scientific dating methods is of great help in building archaeology, to support and/or validate the information obtained from the historical sources. However, the use of Optically Stimulated Luminescence (OSL) for mortar dating, recently proposed, is not still a routine technique. In the present work OSL was applied to the samples of earthen mortars already well dated on historical ground. To our knowledge, this is the first attempt to extend the applicability of OSL techniques to such materials.

In this case, OSL dating exploits the solar bleaching of quartz grains occurred during the production of mortar. Despite the high quartz content of the analyzed mortars, the solar bleaching efficiency was found not good, probably due to the opacity of the raw materials. In fact, OSL dating multi-grain technique was found unapplicable due to the high amount of poorly bleached grains. The single-grain approach, allowing the selection of the well-bleached grains gave better results and was therefore systematically applied. For data elaboration, several statistical models were used and compared. The simple average and Central Age Model (CAM) significantly overestimated the expected age. The Minimum Age Model (MAM) gave a more accurate evaluation of the equivalent dose. In particular the un-log 3-parameters MAM gave good results on the oldest samples but with large errors. The Internal External Consistency Criterion (IEU) gave generally more precise results, but is less accurate than MAM.

It clearly appeared that another criticality of this application is the recent age of the samples. Further studies are required to improve the efficiency of the low OSL signal detection and to reduce errors associated to the estimated equivalent doses.

Daniela Constantin

On the dating of the last glacial cycle in loess deposits using quartz optically stimulated luminescence

October 2015

Babes-Bolyai University, Cluj-Napoca, Romania

Degree: Ph.D.

Supervisors: Vlad Codrea, Alida Timar-Gabor

Luminescence dating of loess deposits in the Danube Basin and the Chinese Loess Plateau was conducted for the Last Glacial cycle samples using 4-11 μm and 63-90 μm quartz. Ages of older samples are underestimated for all grain sizes. For equivalent doses $>$ 100 Gy (30-40 ka) the fine quartz chronologies underestimate the coarse quartz results.

Single aliquot regenerative dose protocol shows that the laboratory dose response obtained for the two fractions of quartz is different and is fitted with the sum of two exponential functions. The higher saturation in fine grains is not a result of the previous alpha irradiation history and time-resolved (TR-OSL) experiments show that this is not caused by contamination with a different mineral nor it is a consequence of multiple luminescence centres active in the quartz detection window. Laboratory saturation characteristics are not affected by previous irradiation, bleaching, or thermal treatments employed.

For doses $>$ 200 Gy natural and laboratory dose response curves diverge, with natural signals showing earlier saturation. The signals measured on fine quartz after adding thousands of Gy on top of the natural dose are below the saturation level for both Romanian and Chinese quartz samples. Poor dose recovery may, in part, cause age underestimation at high doses. This suggests an initial dose-dependent sensitivity change that is not corrected for by the use of the response to a test dose.

Thus, a dose dependent phenomenon underlies the cause of the age discrepancy. Until the mechanisms of this phenomena are explained both sets of SAR OSL ages are suspected to be inaccurate and question the reported chronologies beyond 30-40 ka.

A summary of the thesis can be downloaded from: http://doctorat.ubbcluj.ro/ro/sustinerile-publice-ale-tezelor-de-doctorat/

Robert R. Hendricks

Timing of the Emplacement of an Ancient Coastal Deposit of Georgia Determined by Optically Stimulated Luminescence and Electron Spin Resonance Optical Dating

December 2015

McMaster University, Hamilton, Canada

Degree: Ph.D.

Supervisor: Dr. W. Jack Rink

ESR, OSL and TT-OSL dating methods were applied to samples collected from six of the Ancient Coastal Deposits (ACDs) along the southern Georgia Coastline. Samples were collected from the Princess Anne (the youngest and most seaward ACD), Pamlico, Talbot, Penholoway, Wicomico, and Okefenokee ACDs with the goal of determining the age of formation of these features. Ground Penetrating Radar

(GPR) was used to determine the subsurface morphology and target lithologies for age determination. OSL and TT-OSL dating was attempted on samples collected from the youngest two ACDs, the Pamlico and Princess Anne, at McMaster Universities AGE Lab. ESR samples collected from all of the ACDs studied were measured at Florida State University as well as Osaka University. ESR analysis measured the Al signal, the Ti-Li signal, measured using two different methods, as well as the Ti-H signal. A number of low additive dose points were added to the ESR dose plan to attempt to create a better dose response curve for the low saturating Ti-H signal in attempt to better utilize the signal.

While the geochronological methodology did not prove useful for determining the age of all of the ACDs it did result in depositional age estimates for the Cypresshead Formation at 433-2978 ka and Satilla Formations at 243-417 ka using the Ti-Li ESR signal as a maximum age estimate. The GPR, ESR, and core data all point to the conclusion that the ACDs of the Georgia Coast are geomorphic modifications and not the result of a unique depositional process. Based on the discrepancy between the depositional age of the Cypresshead and Satilla Formations as determined by ESR in this study and the ages of the ACDs published by others from Georgia (Markewich et.al., 2013) or other areas of the Atlantic Coast (Wehmiller, 2004; Willis, 2006) it can be concluded that paleo sea-levels modified the Cypresshead and Satilla Formations in to the morphology seen today at some point after their initial deposition.

A PDF of this thesis can be downloaded from: https://macsphere.mcmaster.ca/ OR by contacting the author at hendricks.robert.r@gmail.com

Daniel N. Livsey

Holocene sea-level, climate, and estuarine stratrigraphy of Baffin Bay, Texas: studying past changes in coastal systems to elucidate future coastal response to changing sea-level and climate

September 2015

Department of Earth Science at UCSB, Santa Barbara, CA, United States

Degree: Ph.D.
Supervisor: Dr. Alexander Simms

Recent studies along the northwestern Gulf of Mexico document rapid back-stepping of estuarine environments of up to 20 km and 150 m/yr at ca. 8.2 thousand years ago (ka), 4.8, ka, and 2.6 ka. If such rapid changes in coastal environments occurred today along the urbanized coast of the Gulf of Mexico major economical and ecological loss would occur. Of these three backstepping events, only one can be tied to a known cause the 8.2 ka event related to a rapid increase in the rate of relative sea-level rise. However, the cause of the latter two, the 4.8 and 2.6 ka events are largely unknown. To determine the relative roles of changes in sea level and climate in these two events, paleo sea-level, climate, and stratigraphic records, are presented from upper Baffin Bay, Texas and neighboring playa Laguna Salada. This abstract has been abbreviated to highlight the paleoclimate reconstruction that utilizes optically stimulated luminescence (OSL) age-dating for a playa chronology, the portion of the dissertation of specific interest to Ancient TL readers.

Paleoclimate records are sparse along the southern Texas coast. A new quantitative drought proxy is derived from a transfer function between X-Ray Fluorescence (XRF) elemental data from a Texas playa core and a tree-ring drought record. The playa core age-model was based upon twenty-two OSL ages obtained from quartz grains isolated from down-core sand lamina. Lamina sampled for OSL age-dating are characterized by well-sorted, sharp-based sand lamina that are interpreted to have been deposited as subaerial aeolian bedforms observed in the field. Radiocarbon ages were not collected given the paucity of organic matter. Using the transfer function, a 954-year tree-ring drought record was extended to ca. 3,000 ka. Ba, Br, and Pb were utilized as predictor variables. Machine learning algorithms, utilized to derive the transfer function, had maximum validation accuracies of 94%. Changes in the extended drought record correspond with the timing of the Roman Climate Optimum, Medieval Warm Period, Little Ice Age, and changes in North Atlantic sea surface temperatures (SST). Increased drought frequency is coeval with nearby dune migration ca. 0.2 ka, 1.9 ka, and 2.6 ka. The highest drought frequency in the record occurs during the Medieval Warm Period ca. 1.0 ka followed by a decrease in drought frequency during the Little Ice Age ca. 0.4 ka. Increased drought frequency accompanies increased North Atlantic SST since 3 ka. This trend of warm North Atlantic SST and dry conditions over the study area follows secular meteorological observations and tree-ring records. These results indicate that lacustrine derived XRF element data can be used as a quantitative tool to reconstruct past drought records, and that North Atlantic SST modulated drought in southern Texas for the last 3,000 years.

Within Baffin Bay, five flooding surfaces occur through a time-period of ever decreasing rates of relative sea-level rise and within error of periods of drying in southern Texas at ca. 1.0 ka, 2.6 ka, 3.4 ka, 4.8 ka, and 5.5 ka. I hypothesize that these flooding surfaces, occurring when sea level in the Gulf of Mexico was rising $<$ 2 mm/yr, and during independently documented drying events, were primarily driven by changes in climate through declines in fluvial sediment supply to the coast.

A PDF of this thesis can be downloaded from: ProQuest Dissertations & Theses. As of 12-10-15 ProQuest is preparing to make the thesis discoverable.

Loïc Martin

Characterization and modeling of archaeological objects for their dating by Paleo-dosimetric methods. Simulation of the dosimetric parameters with Geant4.

December 2015

Institut de Recherche sur les ArchéoMATériaux (IRAMAT) UMR 5060 CNRS - Université de Bordeaux Montaigne, France

Degree: Ph.D.

Supervisors: Norbert Mercier, Sébastien Incerti

The paleodosimetric dating methods allow to obtain the age of some mineral materials which behave as natural dosimeters, the age being derived as the ratio of the dose accumulated from the dated event and the natural dose rate to which the sample was subjected. The determination of the dose rate is usually based on simple models which only allow explicit calculations, but these models reproduce very imperfectly the diversity of situations encountered. Computer modeling allows to represent more complex and more realistic models, which lead to numerically simulate the dose rate. In this work, the toolbox Geant4, allowing to simulate particle-matter interactions by the Monte-Carlo method, was used to create complex models, as well as modeling tools accessible and adaptable to different types of samples and dosimetric situations.

Simulations were first made with basic models in order to study the origin of dose rate variations in sediments, highlighting the limits of the simple models commonly used. This information was used to guide the development of modeling tools based on the Geant4 codes, and also to specify the protocols of samples analysis for gathering the data needed for numerical simulations.

The DosiVox software allows to easily model a wide variety of samples through a voxelised representation of the object and its environment, and to simulate the radioactivity for calculating the spatial distribution of the dose rate. It was developed with a view of accessibility and current use. Comparisons with dosimetric situations previously studied or measured showed the relevance of the modelings, and the possibilities of this computer tool are exposed through a series of examples and applications.

The characterization of the beta dose rate distribution in heterogeneous sediment is one of the most complex problems to be treated. In addition to a study aims at assessing the potential of DosiVox to consider these situations, the DosiSed software was developed specifically for modeling poly-mineral sets of grains. This tool was used to study the heterogeneity of the dose rate in real samples and allowed to include some of the results in a dating problematic.

Thays Desiree Mineli

Evaluation of the high sensitivity Brazilian quartz as personal dosimeter based on optically stimulated luminescence

April 2015

Faculdade de Engenharia Elétrica e Computação, UNICAMP, Campinas, Brasil

Degree: Masters

Supervisors: Eduardo Tavares Costa; André Oliveira Sawakuchi

The use of ionizing radiation is becoming increasingly frequent, whether in industry or in the medical field. The harmful effects of ionizing radiation require security measures in its use. One of the most common ways to protect the health of the operator of ionizing radiation equipment is controlling the dose that persons can receive in a given time period. Personal dosimeters are used for this purpose. Protocols to estimate equivalent doses using optically stimulated luminescence (OSL) have been developed for determinaton of burial ages of sediments, firing of ceramics and personal dosimetry. Studies on dating of sediments in Brazil have found quartz types with very high luminescence sensitivity and excellent dosimetric characteristics. In order to analyze the dosimetric properties of bright Brazilian quartz and evaluate its potential use in personal dosimetry, comparative tests with the most used personal OSL dosimeter ($Al_2O_3 : C$), were made. This work presents the luminescence characteristics of quartz grains commonly found in fluvial (XNG47.2), eolian (TE65B) and coastal (PIN01) Brazilian samples. High sensitivity quartz and $Al_2O_3 : C$ were compared by dose recovery tests using a Single-Aliquot Regenerative dose protocol (SAR) and signal stability tests in samples exposed to beta (given doses: 50.00 mGy, 0.42 Gy, 35.70 Gy and 49.98 Gy) and gamma radiation (given doses: 0.14 mGy, 4.26 mGy, 8.53 mGy and 42.65 mGy). The luminescence measurements were carried out in Risø TL/OSL DA-20 readers using blue stimulation and light detection in the UV band. The studied quartz samples have average OSL sensitivities (beta radiation) ranging from 0.4% to 2.6% of the average sensitivity of the sample $Al_2O_3 : C$. For gamma radiation, quartz sample TE65B showed sensitivity higher (almost twice) than the sensitivity of the $Al_2O_3 : C$ sample. All the analyzed quartz samples showed measurable OSL signal for doses as low as 5 mGy, indicating that they can measure doses in the mGy range. All quartz samples showed OSL signal increasing linearly with dose up to 1 Gy. The studied quartz samples also were able to recover reliable doses using the OSL signal without correction by a test dose, pointing to a stable signal under thermal, optical and irradiation treatments. Equivalent doses calculated using the Central Age Model and without signal correction for a test dose deviated from 1% to 11% of the given dose. Equivalent doses calculated for the quartz samples have a higher accuracy than the equivalent doses calculated for the $Al_2O_3 : C$ sample. The quartz samples have saturation doses ($2D_0$ = 114-175 Gy) higher than the saturation dose for the $Al_2O_3 : C$ sample ($2D_0$ = 35 Gy). The sensitivity of TE65B quartz sample in gamma radiation test was higher than the sensitivity of the $Al_2O_3 : C$ sample. The quartz samples showed insignificant fading in the period of about 1 month (recovered dose with difference less than 10% of given dose). These results indicate that the studied quartz samples are suitable to recover doses from 50 mGy to 50 Gy have potential as dosimeters and encourage further studies to evaluate the use of this type of quartz as sensor element in personal dosimeters.

Ana Luísa Rodrigues dos Santos

Geochemistry, mineralogy and luminescence studies of a pre-historic negative world - from Neolithic to Bronze Age in Alentejo region (Southern Portugal)

May 2015

Centro de Ciências e Tecnologias Nucleares, Instituto Superior Técnico, Universidade de Lisboa Portugal and Universidade de Aveiro, Aveiro, Portugal

Degree: Ph.D.
Supervisors: Fernando Joaquim Fernandes Tavares Rocha, Maria Isabel Marques Dias, Christopher Ian Burbidge

Archaeological research developed in recent years in South Portugal has revealed negative archaeological structures with original architectures and features, posing questions related to their chronology and fill dynamics. These structures (ditches, pits and hypogeum) have been excavated in carbonate-rich rocks and materials derived by weathering of granites, diorites and associated gabbros. They are related with Pre-Historic societies, from the Neolithic through the Bronze Age. In this work, different granulometric fractions of the fill materials of the negative structures and geological contexts have been studied by an innovative approach comprising: (i) chemical composition (neutron activation analysis and X-ray fluorescence), (ii) mineralogical composition (X-ray diffraction), (iii) thermo and optically stimulated luminescence profiling, and (iv) luminescence dating of fill materials.

Results found for granulometry, chemical and mineralogical composition, particularly of the clay fraction, enable differentiation of the paleoenvironments of the fill materials, as well as classification of the carbonate-rich materials: (i) phreatic calcretes, (ii) lacustrine calcretes (young/mature and poor/rich in Mg) and (iii) carbonate detrital formations. Luminescence together with geochemical and mineralogical results (complementing archaeological ones) contributed to the identification of different phases in the stratigraphic sequence, materials provenance and relation with the geological background, with particular emphasis in the role of trace elements, namely rare earth elements. Luminescence dating is often in accordance with archaeological interpretations of stratigraphy. Nevertheless calcite and/or the contribution of geological materials disturb the obtained age. In order to attenuate the effect of calcite, a new methodological approach is proposed in this work for the dose rate estimation, allowing a re-interpretation of the obtained age.

Thus this work contributes to better establish behaviour of geological materials subjected to natural and anthropogenic weathering effects, in an interdisciplinary point of view, and better understanding the "negative Pre-Historical world" in the Alentejo region.

Kirk F. Townsend

A chronostratigraphic record of arroyo entrenchment and aggradation in Kanab Creek, southern Utah

September 2015

Utah State University, Logan, United States

Degree: Masters
Supervisor: Tammy Rittenour

Arroyos are entrenched channels characterized by near-vertical walls of alluvium and flat channel bottoms. Historic channel entrenchment in the southwest United States during the late AD 1800s and early 1900s has stimulated extensive research on these dynamic fluvial systems. The near-synchronous episodes of arroyo entrenchment and aggradation in Kanab Creek and other drainages in southern Utah during the last $\sim$1 ka has led many researchers to argue that hydroclimatic forcings drive arroyo processes. These hypotheses remain largely untested, and there remains considerable uncertainty regarding the timing of these events and the specific mechanisms responsible for arroyo formation.

Previous work established an alluvial chronology for the Kanab Canyon reach of Kanab Creek, but it remained unclear if arroyo events in this reach were continuous with those downstream or synchronous with events in the disconnected arroyo in the upper basin. Using detailed sedimentologic and stratigraphic descriptions coupled with AMS radiocarbon and optically stimulated luminescence (OSL) dating, a new chronostratigraphic record of arroyo entrenchment and aggradation for Kanab Creek is produced in this study. Results suggest at least five periods of fluvial aggradation and episodic arroyo entrenchment during the middle- to late-Holocene, with aggradation occurring from $\sim$6.2 to 3.6 ka (Qf1), $\sim$3.2 to 2.5 ka (Qf2), $\sim$2.2 to 1.5 ka (Qf3), $\sim$1.4 to 0.8 ka (Qf4), and $\sim$0.75 to 0.14 ka (Qf5). This record is compared to regional alluvial and paleoclimate records to explore potential allogenic and autogenic forcing mechanisms. Rapid transitions from exceptional drought to pluvial periods are quasi-synchronous with regional arroyo entrenchment over the last 1.5 ka, but the lack of clear correlations amongst the regional alluvial records and between paleoclimate records beyond 1.5 ka suggests that internal geomorphic thresholds are important controls on the timing of entrenchment in individual catchments.

Previous research on arroyo dynamics has largely focused on the timing of entrenchment. The few studies that have investigated the processes related to aggradation have used historic observations, and not the stratigraphic record of arroyo deposits. In this study, the alluvial records from three reaches of Kanab Creek are combined to test models of the processes and geometric patterns of paleoarroyo aggradation. Results indicate that aggradation initially propagates upstream and then transitions to synchronous vertical aggradation along the entire channel profile as arroyos approach complete filling.

A PDF of this thesis can be downloaded from: http://digitalcommons.usu.edu/etd/4492/

Bibliography

Compiled by Daniel Richter

From 16th May to 31st November 2015

Abboud, R., Issa, H., Abed-Allah, Y. D., and Bakraji, E. H. (2015). Application of radioisotope XRF and thermoluminescence (TL) dating in investigation of pottery from Tell AL-Kasra archaeological site, Syria. *Applied Radiation and Isotopes* **105,** 47-51.

Ackermann, O., Greenbaum, N., Ayalon, A., Bar-Matthews, M., Boaretto, E., Bruins, H. J., Cabanes, D., Horwitz, L. K., Neumann, F. H., Porat, N., Weiss, E., and Maeir, A. M. (2014). Using palaeo-environmental proxies to reconstruct natural and anthropogenic controls on sedimentation rates, Tell es-Safi/Gath, eastern Mediterranean. *Anthropocene* **8,** 70-82.

Alappat, L., Frechen, M., Sree Kumar, S., Suresh Babu, D. S., Ravur, R., and Tsukamoto, S. (2015). Evidence of Late Holocene shoreline progradation in the coast of Kerala, South India obtained from OSL dating of palaeo-beach ridges. *Geomorphology* **245,** 73-86.

Ames, C. J. H., and Cordova, C. E. (2015). Middle and Late Pleistocene Landscape Evolution at the Druze Marsh Site in Northeast Jordan: Implications for Population Continuity and Hominin Dispersal. *Geoarchaeology* **30,** 307-329.

Antoine, P., Moncel, M. H., Locht, J. L., Limondin-Lozouet, N., Auguste, P., Stoetzel, E., Dabkowski, J., Voinchet, P., Bahain, J. J., and Falgueres, C. (2015). Dating the earliest human occupation of Western Europe: New evidence from the fluvial terrace system of the Somme basin (Northern France). *Quaternary International* **370,** 77-99.

Armitage, S. J., Bristow, C. S., and Drake, N. A. (2015). West African monsoon dynamics inferred from abrupt fluctuations of Lake Mega-Chad. *Proceedings of the National Academy of Sciences* **112,** 8543–8548.

Arnold, L. J., Demuro, M., Parés, J. M., Pérez-González, A., Arsuaga, J. L., Bermúdez de Castro, J. M., and Carbonell, E. (2015). Evaluating the suitability of extended-range luminescence dating techniques over early and Middle Pleistocene timescales: Published datasets and case studies from Atapuerca, Spain. *Quaternary International* **389,** 167-190.

Athanassas, C. D., Rollefson, G. O., Kadereit, A., Kennedy, D., Theodorakopoulou, K., Rowan, Y. M., and Wasse, A. (2015). Optically stimulated luminescence (OSL) dating and spatial analysis of geometric lines in the Northern Arabian Desert. *Journal of Archaeological Science* **64,** 1-11.

Aydas, C., Engin, B., Kapan, S., Komut, T., Aydin, T., and Paksu, U. (2015). Dose estimation, kinetics and dating of fossil marine mollusc shells from northwestern part of Turkey. *Applied Radiation and Isotopes* **105,** 72-79.

Babek, O., Briestensky, M., Precechtelova, G., Stepanoikova, P., Hellstrom, J. C., and Drysdale, R. N. (2015). Pleistocene speleothem fracturing in the foreland of the Western Carpathians: a case study from the seismically active eastern margin of the Bohemian Massif. *Geological Quarterly* **59,** 491-506.

Bezerra, I. S. A. A., Nogueira, A. C. R., Guimarães, J. T. F., and Truckenbrodt, W. (2015). Late pleistocene sea-level changes recorded in tidal and fluvial deposits from Itaubal Formation, onshore portion of the Foz do Amazonas Basin, Brazil. *Brazilian Journal of Geology* **45,** 63-78.

Bickel, L., Lüthgens, C., Lomax, J., and Fiebig, M. (2015). The timing of the penultimate glaciation in the northern Alpine Foreland: new insights from luminescence dating. *Proceedings of the Geologists' Association* **126,** 536-550.

Billy, J., Robin, N., Hein, C. J., Certain, R., and FitzGerald, D. M. (2015). Insight into the late Holocene sea-level changes in the NW Atlantic from a paraglacial beach-ridge plain south of Newfoundland. *Geomorphology* **248,** 134-146.

Bisht, P., Ali, S. N., Shukla, A. D., Negi, S., Sundriyal, Y. P., Yadava, M. G., and Juyal, N. (2015). Chronology of late Quaternary glaciation and landform evolution in the upper Dhauliganga valley, (Trans Himalaya), Uttarakhand, India. *Quaternary Science Reviews* **129,** 147-162.

Blegen, N., Tryon, C. A., Faith, J. T., Peppe, D. J., Beverly, E. J., Li, B., and Jacobs, Z. (2015). Distal tephras of the eastern Lake Victoria basin, equatorial East Africa: correlations, chronology and a context for early modern humans. *Quaternary Science Reviews* **122,** 89-111.

Boixadera, J., Poch, R. M., Lowick, S. E., and Balasch, J. C. (2015). Loess and soils in the eastern Ebro Basin. *Quaternary International* **376,** 114-133.

Brill, D., Jankaew, K., and Brückner, H. (2015). Holocene evolution of Phra Thong's beach-ridge plain (Thailand) — Chronology, processes and driving factors. *Geomorphology* **245,** 117-134.

Brooke, B. P., Pietsch, T. J., Olley, J. M., Sloss, C. R., and Cox, M. E. (2015). A preliminary OSL chronology for coastal dunes on Moreton island, Queensland, Australia - Marginal deposits of A large-scale quaternary shelf sediment system. *Continental Shelf Research* **105,** 79-94.

Burow, C., Kehl, M., Hilgers, A., Weniger, G. C., Angelucci, D. E., Villaverde, V., Zapata, J., and Zilhão, J. (2015). Luminescence Dating of Fluvial Deposits in the Rock Shelter of Cueva Antón, Spain. *Geochronometria* **42,** 107-125.

Cai, S., Chen, W., Tauxe, L., Deng, C., Qin, H., Pan, Y., Yi, L., and Zhu, R. (2015). New constraints on the variation of the geomagnetic field during the late Neolithic period: Archaeointensity results from Sichuan, southwestern China. *Journal of Geophysical Research B: Solid Earth* **120,** 2056-2069.

Campbell, G. E., Walker, R. T., Abdrakhmatov, K., Jackson, J., Elliott, J. R., Mackenzie, D., Middleton, T., and Schwenninger, J. L. (2015). Great earthquakes in low strain rate continental interiors: An example from SE Kazakhstan. *Journal of Geophysical Research: Solid Earth* **120,** 2015JB011925.

Carnicelli, S., Benvenuti, M., Andreucci, S., and Ciampalini, R. (2015). Late Pleistocene relic Ultisols and Alfisols in an alluvial fan complex in coastal Tuscany. *Quaternary International* **376,** 163-172.

Chauhan, N., Choi, J.-H., Kim, J., and Lee, G. (2015). Application of newly developed NCF-SAR protocol to Quaternary sediments from Suncheon and Jeongok, South Korea. *Geosciences Journal* **19,** 407-413.

Chung, K. S., Park, C. Y., Lee, J. I., and Kim, J. L. (2015). An algorithm for the integrated deconvolution of radioluminescence and thermally/optically stimulated luminescence glow curves. *Radiation Measurements* **79,** 7-12.

Clemmensen, L. B., Glad, A. C., Hansen, K. W. T., and Murray, A. S. (2015). Episodes of aeolian sand movement on a large spit system (Skagen Odde, Denmark) and North Atlantic storminess during the Little Ice Age. *Bulletin of the Geological Society of Denmark* **63.**

Combès, B., Philippe, A., Lanos, P., Mercier, N., Tribolo, C., Guerin, G., Guibert, P., and Lahaye, C. (2015). A Bayesian central equivalent dose model for optically stimulated luminescence dating. *Quaternary Geochronology* **28,** 62-70.

Cremaschi, M., Zerboni, A., Nicosia, C., Negrino, F., Rodnight, H., and Spötl, C. (2015). Age, soil-forming processes, and archaeology of the loess deposits at the Apennine margin of the Po plain (northern Italy): New insights from the Ghiardo area. *Quaternary International* **376,** 173-188.

DeJong, B. D., Bierman, P., Newell, W. L., Rittenour, T. M., Mahan, S. A., Balco, G., and Hood, D. R. (2015). Pleistocene relative sea levels in the Chesapeake Bay region and their implications for the next century. *GSA Today* **25,** 4-10.

Demuro, M., Arnold, L. J., Parés, J. M., and Sala, R. (2015). Extended-range luminescence chronologies suggest potentially complex bone accumulation histories at the Early-to-Middle Pleistocene palaeontological site of Huéscar-1 (Guadix-Baza basin, Spain). *Quaternary International* **389,** 191-212.

Dillehay, T. D., Ocampo, C., Saavedra, J., Sawakuchi, A. O., Vega, R. M., Pino, M., Collins, M. B., Scott Cummings, L., Arregui, I., Villagran, X. S., Hartmann, G. A., Mella, M., González, A., and Dix, G. (2015). New Archaeological Evidence for an Early Human Presence at Monte Verde, Chile. *PLoS ONE* **10,** e0141923.

Dimitrijević, V., Mrdjić, N., Korać, M., Chu, S., Kostić, D., Jovičić, M., and Blackwell, B. A. B. (2015). The latest steppe mammoths (Mammuthus trogontherii (Pohlig)) and associated fauna on the Late Middle Pleistocene steppe at Nosak, Kostolac Basin, Northeastern Serbia. *Quaternary International* **379,** 14-27.

Dogan, T., Cetin, H., Yegingil, Z., Topaksu, M., Yüksel, M., Duygun, F., Nur, N., and Yegingil, İ. (2015). Optically stimulated luminescence dating of Holocene alluvial fans, East Anatolian Fault System, Turkey. *Radiation Effects and Defects in Solids* **170,** 630-644.

Dong, Y., Wu, N., Li, F., Huang, L., and Wen, W. (2015). Time-Transgressive Nature of the Magnetic Susceptibility Record across the Chinese Loess Plateau at the Pleistocene/Holocene Transition. *PLoS ONE* **10,** e0133541.

Dragovich, J. D., Mahan, S. A., Anderson, M. L., MacDonald, J. H., Jr, Schilter, J. F., Frattali, C. L., Koger, C. J., Smith, D. T., Stoker, B. A., DuFrane, A., Eddy, M. P., Cakir, R., and Sauer, K. B. (2015). Geologic map of the Lake Roesiger 7.5-minute quadrangle, Snohomish County, Washington: Washington Division of Geology and Earth Resources Map Series 2015-01, 1 sheet, scale 1:24,000, 47 p. text.

Duller, G. A. T., Tooth, S., Barham, L., and Tsukamoto, S. (2015). New investigations at Kalambo Falls, Zambia: Luminescence chronology, site formation, and archaeological significance. *Journal of Human Evolution* **85,** 111-125.

Durcan, J. A., King, G. E., and Duller, G. A. T. (2015). DRAC: Dose Rate and Age Calculator for trapped charge dating. *Quaternary Geochronology* **28,** 54-61.

Duval, M. (2015). Evaluating the accuracy of ESR dose determination of pseudo-Early Pleistocene fossil tooth enamel samples using dose recovery tests. *Radiation Measurements* **79,** 24-32.

Duval, M., Bahain, J.-J., Falguères, C., Garcia, J., Guilarte, V., Grün, R., Martínez, K., Moreno, D., Shao, Q., and Voinchet, P. (2015). Revisiting the ESR chronology of the Early Pleistocene hominin occupation at Vallparadís (Barcelona, Spain). *Quaternary International* **389,** 213-223.

Duval, M., and Guilarte, V. (2015). ESR dosimetry of optically bleached quartz grains extracted from Plio-Quaternary sediment: Evaluating some key aspects of the ESR signals associated to the Ti-centers. *Radiation Measurements* **78,** 28-41.

Duval, M., Sancho, C., Calle, M., Guilarte, V., and Peña-Monné, J. L. (2015). On the interest of using the multiple center approach in ESR dating of optically bleached quartz grains: Some examples from the Early Pleistocene terraces of the Alcanadre River (Ebro basin, Spain). *Quaternary Geochronology* **29,** 58-69.

El-Sayed, A.-M., Tanimura, K., and Shluger, A. L. (2015). Optical signatures of intrinsic electron localization in amorphous SiO 2. *Journal of Physics: Condensed Matter* **27,** 265501.

Fan, L., Huang, C. C., Pang, J., Zha, X., Zhou, Y., Li, X., and Liu, T. (2015). Sedimentary records of palaeofloods in the Wubu Reach along the Jin-Shaan gorges of the middle Yellow River, China. *Quaternary International* **380–381,** 368-376.

Fan, Y., Chen, X., Liu, W., Zhang, F., and Zhang, F. (2015). Formation of present desert landscape surrounding Jilantai Salt Lake in northern China based on OSL dating. *Frontiers of Earth Science* **9,** 497-508.

Fattahi, M. (2015). OSL dating of the Miam Qanat (KĀRIZ) system in NE Iran. *Journal of Archaeological Science* **59,** 54-63.

Fattahi, M., Walker, R., Khatib, M. M., Zarrinkoub, M., and Talebian, M. (2015). Determination of Slip-Rate by Optical Dating of Lake Bed Sediments from the Dasht-E-Bayaz Fault, Ne Iran. *Geochronometria* **42,** 148-157.

Faust, D., Yanes, Y., Willkommen, T., Roettig, C., Richter, D., Richter, D., Suchodoletz, H. v., and Zöller, L. (2015). A contribution to the understanding of late Pleistocene dune sand-paleosol-sequences in Fuerteventura (Canary Islands). *Geomorphology* **246,** 290-304.

Feathers, J. (2015). Luminescence dating at Diepkloof Rock Shelter – new dates from single-grain quartz. *Journal of Archaeological Science* **63,** 164-174.

Fitzsimmons, K. E., Stern, N., Murray-Wallace, C. V., Truscott, W., and Pop, C. (2015). The Mungo Mega-Lake Event, Semi-Arid Australia: Non-Linear Descent into the Last Ice Age, Implications for Human Behaviour. *PLoS ONE* **10,** e0127008.

Forzoni, A., Storms, J. E. A., Reimann, T., Moreau, J., and Jouet, G. (2015). Non-linear response of the Golo River system, Corsica, France, to Late Quaternary climatic and sea level variations. *Quaternary Science Reviews* **121,** 11-27.

Fruergaard, M., Møller, I., Johannessen, P. N., Nielsen, L. H., Andersen, T. J., Nielsen, L., Sander, L., and Pejrup, M. (2015). Stratigraphy, evolution, and controls of a holocene transgressive-regressive barrier island under changing sea level: Danish north sea coast. *Journal of Sedimentary Research* **85,** 820-844.

Fruergaard, M., Piasecki, S., Johannessen, P. N., Noe-Nygaard, N., Andersen, T. J., Pejrup, M., and Nielsen, L. H. (2015). Tsunami propagation over a wide, shallow continental shelf caused by the Storegga slide, southeastern North Sea, Denmark. *Geology* **43,** 1047-1050.

Fujiwara, T., Toyoda, S., Uchida, A., Ishibashi, J. I., Nakai, S., and Takamasa, A. (2015). ESR dating of barite in sea-floor hydrothermal sulfide deposits in the okinawa trough. *In* "Subseafloor Biosphere Linked to Hydrothermal Systems: TAIGA Concept." (J.-i. Ishibashi, K. Okino, and M. Sunamura, Eds.), pp. 369-386.

Geber-Bergstrand, T., Bernhardsson, C., Christiansson, M., Mattsson, S., and Rääf, C. L. (2015). Desiccants for retrospective dosimetry using optically stimulated luminescence (OSL). *Radiation Measurements* **78,** 17-22.

Ghilardi, M., Sanderson, D., Kinnaird, T., Bicket, A., Balossino, S., Parisot, J.-C., Hermitte, D., Guibal, F., and Fleury, J. T. (2015). Dating the bridge at Avignon (south France) and reconstructing the Rhone River fluvial palaeo-landscape in Provence from medieval to modern times. *Journal of Archaeological Science: Reports* **4,** 336-354.

Gong, G., Sun, W., and Xu, H. (2015). Thermoluminescence signal in K-feldspar grains: Revisited. *Applied Radiation and Isotopes* **105,** 80-87.

Gong, Z., Li, S.-H., and Li, B. (2015). Late Quaternary faulting on the Manas and Hutubi reverse faults in the northern foreland basin of Tian Shan, China. *Earth and Planetary Science Letters* **424,** 212-225.

Gong, Z., Sun, J., and Lü, T. (2015). Investigating the components of the optically stimulated luminescence signals of quartz grains from sand dunes in China. *Quaternary Geochronology* **29,** 48-57.

González-Villanueva, R., Pérez-Arlucea, M., Costas, S., Bao, R., Otero, X. L., and Goble, R. (2015). 8000 years of environmental evolution of barrier–lagoon systems emplaced in coastal embayments (NW Iberia). *The Holocene* **25,** 1786-1801.

Greilich, S., Gribenski, N., Mittelstraß, D., Dornich, K., Huot, S., and Preusser, F. (2015). Single-grain dose-distribution measurements by optically stimulated luminescence using an integrated EMCCD-based system. *Quaternary Geochronology* **29,** 70-79.

Groucutt, H. S., White, T. S., Clark-Balzan, L., Parton, A., Crassard, R., Shipton, C., Jennings, R. P., Parker, A. G., Breeze, P. S., Scerri, E. M. L., Alsharekh, A., and Petraglia, M. D. (2015). Human occupation of the Arabian Empty Quarter during MIS 5: Evidence from Mundafan Al-Buhayrah, Saudi Arabia. *Quaternary Science Reviews* **119,** 116-135.

Guibert, P., Brodard, A., Quiles, A., Geneste, J.-M., Baffier, D., Debard, E., and Ferrier, C. (2015). When were the walls of the Chauvet-Pont d'Arc Cave heated? A chronological approach by thermoluminescence. *Quaternary Geochronology* **29,** 36-47.

Guo, Y. J., Li, B., Zhang, J. F., and Roberts, R. G. (2015). Luminescence-based chronologies for Palaeolithic sites in the Nihewan Basin, northern China: First tests using newly developed optical dating procedures for potassium feldspar grains. *Journal of Archaeological Science: Reports* **3,** 31-40.

Guralnik, B., Jain, M., Herman, F., Ankjærgaard, C., Murray, A. S., Valla, P. G., Preusser, F., King, G. E., Chen, R., Lowick, S. E., Kook, M., and Rhodes, E. J. (2015). OSL-thermochronometry of feldspar from the KTB borehole, Germany. *Earth and Planetary Science Letters* **423,** 232-243.

Gusev, E. A., Molodkov, A. N., and Derevyanko, L. G. (2015). Sopochnaya Karga mammoth, time and environment conditions of its habitat (North of West Siberia). *Advances in Current Natural Sciences* **1,** 432–435.

Hall, S. A., and Goble, R. J. (2015). OSL age and stratigraphy of the Strauss sand sheet in New Mexico, USA. *Geomorphology* **241,** 42-54.

Han, Z., Li, X., Yi, S., Stevens, T., Chen, Y., Wang, X., and Lu, H. (2015). Extreme monsoon aridity episodes recorded in South China during Heinrich Events. *Palaeogeography, Palaeoclimatology, Palaeoecology* **440,** 467-474.

Harangi, S., Lukacs, R., Schmitt, A. K., Dunkl, I., Molnar, K., Kiss, B., Seghedi, I., Novothny, A., and Molnar, M. (2015). Constraints on the timing of Quaternary volcanism and duration of magma residence at Ciomadul volcano, east-central Europe, from combined U-Th/He and U-Th zircon geochronology. *Journal of Volcanology and Geothermal Research* **301,** 66-80.

Harmand, D., Voinchet, P., Cordier, S., Bahain, J.-J., and Rixhon, G. (2015). Datations ESR de terrasses alluviales des vallées de la Moselle et de la Meurthe (France, Allemagne) : implications chronostratigraphiques et limites méthodologiques. *Quaternaire* **26,** 13-26.

He, Z., Zhang, X., Bao, S., Qiao, Y., Sheng, Y., Liu, X., He, X., Yang, X., Zhao, J., Liu, R., and Lu, C. (2015). Multiple climatic cycles imprinted on regional uplift-controlled fluvial terraces in the lower Yalong River and Anning River, SE Tibetan Plateau. *Geomorphology* **250,** 95-112.

Hede, M. U., Sander, L., Clemmensen, L. B., Kroon, A., Pejrup, M., and Nielsen, L. (2015). Changes in Holocene relative sea-level and coastal morphology: A study of a raised beach ridge system on Samsø, southwest Scandinavia. *Holocene* **25,** 1402-1414.

Hernandez, M., and Mercier, N. (2015). Characteristics of the post-blue VSL signal from sedimentary quartz. *Radiation Measurements* **78,** 1-8.

Hu, G., Yi, C.-L., Zhang, J.-F., Liu, J.-H., and Jiang, T. (2015). Luminescence dating of glacial deposits near the eastern Himalayan syntaxis using different grain-size fractions. *Quaternary Science Reviews* **124,** 124-144.

Hughes, K., Croke, J., Bartley, R., Thompson, C., and Sharma, A. (2015). Alluvial terrace preservation in the Wet Tropics, northeast Queensland, Australia. *Geomorphology* **248,** 311-326.

Ishibashi, J. I., Shimada, K., Sato, F., Uchida, A., Toyoda, S., Takamasa, A., Nakai, S., Hyodo, H., Sato, K., Kumagai, H., and Ikehata, K. (2015). Dating of hydrothermal mineralization in active hydrothermal fields in the Southern Mariana trough. *In* "Subseafloor Biosphere Linked to Hydrothermal Systems: TAIGA Concept." (J.-i. Ishibashi, K. Okino, and M. Sunamura, Eds.), pp. 289-300.

Ito, K., Tamura, T., Hasebe, N., Nakamura, T., Arai, S., Ogata, M., Itono, T., and Kashiwaya, K. (2015). Comparison of Luminescence Dating Methods on Lake Sediments from a Small Catchment: Example from Lake Yogo, Japan. *In* "Earth Surface Processes and Environmental Changes in East Asia." (K. Kashiwaya, J. Shen, and J. Y. Kim, Eds.), pp. 221-238. Springer Japan.

Jacobs, Z., and Roberts, R. G. (2015). An improved single grain OSL chronology for the sedimentary deposits from Diepkloof Rockshelter, Western Cape, South Africa. *Journal of Archaeological Science* **63,** 175-192.

Jia, F., Lu, R., Gao, S., Li, J., and Liu, X. (2015). Holocene aeolian activities in the southeastern Mu Us Desert, China. *Aeolian Research* **19, Part B,** 267-274.

Jiang, H., Shevenell, A., Yu, S., Xu, H., and Mao, X. (2015). Decadal- to centennial-scale East Asian summer monsoon variability during the Medieval Climate Anomaly reconstructed from an eastern Tibet lacustrine sequence. *Journal of Paleolimnology* **54,** 205-222.

Jin, M., Li, G., Li, F., Duan, Y., Wen, L., Wei, H., Yang, L., Fan, Y., and Chen, F. (2015). Holocene shorelines and lake evolution in Juyanze Basin, southern Mongolian Plateau, revealed by luminescence dating. *The Holocene* **25,** 1898-1911.

Jochems, A. P., and Pederson, J. L. (2015). Active salt deformation and rapid, transient incision along the Colorado River near Moab, Utah. *Journal of Geophysical Research F: Earth Surface* **120,** 730-744.

Kalińska-Nartiša, E., Thiel, C., Nartišs, M., Buylaert, J.-P., and Murray, A. S. (2015). Age and sedimentary record of inland eolian sediments in Lithuania, NE European Sand Belt. *Quaternary Research* **84,** 82-95.

Kearfott, K. J., and West, W. G. (2015). An affordable optically stimulated luminescent dosimeter reader utilizing multiple excitation wavelengths. *Applied Radiation and Isotopes* **104,** 87-99.

Kendrick, K. J., Matti, J. C., and Mahan, S. A. (2015). Late Quaternary slip history of the Mill Creek strand of the San Andreas fault in San Gorgonio Pass, southern California: The role of a subsidiary left-lateral fault in strand switching. *Geological Society of America Bulletin* **127,** 825-849.

Khan, M. S. H., Haque, M. M., Pati, P., Chowdhury, K. R., and Biswas, S. (2015). OSL derived uplift rate of Dakhin Nhila anticline along the southeastern coast of the Bay of Bengal, Bangladesh. *Himalayan Geology* **36,** 143-152.

Kim, J. C., Chang, T. S., Yi, S., Hong, S. S., and Nahm, W.-H. (2015). OSL dating of coastal sediments from the southwestern Korean Peninsula: A comparison of different size fractions of quartz. *Quaternary International* **384,** 82-90.

Kim, M. J., Lee, Y. J., Lee, J. I., Kim, J. L., and Hong, D. G. (2015). Fading test using the SAAD-POSL method for retrospective accidental dosimetry of building materials. *Radiation Physics and Chemistry* **116,** 373-376.

Kitis, G., Kiyak, N. G., and Polymeris, G. S. (2015). Temperature lags of luminescence measurements in a commercial luminescence reader. *Nuclear Instruments and Methods in Physics Research Section B: Beam Interactions with Materials and Atoms* **359,** 60-63.

Kondopoulou, D., Aidona, E., Ioannidis, N., Polymeris, G. S., and Tsolakis, S. (2015). Archaeomagnetic study and thermoluminescence dating of Protobyzantine kilns (Megali Kypsa, North Greece). *Journal of Archaeological Science: Reports* **2,** 156-168.

Kraushaar, S., Ollesch, G., Siebert, C., Vogel, H.-J., and Fuchs, M. (2015). Long-Term Sediment Export Estimates from Northern Jordan using Roman Cisterns as Sediment Traps. *Geoarchaeology* **30,** 369-378.

Layzell, A. L., Mandel, R. D., Ludvigson, G. A., Rittenour, T. M., and Smith, J. J. (2015). Forces driving late Pleistocene (ca. 77–12 ka) landscape evolution in the Cimarron River valley, southwestern Kansas. *Quaternary Research* **84,** 106-117.

Leonard, S., and Nott, J. (2015). Rapid Cycles of Episodic Adjustment: Understanding the Holocene fluvial archive of the Daintree River of Northeastern Australia. *The Holocene* **25,** 1208-1219.

Li, G., Jin, M., Chen, X., Wen, L., Zhang, J., Madsen, D., Zhao, H., Wang, X., Fan, T., Duan, Y., Liu, X., Wu, D., Li, F., and Chen, F. (2015). Environmental changes in the Ulan Buh Desert, southern Inner Mongolia, China since the middle Pleistocene based on sedimentology, chronology and proxy indexes. *Quaternary Science Reviews* **128,** 69-80.

Li, G., Jin, M., Duan, Y., Madsen, D. B., Li, F., Yang, L., Wei, H., and Chen, F. (2015). Quartz and K-feldspar luminescence dating of a Marine Isotope Stage 5 megalake in the Juyanze Basin, central Gobi Desert, China. *Palaeogeography, Palaeoclimatology, Palaeoecology* **440,** 96-109.

Li, G., Wen, L., Xia, D., Duan, Y., Rao, Z., Madsen, D. B., Wei, H., Li, F., Jia, J., and Chen, F. (2015). Quartz OSL and K-feldspar pIRIR dating of a loess/paleosol sequence from arid central Asia, Tianshan Mountains, NW China. *Quaternary Geochronology* **28,** 40-53.

Li, K., Xu, X.-W., Tan, X.-B., Chen, G.-H., Xu, C., and Kang, W.-J. (2015). Late Quaternary deformation of the Longquan anticline in the Longmenshan thrust belt, eastern Tibet, and its tectonic implication. *Journal of Asian Earth Sciences* **112,** 1-10.

Liritzis, I., Aravantinos, V., Polymeris, G. S., Zacharias, N., Fappas, I., Agiamarniotis, G., Sfampa, I. K., Vafiadou, A., and Kitis, G. (2015). Witnessing prehistoric Delphi by luminescence dating. *Comptes Rendus Palevol* **14,** 219-232.

Liu, T., Huang, C. C., Pang, J., Zha, X., Zhou, Y., Zhang, Y., and Ji, L. (2015). Late Pleistocene and Holocene palaeoflood events recorded by slackwater deposits in the upper Hanjiang River valley, China. *Journal of Hydrology* **529, Part 2,** 499-510.

Liu, T., Huang, C. C., Pang, J., Zhou, Y., Zhang, Y., Ji, L., and Shang, R. (2014). Extraordinary hydro-climatic events during 1800–1600 yr BP in the Jin–Shaan Gorges along the middle Yellow River, China. *Palaeogeography, Palaeoclimatology, Palaeoecology* **410,** 143-152.

Liu, W., Lai, Z., Hu, K., Ge, Y., Cui, P., Zhang, X., and Liu, F. (2015). Age and extent of a giant glacial-dammed lake at Yarlung Tsangpo gorge in the Tibetan Plateau. *Geomorphology* **246,** 370-376.

Lokier, S. W., Bateman, M. D., Larkin, N. R., Rye, P., and Stewart, J. R. (2015). Late Quaternary sea-level changes of the Persian Gulf. *Quaternary Research* **84,** 69-81.

Long, H., Shen, J., Wang, Y., Gao, L., and Frechen, M. (2015). High-resolution OSL dating of a late Quaternary sequence from Xingkai Lake (NE Asia): Chronological challenge of the "MIS 3a Mega-paleolake" hypothesis in China. *Earth and Planetary Science Letters* **428,** 281-292.

López Steinmetz, R. L., and Galli, C. I. (2015). Hydrological change during the pleistocene-holocene transition associated with the last glacial maximum-altithermal in the eastern border of northern Puna. *Andean Geology* **42,** 1-19.

Lopez-Recio, M., Silva, P. G., Roquero, E., Cunha, P. P., Tapias, F., Alcaraz-Castano, M., Baena, J., Cuartero, F., Morin, J., Torres, T., Ortiz, J. E., Murray, A. S., and Buylaert, J. P. (2015). Geochronology of the Acheulean sites of Pinedo and Cien Fanegas (Tagus River valley), and implications for the fluvial evolution in the environs of Toledo (Spain). *Estudios Geologicos-Madrid* **71,** e029.

Lowick, S. E., Buechi, M. W., Gaar, D., Graf, H. R., and Preusser, F. (2015). Luminescence dating of Middle Pleistocene proglacial deposits from northern Switzerland: methodological aspects and stratigraphical conclusions. *Boreas* **44,** 459-482.

Lu, R., Jia, F., Gao, S., Shang, Y., Li, J., and Zhao, C. (2015). Holocene aeolian activity and climatic change in Qinghai Lake basin, northeastern Qinghai–Tibetan Plateau. *Palaeogeography, Palaeoclimatology, Palaeoecology* **430,** 1-10.

Mackay, A., Jacobs, Z., and Steele, T. E. (2015). Pleistocene Archaeology and Chronology of Putslaagte 8 (PL8) Rockshelter, Western Cape, South Africa. *Journal of African Archaeology* **13,** 71-98.

Macklin, M. G., Panyushkina, I. P., Toonen, W. H. J., Chang, C., Tourtellotte, P. A., Duller, G. A. T., Wang, H., and Prins, M. A. (2015). The influence of Late Pleistocene geomorphological inheritance and Holocene hydromorphic regimes on floodwater farming in the Talgar catchment, southeast Kazakhstan, Central Asia. *Quaternary Science Reviews* **129,** 85-95.

Matmon, A., Hidy, A. J., Vainer, S., Crouvi, O., Fink, D., Erel, Y., Horwitz, L. K., Chazan, M., and Team, A. (2015). New chronology for the southern Kalahari Group sediments with implications for sediment-cycle dynamics and early hominin occupation. *Quaternary Research* **84,** 118-132.

May, J. H., Barrett, A., Cohen, T. J., Jones, B. G., Price, D., and Gliganic, L. A. (2015). Late Quaternary evolution of a playa margin at Lake Frome, South Australia. *Journal of Arid Environments* **122,** 93-108.

May, J.-H., Plotzki, A., Rodrigues, L., Preusser, F., and Veit, H. (2015). Holocene floodplain soils along the Río Mamoré, northern Bolivia, and their implications for understanding inundation and depositional patterns in seasonal wetland settings. *Sedimentary Geology* **330,** 74-89.

May, S. M., Brill, D., Engel, M., Scheffers, A., Pint, A., Opitz, S., Wennrich, V., Squire, P., Kelletat, D., and Brückner, H. (2015). Traces of historical tropical cyclones and tsunamis in the Ashburton Delta (north-west Australia). *Sedimentology* **62,** 1546-1572.

McIntosh, P. D. (2015). Comments on the paper "Stratigraphy and geochronology of Quaternary marine terraces of Tasmania, Southeastern Australia: implications on neotectonism" by Jaeryul Shin, Geosciences Journal, 17, 429-443. *Geosciences Journal* **19,** 575-578.

Mendes, V. R., Giannini, P. C. F., Guedes, C. C. F., DeWitt, R., and De Abreu Andrade, H. A. (2015). Central santa catarina coastal dunefields chronology and their relation to relative sea level and climatic changes. *Brazilian Journal of Geology* **45,** 79-95.

Miao, X., Wang, H., Hanson, P. R., Mason, J. A., and Liu, X. (2016). A new method to constrain soil development time using both OSL and radiocarbon dating. *Geoderma* **261,** 93-100.

Möller, P., and Murray, A. S. (2015). Drumlinised glaciofluvial and glaciolacustrine sediments on the Småland peneplain, South Sweden – new information on the growth and decay history of the Fennoscandian Ice Sheets during MIS 3. *Quaternary Science Reviews* **122,** 1-29.

Moran, K. L., Mallinson, D. J., Culver, S. J., Leorri, E., and Mulligan, R. P. (2014). Late Holocene Evolution of Currituck Sound, North Carolina, USA: Environmental Change Driven by Sea-Level Rise, Storms, and Barrier Island Morphology. *Journal of Coastal Research* **31,** 827-841.

Murton, J. B., Goslar, T., Edwards, M. E., Bateman, M. D., Danilov, P. P., Savvinov, G. N., Gubin, S. V., Ghaleb, B., Haile, J., Kanevskiy, M., Lozhkin, A. V., Lupachev, A. V., Murton, D. K., Shur, Y., Tikhonov, A., Vasil'chuk, A. C., Vasil'chuk, Y. K., and Wolfe, S. A. (2015). Palaeoenvironmental Interpretation of Yedoma Silt (Ice Complex) Deposition as Cold-Climate Loess, Duvanny Yar, Northeast Siberia. *Permafrost and Periglacial Processes* **26,** 208-288.

Nadel, D., Bar-Oz, G., Malkinson, D., Spivak, P., Langgut, D., Porat, N., Khechoyan, A., Nachmias, A., Crater-Gershtein, E., Katinaa, A., Bermatov-Paz, G., Nahapetyan, S., and Gasparyan, B. (2015). New insights into desert kites in Armenia: The fringes of the Ararat Depression. *Arabian Archaeology and Epigraphy* **26,** 120-143.

Nascimento, A. F., Furquim, S. A. C., Graham, R. C., Beirigo, R. M., Oliveira Junior, J. C., Couto, E. G., and Vidal-Torrado, P. (2015). Pedogenesis in a Pleistocene fluvial system of the Northern Pantanal - Brazil. *Geoderma* **255,** 58-72.

Nelson, A. R., Briggs, R. W., Dura, T., Engelhart, S. E., Gelfenbaum, G., Bradley, L.-A., Forman, S. L., Vane, C. H., and Kelley, K. A. (2015). Tsunami recurrence in the eastern Alaska-Aleutian arc: A Holocene stratigraphic record from Chirikof Island, Alaska. *Geosphere* **11,** 1172-1203.

Nijhuis, A. G., Edmonds, D. A., Caldwell, R. L., Cederberg, J. A., Slingerland, R. L., Best, J. L., Parsons, D. R., and Robinson, R. A. J. (2015). Fluvio-deltaic avulsions during relative sea-level fall. *Geology* **43,** 719-722.

Nosenko, V. V., Vorona, I. P., Baran, N. P., Ishchenko, S. S., Vysotskyi, B. V., Krakhmalnaya, T. V., and Semenov, Y. A. (2015). Comparative EPR study CO2− radicals in modern and fossil tooth enamel. *Radiation Measurements* **78,** 53-57.

Nottebaum, V., Lehmkuhl, F., Stauch, G., Lu, H., and Yi, S. (2015). Late Quaternary aeolian sand deposition sustained by fluvial reworking and sediment supply in the Hexi Corridor — An example from northern Chinese drylands. *Geomorphology* **250,** 113-127.

Ogundare, F. O., and Chithambo, M. L. (2013). Characteristics of luminescence lifetimes in natural quartz from Brazil and South Korea. *Radiation Effects & Defects in Solids: Incorporating Plasma Techniques & Plasma Phenomena* **168,** 460-467.

Oniya, E. O. (2015). Dependence of heating rates of thermal activation on thermal activation characteristics of 110 °C TL peak of quartz: A simulation approach. *Radiation Physics and Chemistry* **115,** 171-178.

Panin, A., Adamiec, G., and Filippov, V. (2015). Fluvial response to proglacial effects and climate in the upper Dnieper valley (Western Russia) during the Late Weichselian and the Holocene. *Quaternaire* **26,** 27-48.

Parenti, F. (2015). Old and new on the same site: Putting Vale da Pedra Furada into a wider context. A comment to Lahaye et al. 2015. *Quaternary Geochronology* **30, Part A,** 48-53.

Peña-Monné, J. L., Sancho-Marcén, C., Sampietro-Vattuone, M. M., Rivelli, F., Rhodes, E. J., Osácar-Soriano, M. C., Rubio-Fernández, V., and García-Giménez, R. (2015). Geomorphological study of the Cafayate dune field (Northwest Argentina) during the last millennium. *Palaeogeography, Palaeoclimatology, Palaeoecology* **438,** 352-363.

Peng, J., Dong, Z., and Han, F. (2016). Optically stimulated luminescence dating of sandy deposits from Gulang county at the southern margin of the Tengger Desert, China. *Journal of Arid Land* **8,** 1-12.

Pereira, A., Nomade, S., Voinchet, P., Bahain, J. J., Falguères, C., Garon, H., Lefèvre, D., Raynal, J. P., Scao, V., and Piperno, M. (2015). The earliest securely dated hominin fossil in Italy and evidence of Acheulian occupation during glacial MIS 16 at Notarchirico (Venosa, Basilicata, Italy). *Journal of Quaternary Science* **30,** 639-650.

Poręba, G. J., Śnieszko, Z., and Moska, P. (2015). Application of OSL dating and ^{137}Cs measurements to reconstruct the history of water erosion: A case study of a Holocene colluvium in Świerklany, south Poland. *Quaternary International* **374,** 189-197.

Qiu, F., and Zhou, L. (2015). A new luminescence chronology for the Mangshan loess-palaeosol sequence on the southern bank of the Yellow River in Henan, central China. *Quaternary Geochronology* **30, Part A,** 24-33.

Rades, E. F., Tsukamoto, S., Frechen, M., Xu, Q., and Ding, L. (2015). A lake-level chronology based on feldspar luminescence dating of beach ridges at Tangra Yum Co (southern Tibet). *Quaternary Research* **83,** 469-478.

Rémillard, A. M., Hétu, B., Bernatchez, P., Buylaert, J.-P., Murray, A. S., St-Onge, G., and Geach, M. (2015). Chronology and palaeoenvironmental implications of the ice-wedge pseudomorphs and composite-wedge casts on the Magdalen Islands (eastern Canada). *Boreas* **44,** 658-675.

Richter, D., Klinger, P., and Zöller, L. (2015). Palaeodose underestimation of heated quartz in Red-TL dating of volcanic contexts. *Geochronometria* **42,** 182-188.

Richter, D., Richter, A., and Dornich, K. (2015). lexsyg smart - a luminescence detection system for dosimetry, material research and dating application. *Geochronometria* **42,** 202-209.

Rink, W. J., and López, G. I. (2015). Corrigendum to "OSL-based lateral progradation and aeolian sediment accumulation rates for the Apalachicola Barrier Island Complex, North Gulf of Mexico, Florida" [Geomorphology 123 (2010) 330–342]. *Geomorphology* **241,** 41.

Roskin, J., Sivan, D., Shtienberg, G., Roskin, E., Porat, N., and Bookman, R. (2015). Natural and human controls of the Holocene evolution of the beach, aeolian sand and dunes of Caesarea (Israel). *Aeolian Research* **19, Part A,** 65-85.

Roskosch, J., Tsukamoto, S., and Frechen, M. (2015). Luminescence Dating of Fluvial Deposits from the Weser Valley, Germany. *Geochronometria* **42,** 126-138.

Rossetti, D. F., Cohen, M. C. L., Tatumi, S. H., Sawakuchi, A. O., Cremon, É. H., Mittani, J. C. R., Bertani, T. C., Munita, C. J. A. S., Tudela, D. R. G., Yee, M., and Moya, G. (2015). Mid-Late Pleistocene OSL chronology in western Amazonia and implications for the transcontinental Amazon pathway. *Sedimentary Geology* **330,** 1-15.

Sabtu, S. N., Mahat, R. H., Amin, Y. M., Price, D. M., Bradley, D. A., and Maah, M. J. (2015). Thermoluminescence dating analysis at the site of an ancient brick structure at Pengkalan Bujang, Malaysia. *Applied Radiation and Isotopes* **105,** 182-187.

Salcher, B. C., Starnberger, R., and Götz, J. (2015). The last and penultimate glaciation in the North Alpine Foreland: New stratigraphical and chronological data from the Salzach glacier. *Quaternary International* **388,** 218-231.

Scherler, D., Bookhagen, B., Wulf, H., Preusser, F., and Strecker, M. R. (2015). Increased late Pleistocene erosion rates during fluvial aggradation in the Garhwal Himalaya, northern India. *Earth and Planetary Science Letters* **428,** 255-266.

Schmidt, C., Kindermann, K., van Peer, P., and Bubenzer, O. (2015). Multi-emission luminescence dating of heated chert from the Middle Stone Age sequence at Sodmein Cave (Red Sea Mountains, Egypt). *Journal of Archaeological Science* **63,** 94-103.

Schuldenrein, J. (2015). Refining landscape contexts for open-air, Lower and Middle Paleolithic sites: a case study from Muthanna Province, Southern Iraq. *Archaeological and Anthropological Sciences* **7,** 257-273.

Sebe, K., Roetzel, R., Fiebig, M., and Lüthgens, C. (2015). Pleistocene wind system in eastern Austria and its impact on landscape evolution. *CATENA* **134,** 59-74.

Sewell, R. J., Parry, S., Millis, S. W., Wang, N., Rieser, U., and DeWitt, R. (2015). Dating of debris flow fan complexes from Lantau Island, Hong Kong, China: The potential relationship between landslide activity and climate change. *Geomorphology* **248,** 205-227.

Sfampa, I. K., Polymeris, G. S., Pagonis, V., Theodosoglou, E., Tsirliganis, N. C., and Kitis, G. (2015). Correlation of basic TL, OSL and IRSL properties of ten K-feldspar samples of various origins. *Nuclear Instruments and Methods in Physics Research Section B: Beam Interactions with Materials and Atoms* **359,** 89-98.

Shen, J., Wang, Y., and Zhu, Y. (2015). OSL Chronology of the Sand Hills of Xingkai Lake, Northeast China and Its Implication for Environmental Changes Since 200 kyr BP. *In* "Earth Surface Processes and Environmental Changes in East Asia." (K. Kashiwaya, J. Shen, and J. Y. Kim, Eds.), pp. 45-61. Springer Japan.

Shi, X., Kirby, E., Furlong, K. P., Meng, K., Robinson, R., and Wang, E. (2015). Crustal strength in central Tibet determined from Holocene shoreline deflection around Siling Co. *Earth and Planetary Science Letters* **423,** 145-154.

Shin, J. (2013). Stratigraphy and geochronology of quaternary marine terraces of Tasmania, Southeastern Australia: implications on neotectonism. *Geosciences Journal* **17,** 429-443.

Sier, M. J., Peeters, J., Dekkers, M. J., Parés, J. M., Chang, L., Busschers, F. S., Cohen, K. M., Wallinga, J., Bunnik, F. P. M., and Roebroeks, W. (2015). The Blake Event recorded near the Eemian type locality – A diachronic onset of the Eemian in Europe. *Quaternary Geochronology* **28,** 12-28.

Simkins, L. M., Simms, A. R., and Dewitt, R. (2015). Assessing the link between coastal morphology, wave energy and sea ice throughout the Holocene from Antarctic raised beaches. *Journal of Quaternary Science* **30,** 335-348.

Singh, S. J., Karmakar, M., and Singh, S. D. (2013). On the determination of the order of kinetics in thermoluminescence by peak-shape method. *Radiation Effects & Defects in Solids: Incorporating Plasma Techniques & Plasma Phenomena* **168,** 352-357.

Sitzia, L., Bertran, P., Bahain, J.-J., Bateman, M. D., Hernandez, M., Garon, H., de Lafontaine, G., Mercier, N., Leroyer, C., Queffelec, A., and Voinchet, P. (2015). The Quaternary coversands of southwest France. *Quaternary Science Reviews* **124,** 84-105.

Smedley, R. K., Duller, G. A. T., and Roberts, H. M. (2015). Bleaching of the post-IR IRSL signal from individual grains of K-feldspar: Implications for single-grain dating. *Radiation Measurements* **79,** 33-42.

Sneed, M., Orlando, P. v. P., Borchers, J. W., Everett, R., Solt, M., McGann, M., Lowers, H., and Mahan, S. (2015). Lithostratigraphic, borehole-geophysical, hydrogeologic, and hydrochemical data from the East Bay Plain, Alameda County, California. *In* "Data Series." pp. 68, Reston, VA.

Sohbati, R., Murray, A. S., Porat, N., Jain, M., and Avner, U. (2015). Age of a prehistoric "Rodedian" cult site constrained by sediment and rock surface luminescence dating techniques. *Quaternary Geochronology* **30, Part A,** 90-99.

Solongo, S., Ochir, A., Tengis, S., Fitzsimmons, K., and Hublin, J.-J. (2015). Luminescence dating of mortar and terracotta from a Royal Tomb at Ulaankhermiin Shoroon Bumbagar, Mongolia. *Science and Technology of Archaeological Research* **1,** STAR2015112054892315Y.0000000008; DOI: 10.1179/2054892315Y.0000000008.

Solongo, S., and Tengis, S. (2015). The feldspar pIRIR and quartz OSL on silty-clay sediments from walled ramparts in Orkhon Valley, Mongolia. *Quaternary Geochronology* **30, Part A,** 18-23.

Tankersley, K. B., Murari, M. K., Crowley, B. E., Owen, L. A., Storrs, G. W., and Mortensen, L. (2015). Quaternary chronostratigraphy and stable isotope paleoecology of Big Bone Lick, Kentucky, USA. *Quaternary Research* **83,** 479-487.

Tema, E., Polymeris, G., Morales, J., Goguitchaichvili, A., and Tsaknaki, V. (2015). Dating of ancient kilns: A combined archaeomagnetic and thermoluminescence analysis applied to a brick workshop at Kato Achaia, Greece. *Journal of Cultural Heritage* **16,** 496-507.

Thiel, C., Tsukamoto, S., Tokuyasu, K., Buylaert, J.-P., Murray, A. S., Tanaka, K., and Shirai, M. (2015). Testing the application of quartz and feldspar luminescence dating to MIS 5 Japanese marine deposits. *Quaternary Geochronology* **29,** 16-29.

Timar-Gabor, A., Constantin, D., Marković, S. B., and Jain, M. (2015). Extending the area of investigation of fine versus coarse quartz optical ages from the Lower Danube to the Carpathian Basin. *Quaternary International* **388,** 168-176.

Toyoda, S., Banerjee, D., Kumagai, H., Miyazaki, J., Ishibashi, J.-i., Mochizuki, N., and Kojima, S. (2015). Gamma Ray Doses in Water Around Sea Floor Hydrothermal Area in the Southern Mariana Trough. *In* "Subseafloor Biosphere Linked to Hydrothermal Systems." (J.-i. Ishibashi, K. Okino, and M. Sunamura, Eds.), pp. 603-606. Springer Japan.

Tribolo, C., Rasse, M., Soriano, S., and Huysecom, E. (2015). Defining a chronological framework for the Middle Stone Age in West Africa: Comparison of methods and models for OSL ages at Ounjougou (Mali). *Quaternary Geochronology* **29,** 80-96.

Varma, V., Toyoda, S., Isono, Y., Uchida, A., Banerjee, D., Singhvi, A., and Ishibashi, J.-i. (2015). OSL Dating of Sea Floor Sediments at the Okinawa Trough. *In* "Subseafloor Biosphere Linked to Hydrothermal Systems." (J.-i. Ishibashi, K. Okino, and M. Sunamura, Eds.), pp. 617-620. Springer Japan.

Veit, H., Preusser, F., and Trauerstein, M. (2015). The Southern Westerlies in Central Chile during the two last glacial cycles as documented by coastal aeolian sand deposits and intercalating palaeosols. *CATENA* **134,** 30-40.

Voinchet, P., Moreno, D., Bahain, J.-J., Tissoux, H., Tombret, O., Falguères, C., Moncel, M.-H., Schreve, D., Candy, I., Antoine, P., Ashton, N., Beamish, M., Cliquet, D., Despriée, J., Lewis, S., Limondin-Lozouet, N., Locht, J.-L., Parfitt, S., and Pope, M. (2015). New chronological data (ESR and ESR/U-series) for the earliest Acheulian sites of north-western Europe. *Journal of Quaternary Science* **30,** 610-622.

Wang, J., Chen, G., Peng, Z., and Grapes, R. (2015). Loess-like deposits in the Pearl River delta area, southeast China. *Aeolian Research* **19, Part A,** 113-122.

Wang, X., Vandenberghe, J., Yi, S., Van Balen, R., and Lu, H. (2015). Climate-dependent fluvial architecture and processes on a suborbital timescale in areas of rapid tectonic uplift: An example from the NE Tibetan Plateau. *Global and Planetary Change* **133,** 318-329.

Wang, X., Yi, S., Lu, H., Vandenberghe, J., and Han, Z. (2015). Aeolian process and climatic changes in loess records from the northeastern Tibetan Plateau: Response to global temperature forcing since 30 ka. *Paleoceanography* **30,** 612-620.

Winsemann, J., Lang, J., Roskosch, J., Polom, U., Böhner, U., Brandes, C., Glotzbach, C., and Frechen, M. (2015). Terrace styles and timing of terrace formation in the Weser and Leine valleys, northern Germany: Response of a fluvial system to climate change and glaciation. *Quaternary Science Reviews* **123,** 31-57.

Xu, H., Jiang, H., Yu, S., Yang, H., and Chen, J. (2015). OSL and pollen concentrate ^{14}C dating of dammed lake sediments at Maoxian, east Tibet, and implications for two historical earthquakes in AD 638 and 952. *Quaternary International* **371,** 290-299.

Xu, S., Ding, X., Yu, L., and Ni, Z. (2015). Palaeoclimatic implications of aeolian sediments on the Miaodao Islands, Bohai Sea, East China, based on OSL dating and proxies. *Aeolian Research* **19, Part B,** 259-266.

Xu, Z., Lu, H., Yi, S., Vandenberghe, J., Mason, J. A., Zhou, Y., and Wang, X. (2015). Climate-driven changes to dune activity during the Last Glacial Maximum and deglaciation in the Mu Us dune field, north-central China. *Earth and Planetary Science Letters* **427,** 149-159.

Yu, L., Lai, Z., An, P., Pan, T., and Chang, Q. (2015). Aeolian sediments evolution controlled by fluvial processes, climate change and human activities since LGM in the Qaidam Basin, Qinghai-Tibetan Plateau. *Quaternary International* **372,** 23-32.

Zamora-Camacho, A., Manuel Espindola, J., Schaaf, P., Ramirez, A., and Godinez Calderon, M. d. L. (2015). Evidence of pre-Columbian settlements in the forest of the Tuxtla Volcanic Field, Veracruz, Mexico. *Geofisica Internacional* **54,** 277-287.

Zerboni, A., Trombino, L., Frigerio, C., Livio, F., Berlusconi, A., Michetti, A., Rodnight, H., and Spötl, C. (2015). The loess-paleosol sequence at Monte Netto: a record of climate change in the Upper Pleistocene of the central Po Plain, northern Italy. *Journal of Soils and Sediments* **15,** 1329-1350.

Zha, X., Huang, C., Pang, J., Liu, J., and Xue, X. (2015). Reconstructing the palaeoflood events from slackwater deposits in the upper reaches of Hanjiang River, China. *Quaternary International* **380–381,** 358-367.

Zhang, J., Feng, J.-L., Hu, G., Wang, J., Yang, Y., Lin, Y., Jiang, T., and Zhu, L. (2015). Holocene proglacial loess in the Ranwu valley, southeastern Tibet, and its paleoclimatic implications. *Quaternary International* **372,** 9-22.

Zhang, J., Nottebaum, V., Tsukamoto, S., Lehmkuhl, F., and Frechen, M. (2015). Late Pleistocene and Holocene loess sedimentation in central and western Qilian Shan (China) revealed by OSL dating. *Quaternary International* **372,** 120-129.

Zhou, L., Jin, Z., Wang, C.-H., Li, F., Wang, Y., Wang, X., Zhang, F., Chen, L., and Du, J. (2015). Otolith microchemistry of modern versus well-dated ancient naked carp Gymnocypris przewalskii: Implication for water evolution of Lake Qinghai. *Journal of Asian Earth Sciences* **105,** 399-407.

Zuccarello, A. R., Caputo, R., Gueli, A. M., Bianca, M., and Troja, S. O. (2015). New ESR ages for Piano San Nicola site, Gulf of Taranto, Italy. *Bollettino Di Geofisica Teorica Ed Applicata* **56,** 425-434.

Proceedings of the LED 14 held in Montreal in July 2014

Quaternary Geochronology, Volume 30/B

al Khasawneh, S., Murray, A., Bonatz, D., and Freiesleben, T. (2015). Testing the application of post IR IRSL dating to Iron- and Viking-age ceramics and heated stones from Denmark. *Quaternary Geochronology* **30, Part B,** 386-391.

Alexanderson, H., and Henriksen, M. (2015). A short-lived aeolian event during the Early Holocene in southeastern Norway. *Quaternary Geochronology* **30, Part B,** 175-180.

Armitage, S. J. (2015). Optically stimulated luminescence dating of Ocean Drilling Program core 658B: Complications arising from authigenic uranium uptake and lateral sediment movement. *Quaternary Geochronology* **30, Part B,** 270-274.

Arnold, L. J., and Demuro, M. (2015). Insights into TT-OSL signal stability from single-grain analyses of known-age deposits at Atapuerca, Spain. *Quaternary Geochronology* **30, Part B,** 472-478.

Bahain, J.-J., Falguères, C., Laurent, M., Dolo, J.-M., Shao, Q., Auguste, P., and Tuffreau, A. (2015). ESR/U-series dating of faunal remains from the paleoanthropological site of Biache-Saint-Vaast (Pas-de-Calais, France). *Quaternary Geochronology* **30, Part B,** 541-546.

Bailiff, I. K., Gerrard, C. M., Gutiérrez, A., Snape-Kennedy, L. M., and Wilkinson, K. N. (2015). Luminescence dating of irrigation systems: Application to a qanat in Aragón, Spain. *Quaternary Geochronology* **30, Part B,** 452-459.

Balescu, S., Huot, S., Mejri, H., Barré, M., Forget Brisson, L., Lamothe, M., and Oueslati, A. (2015). Luminescence dating of Middle Pleistocene (MIS 7) marine shoreline deposits along the eastern coast of Tunisia: A comparison of K-feldspar and Na-feldspar IRSL ages. *Quaternary Geochronology* **30, Part B,** 288-293.

Bartz, M., Klasen, N., Zander, A., Brill, D., Rixhon, G., Seeliger, M., Eiwanger, J., Weniger, G.-C., Mikdad, A., and Brückner, H. (2015). Luminescence dating of ephemeral stream deposits around the Palaeolithic site of Ifri n'Ammar (Morocco). *Quaternary Geochronology* **30, Part B,** 460-465.

Bateman, M. D., Stein, S., Ashurst, R. A., and Selby, K. (2015). Instant luminescence chronologies? High resolution luminescence profiles using a portable luminescence reader. *Quaternary Geochronology* **30, Part B,** 141-146.

Biswas, R. H., Toyoda, S., Takada, M., and Shitaoka, Y. (2015). Multiple approaches to date Japanese marker tephras using optical and ESR methods. *Quaternary Geochronology* **30, Part B,** 350-356.

Buylaert, J.-P., Yeo, E.-Y., Thiel, C., Yi, S., Stevens, T., Thompson, W., Frechen, M., Murray, A., and Lu, H. (2015). A detailed post-IR IRSL chronology for the last interglacial soil at the Jingbian loess site (northern China). *Quaternary Geochronology* **30, Part B,** 194-199.

Chen, Y., Li, S.-H., Li, B., Hao, Q., and Sun, J. (2015). Maximum age limitation in luminescence dating of Chinese loess using the multiple-aliquot MET-pIRIR signals from K-feldspar. *Quaternary Geochronology* **30, Part B,** 207-212.

ChongYi, E., Lai, Z., Hou, G., Cao, G., Sun, Y., Wang, Y., and Jiang, Y. (2015). Age determination for a Neolithic site in northeastern Qinghai-Tibetan Plateau using a combined luminescence and radiocarbon dating. *Quaternary Geochronology* **30, Part B,** 411-415.

Colarossi, D., Duller, G. A. T., Roberts, H. M., Tooth, S., and Lyons, R. (2015). Comparison of paired quartz OSL and feldspar post-IR IRSL dose distributions in poorly bleached fluvial sediments from South Africa. *Quaternary Geochronology* **30, Part B,** 233-238.

Falguères, C., Shao, Q., Han, F., Bahain, J. J., Richard, M., Perrenoud, C., Moigne, A. M., and Lumley de, H. (2015). New ESR and U-series dating at Caune de l'Arago, France: A key-site for European Middle Pleistocene. *Quaternary Geochronology* **30, Part B,** 547-553.

Fan, A., Jin, Z., Liu, Y., Li, S., ZhangSun, Y., and Wu, Y. (2015). OSL chronology of traditional zinc smelting activity in Yunnan province, southwest China. *Quaternary Geochronology* **30, Part B,** 369-373.

Feathers, J. K., and Pagonis, V. (2015). Dating quartz near saturation – Simulations and application at archaeological sites in South Africa and South Carolina. *Quaternary Geochronology* **30, Part B,** 416-421.

Forget Brisson, L., Lamothe, M., Huot, S., Hardy, F., and Chapdelaine, C. (2015). Optical dating of St. Lawrence Iroquoian ceramics from the Mailhot-Curran site, southern Québec. *Quaternary Geochronology* **30, Part B,** 392-397.

Fu, X., Li, S.-H., and Li, B. (2015). Optical dating of aeolian and fluvial sediments in north Tian Shan range, China: Luminescence characteristics and methodological aspects. *Quaternary Geochronology* **30, Part B,** 161-167.

Fuchs, M., Dietze, M., Al-Qudah, K., and Lomax, J. (2015). Dating desert pavements – First results from a challenging environmental archive. *Quaternary Geochronology* **30, Part B,** 342-349.

Geach, M. R., Thomsen, K. J., Buylaert, J. P., Murray, A. S., Mather, A. E., Telfer, M. W., and Stokes, M. (2015). Single-grain and multi-grain OSL dating of river terrace sediments in the Tabernas Basin, SE Spain. *Quaternary Geochronology* **30, Part B,** 213-218.

Han, F., Bahain, J.-J., Liu, C., and Yin, G. (2015). Testing mathematical uranium migration models in combined ESR/U-series dating of fossil teeth from open-air sites. *Quaternary Geochronology* **30, Part B,** 519-523.

Hernandez, M., Bahain, J.-J., Mercier, N., Tombret, O., Falguères, C., and Jaubert, J. (2015). Dating results on sedimentary quartz, bones and teeth from the Middle Pleistocene archaeological site of Coudoulous I (Lot, SW France): A comparative study between TT-OSL and ESR/U-series methods. *Quaternary Geochronology* **30, Part B,** 493-497.

Hood, A. G. E., and Schwenninger, J.-L. (2015). The minimum extraction technique: A new sampling methodology for optically stimulated luminescence dating of museum ceramics. *Quaternary Geochronology* **30, Part B,** 381-385.

Hou, G., Lai, Z., Cao, G., E, C., Sun, Y., Rhode, D., and James, F. (2015). The earliest prehistoric pottery in the Qinghai-Tibetan Plateau and its archaeological implications. *Quaternary Geochronology* **30, Part B,** 431-437.

Jin, Z. Y., Wu, Y. J., Fan, A. C., Yue, Z. W., Li, G., Li, S. H., and Yan, L. F. (2015). Luminescence study of the initial, pre-casting firing temperatures of clay mould and core used for bronze casting at Yinxu (13c. BC~11c. BC). *Quaternary Geochronology* **30, Part B,** 374-380.

Kang, S., Wang, X., Lu, Y., Liu, W., Song, Y., and Wang, N. (2015). A high-resolution quartz OSL chronology of the Talede loess over the past ~30 ka and its implications for dust accumulation in the Ili Basin, Central Asia. *Quaternary Geochronology* **30, Part B,** 181-187.

Kenzler, M., Tsukamoto, S., Meng, S., Thiel, C., Frechen, M., and Hüneke, H. (2015). Luminescence dating of Weichselian interstadial sediments from the German Baltic Sea coast. *Quaternary Geochronology* **30, Part B,** 251-256.

Kim, J. C., Cheong, D., Shin, S., Park, Y.-H., and Hong, S. S. (2015). OSL chronology and accumulation rate of the Nakdong deltaic sediments, southeastern Korean Peninsula. *Quaternary Geochronology* **30, Part B,** 245-250.

Kinnaird, T. C., Sanderson, D. C. W., and Bigelow, G. F. (2015). Feldspar SARA IRSL dating of very low dose rate aeolian sediments from Sandwick South, Unst, Shetland. *Quaternary Geochronology* **30, Part B,** 168-174.

Kristensen, J. A., Thomsen, K. J., Murray, A. S., Buylaert, J.-P., Jain, M., and Breuning-Madsen, H. (2015). Quantification of termite bioturbation in a savannah ecosystem: Application of OSL dating. *Quaternary Geochronology* **30, Part B,** 334-341.

Lahaye, C., Guérin, G., Boëda, E., Fontugne, M., Hatté, C., Frouin, M., Clemente-Conte, I., Pino, M., Felice, G. D., Guidon, N., Lourdeau, A., Pagli, M., Pessis, A. M., and Da Costa, A. (2015). New insights into a late-Pleistocene human occupation in America: The Vale da Pedra Furada complete chronological study. *Quaternary Geochronology* **30, Part B,** 445-451.

Liu, C.-R., Yin, G.-M., and Han, F. (2015). Effects of grain size on quartz ESR dating of Ti–Li center in fluvial and lacustrine sediments. *Quaternary Geochronology* **30, Part B,** 513-518.

Liu, Z., Zhao, H., Wang, C.-M., and Li, S.-H. (2015). Estimation of paleo-firing temperatures using luminescence signals for the volcanic lava baked layer in Datong, China. *Quaternary Geochronology* **30, Part B,** 363-368.

Mahan, S. A., Martin, F. W., and Taylor, C. (2015). Construction ages of the Upton Stone Chamber: Preliminary findings and suggestions for future luminescence research. *Quaternary Geochronology* **30, Part B,** 422-430.

May, J.-H., Preusser, F., and Gliganic, L. A. (2015). Refining late Quaternary plunge pool chronologies in Australia's monsoonal 'Top End'. *Quaternary Geochronology* **30, Part B,** 328-333.

McGuire, C., and Rhodes, E. J. (2015). Downstream MET-IRSL single-grain distributions in the Mojave River, southern California: Testing assumptions of a virtual velocity model. *Quaternary Geochronology* **30, Part B,** 239-244.

Meng, Y.-M., Zhang, J.-F., Qiu, W.-L., Fu, X., Guo, Y.-J., and Zhou, L.-P. (2015). Optical dating of the Yellow River terraces in the Mengjin area (China): First results. *Quaternary Geochronology* **30, Part B,** 219-225.

Moreno, D., Falguères, C., Pérez-González, A., Voinchet, P., Ghaleb, B., Despriée, J., Bahain, J.-J., Sala, R., Carbonell, E., Bermúdez de Castro, J. M., and Arsuaga, J. L. (2015). New radiometric dates on the lowest stratigraphical section (TD1 to TD6) of Gran Dolina site (Atapuerca, Spain). *Quaternary Geochronology* **30, Part B,** 535-540.

Morthekai, P., Chauhan, P. R., Jain, M., Shukla, A. D., Rajapara, H. M., Krishnan, K., Sant, D. A., Patnaik, R., Reddy, D. V., and Singhvi, A. K. (2015). Thermally re-distributed IRSL (RD-IRSL): A new possibility of dating sediments near B/M boundary. *Quaternary Geochronology* **30, Part B,** 154-160.

Nentwig, V., Tsukamoto, S., Frechen, M., and Bahlburg, H. (2015). Reconstructing the tsunami record in Tirúa, Central Chile beyond the historical record with quartz-based SAR-OSL. *Quaternary Geochronology* **30, Part B,** 299-305.

Neudorf, C. M., Lian, O. B., Walker, I. J., Shugar, D. H., Eamer, J. B. R., and Griffin, L. C. M. (2015). Toward a luminescence chronology for coastal dune and beach deposits on Calvert Island, British Columbia central coast, Canada. *Quaternary Geochronology* **30, Part B,** 275-281.

Nian, X., Chen, F., Li, F., and Gao, X. (2015). Optical dating of a Paleolithic site near the eastern coastal region of Shandong, northern China. *Quaternary Geochronology* **30, Part B,** 466-471.

Ou, X., Duller, G. A. T., Roberts, H. M., Zhou, S., Lai, Z., Chen, R., Chen, R., and Zeng, L. (2015). Single grain optically stimulated luminescence dating of glacial sediments from the Baiyu Valley, southeastern Tibet. *Quaternary Geochronology* **30, Part B,** 314-319.

Rémillard, A. M., Buylaert, J. P., Murray, A. S., St-Onge, G., Bernatchez, P., and Hétu, B. (2015). Quartz OSL dating of late Holocene beach ridges from the Magdalen Islands (Quebec, Canada). *Quaternary Geochronology* **30, Part B,** 264-269.

Richard, M., Falguères, C., Pons-Branchu, E., Bahain, J. J., Voinchet, P., Lebon, M., Valladas, H., Dolo, J. M., Puaud, S., Rué, M., Daujeard, C., Moncel, M. H., and Raynal, J. P. (2015). Contribution of ESR/U-series dating to the chronology of late Middle Palaeolithic sites in the middle Rhône valley, southeastern France. *Quaternary Geochronology* **30, Part B,** 529-534.

Rittenour, T. M., Cotter, J. F. P., and Arends, H. E. (2015). Application of single-grain OSL dating to ice-proximal deposits, glacial Lake Benson, west-central Minnesota, USA. *Quaternary Geochronology* **30, Part B,** 306-313.

Rui, X., Zhang, J.-F., Hou, Y.-M., Yang, Z.-M., Liu, Y., Zhen, Z.-M., and Zhou, L.-P. (2015). Feldspar multi-elevated-temperature post-IR IRSL dating of the Wulanmulun Paleolithic site and its implication. *Quaternary Geochronology* **30, Part B,** 438-444.

Shao, Q., Bahain, J.-J., Wang, W., Zhu, M., Voinchet, P., Lin, M., and Douville, E. (2015). Coupled ESR and U-series dating of early Pleistocene Gigantopithecus faunas at Mohui and Sanhe Caves, Guangxi, southern China. *Quaternary Geochronology* **30, Part B,** 524-528.

Shen, H., Yu, L., Zhang, H., Zhao, M., and Lai, Z. (2015). OSL and radiocarbon dating of flood deposits and its paleoclimatic and archaeological implications in the Yihe River Basin, East China. *Quaternary Geochronology* **30, Part B,** 398-404.

Song, Y., Lai, Z., Li, Y., Chen, T., and Wang, Y. (2015). Comparison between luminescence and radiocarbon dating of late Quaternary loess from the Ili Basin in Central Asia. *Quaternary Geochronology* **30, Part B,** 405-410.

Stone, A. E. C., Bateman, M. D., and Thomas, D. S. G. (2015). Rapid age assessment in the Namib Sand Sea using a portable luminescence reader. *Quaternary Geochronology* **30, Part B,** 134-140.

Sugisaki, S., Buylaert, J.-P., Murray, A., Tada, R., Zheng, H., Ke, W., Saito, K., Chao, L., Li, S., and Irino, T. (2015). OSL dating of fine-grained quartz from Holocene Yangtze delta sediments. *Quaternary Geochronology* **30, Part B,** 226-232.

Tamura, T., Sawai, Y., and Ito, K. (2015). OSL dating of the AD 869 Jogan tsunami deposit, northeastern Japan. *Quaternary Geochronology* **30, Part B,** 294-298.

Toyoda, S. (2015). Paramagnetic lattice defects in quartz for applications to ESR dating. *Quaternary Geochronology* **30, Part B,** 498-505.

Trandafir, O., Timar-Gabor, A., Schmidt, C., Veres, D., Anghelinu, M., Hambach, U., and Simon, S. (2015). OSL dating of fine and coarse quartz from a Palaeolithic sequence on the Bistrița Valley (Northeastern Romania). *Quaternary Geochronology* **30, Part B,** 487-492.

Voinchet, P., Toyoda, S., Falguères, C., Hernandez, M., Tissoux, H., Moreno, D., and Bahain, J. J. (2015). Evaluation of ESR residual dose in quartz modern samples, an investigation on environmental dependence. *Quaternary Geochronology* **30, Part B,** 506-512.

Wang, Y., Long, H., Yi, L., Yang, L., Ye, X., and Shen, J. (2015). OSL chronology of a sedimentary sequence from the inner-shelf of the East China Sea and its implication on post-glacial deposition history. *Quaternary Geochronology* **30, Part B,** 282-287.

Yang, L., Long, H., Yi, L., Li, P., Wang, Y., Gao, L., and Shen, J. (2015). Luminescence dating of marine sediments from the Sea of Japan using quartz OSL and polymineral pIRIR signals of fine grains. *Quaternary Geochronology* **30, Part B,** 257-263.

Yi, S., Buylaert, J.-P., Murray, A. S., Thiel, C., Zeng, L., and Lu, H. (2015). High resolution OSL and post-IR IRSL dating of the last interglacial–glacial cycle at the Sanbahuo loess site (northeastern China). *Quaternary Geochronology* **30, Part B,** 200-206.

Zhang, J., Tsukamoto, S., Nottebaum, V., Lehmkuhl, F., and Frechen, M. (2015). De plateau and its implications for post-IR IRSL dating of polymineral fine grains. *Quaternary Geochronology* **30, Part B,** 147-153.

Zhang, J.-F., Huang, W.-W., Hu, Y., Yang, S.-X., and Zhou, L.-P. (2015). Optical dating of flowstone and silty carbonate-rich sediments from Panxian Dadong Cave, Guizhou, southwestern China. *Quaternary Geochronology* **30, Part B,** 479-486.

Zhao, H., Li, S.-H., Li, B., and Li, G.-Q. (2015). Holocene climate changes in westerly-dominated areas of central Asia: Evidence from optical dating of two loess sections in Tianshan Mountain, China. *Quaternary Geochronology* **30, Part B,** 188-193.

Zhao, H., Liu, Z., Wang, C.-M., and Li, S.-H. (2015). Luminescence dating of volcanic eruptions in Datong, northern China. *Quaternary Geochronology* **30, Part B,** 357-362.

Zhao, Q., Thomsen, K. J., Murray, A. S., Wei, M., Pan, B., Song, B., Zhou, R., Chen, S., Zhao, X., and Chen, H. (2015). Testing the use of OSL from quartz grains for dating debris flows in Miyun, northeast Beijing, China. *Quaternary Geochronology* **30, Part B,** 320-327.

Radiation Measurements, Volume 81

Ankjærgaard, C., Guralnik, B., Porat, N., Heimann, A., Jain, M., and Wallinga, J. (2015). Violet stimulated luminescence: geo- or thermochronometer? *Radiation Measurements* **81,** 78-84.

Bluszcz, A., Adamiec, G., and Heer, A. J. (2015). Estimation of equivalent dose and its uncertainty in the OSL SAR protocol when count numbers do not follow a Poisson distribution. *Radiation Measurements* **81,** 46-54.

Chen, R., and Pagonis, V. (2015). Study of the stability of the TL and OSL signals. *Radiation Measurements* **81,** 192-197.

Chithambo, M. L. (2015). Luminescence lifetimes in natural quartz annealed beyond its second phase inversion temperature. *Radiation Measurements* **81,** 198-204.

Chruścińska, A. (2015). Estimating the parameters of traps in quartz by the variable energy of stimulation optically stimulated luminescence (VES-OSL) method. *Radiation Measurements* **81,** 205-211.

Constantin, D., Jain, M., Murray, A. S., Buylaert, J.-P., and Timar-Gabor, A. (2015). Quartz luminescence response to a mixed alpha-beta field: Investigations on Romanian loess. *Radiation Measurements* **81,** 110-115.

Cunningham, A. C., Evans, M., and Knight, J. (2015). Quantifying bleaching for zero-age fluvial sediment: A Bayesian approach. *Radiation Measurements* **81,** 55-61.

Duller, G. A. T., Kook, M., Stirling, R. J., Roberts, H. M., and Murray, A. S. (2015). Spatially-resolved thermoluminescence from snail opercula using an EMCCD. *Radiation Measurements* **81,** 157-162.

Duval, M., Campaña, I., Guilarte, V., Miguens, L., Iglesias, J., and González Sierra, S. (2015). Assessing the uncertainty on particle size and shape: Implications for ESR and OSL dating of quartz and feldspar grains. *Radiation Measurements* **81,** 116-122.

Freiesleben, T., Sohbati, R., Murray, A., Jain, M., al Khasawneh, S., Hvidt, S., and Jakobsen, B. (2015). Mathematical model quantifies multiple daylight exposure and burial events for rock surfaces using luminescence dating. *Radiation Measurements* **81,** 16-22.

Frouin, M., Huot, S., Mercier, N., Lahaye, C., and Lamothe, M. (2015). The issue of laboratory bleaching in the infrared-radiofluorescence dating method. *Radiation Measurements* **81,** 212-217.

Gribenski, N., Preusser, F., Greilich, S., Huot, S., and Mittelstraß, D. (2015). Investigation of cross talk in single grain luminescence measurements using an EMCCD camera. *Radiation Measurements* **81,** 163-170.

Guérin, G., Combès, B., Lahaye, C., Thomsen, K. J., Tribolo, C., Urbanova, P., Guibert, P., Mercier, N., and Valladas, H. (2015). Testing the accuracy of a Bayesian central-dose model for single-grain OSL, using known-age samples. *Radiation Measurements* **81,** 62-70.

Guérin, G., and Visocekas, R. (2015). Volcanic feldspars anomalous fading: Evidence for two different mechanisms. *Radiation Measurements* **81,** 218-223.

Guralnik, B., Li, B., Jain, M., Chen, R., Paris, R. B., Murray, A. S., Li, S.-H., Pagonis, V., Valla, P. G., and Herman, F. (2015). Radiation-induced growth and isothermal decay of infrared-stimulated luminescence from feldspar. *Radiation Measurements* **81,** 224-231.

Hansen, V., Murray, A., Buylaert, J.-P., Yeo, E.-Y., and Thomsen, K. (2015). A new irradiated quartz for beta source calibration. *Radiation Measurements* **81,** 123-127.

Huot, S., Frouin, M., and Lamothe, M. (2015). Evidence of shallow TL peak contributions in infrared radiofluorescence. *Radiation Measurements* **81,** 237-241.

Jain, M., Sohbati, R., Guralnik, B., Murray, A. S., Kook, M., Lapp, T., Prasad, A. K., Thomsen, K. J., and Buylaert, J. P. (2015). Kinetics of infrared stimulated luminescence from feldspars. *Radiation Measurements* **81,** 242-250.

Kijek, N., and Chruścińska, A. (2015). Equivalent dose of quartz originating from ceramics obtained by OSL SAR method – Tests of protocol parameters. *Radiation Measurements* **81,** 128-133.

Kim, K. B., and Hong, D. G. (2015). Analytical investigations of thermoluminescence glow curve on quartz for luminescence dating. *Radiation Measurements* **81,** 232-236.

Kook, M., Lapp, T., Murray, A. S., Thomsen, K. J., and Jain, M. (2015). A luminescence imaging system for the routine measurement of single-grain OSL dose distributions. *Radiation Measurements* **81,** 171-177.

Lapp, T., Kook, M., Murray, A. S., Thomsen, K. J., Buylaert, J. P., and Jain, M. (2015). A new luminescence detection and stimulation head for the Risø TL/OSL reader. *Radiation Measurements* **81,** 178-184.

Lomax, J., Mittelstraß, D., Kreutzer, S., and Fuchs, M. (2015). OSL, TL and IRSL emission spectra of sedimentary quartz and feldspar samples. *Radiation Measurements* **81,** 251-256.

Martin, L., Mercier, N., Incerti, S., Lefrais, Y., Pecheyran, C., Guérin, G., Jarry, M., Bruxelles, L., Bon, F., and Pallier, C. (2015). Dosimetric study of sediments at the beta dose rate scale: Characterization and modelization with the DosiVox software. *Radiation Measurements* **81,** 134-141.

Meriç, N., Yüce, Ü. R., Şahiner, E., Damianidis, A., and Polymeris, G. S. (2015). Dose response and fading studies on de-proteinated tooth enamel after de-convolution using the sum of general order kinetics and a component for tunnelling recombination. *Radiation Measurements* **81,** 257-261.

Moska, P., Jary, Z., Adamiec, G., and Bluszcz, A. (2015). OSL chronostratigraphy of a loess-palaeosol sequence in Złota using quartz and polymineral fine grains. *Radiation Measurements* **81,** 23-31.

Murray, A., Buylaert, J.-P., and Thiel, C. (2015). A luminescence dating intercomparison based on a Danish beach-ridge sand. *Radiation Measurements* **81,** 32-38.

Nelson, M. S., and Rittenour, T. M. (2015). Using grain-size characteristics to model soil water content: Application to dose-rate calculation for luminescence dating. *Radiation Measurements* **81,** 142-149.

Pagonis, V., and Chen, R. (2015). Monte Carlo simulations of TL and OSL in nanodosimetric materials and feldspars. *Radiation Measurements* **81,** 262-269.

Polymeris, G. S., Şahiner, E., Meriç, N., and Kitis, G. (2015). Thermal assistance in TA – OSL signals of feldspar and polymineral samples; comparison with the case of pure quartz. *Radiation Measurements* **81,** 270-274.

Qin, J., Chen, J., Valla, P. G., Herman, F., and Li, K. (2015). Estimating rock cooling rates by using multiple luminescence thermochronometers. *Radiation Measurements* **81,** 85-91.

Reimann, T., Ankjærgaard, C., and Wallinga, J. (2015). Testing the potential of a transferred IRSL (T-IRSL) feldspar signal for luminescence dating. *Radiation Measurements* **81,** 275-281.

Schmidt, C., Friedrich, J., and Zöller, L. (2015). Thermochronometry using red TL of quartz? – Numerical simulation and observations from in-situ drill-hole samples. *Radiation Measurements* **81,** 98-103.

Tang, S.-L., and Li, S.-H. (2015). Low temperature thermochronology using thermoluminescence signals from quartz. *Radiation Measurements* **81,** 92-97.

Thomsen, K. J., Kook, M., Murray, A. S., Jain, M., and Lapp, T. (2015). Single-grain results from an EMCCD-based imaging system. *Radiation Measurements* **81,** 185-191.

Timar-Gabor, A., Constantin, D., Buylaert, J. P., Jain, M., Murray, A. S., and Wintle, A. G. (2015). Fundamental investigations of natural and laboratory generated SAR dose response curves for quartz OSL in the high dose range. *Radiation Measurements* **81,** 150-156.

Tissoux, H., Voinchet, P., Lacquement, F., and Despriée, J. (2015). ESR as a method for the characterization of alluvial sediments. *Radiation Measurements* **81,** 2-8.

Tsukamoto, S., Toyoda, S., Tani, A., and Oppermann, F. (2015). Single aliquot regenerative dose method for ESR dating using X-ray irradiation and preheat. *Radiation Measurements* **81,** 9-15.

Wu, T.-S., Jain, M., Guralnik, B., Murray, A. S., and Chen, Y.-G. (2015). Luminescence characteristics of quartz from Hsuehshan Range (Central Taiwan) and implications for thermochronometry. *Radiation Measurements* **81,** 104-109.

Zink, A. J. C. (2015). Bayesian analysis of luminescence measurements. *Radiation Measurements* **81,** 71-77.

Zular, A., Sawakuchi, A. O., Guedes, C. C. F., and Giannini, P. C. F. (2015). Attaining provenance proxies from OSL and TL sensitivities: Coupling with grain size and heavy minerals data from southern Brazilian coastal sediments. *Radiation Measurements* **81,** 39-45.

Reviews, encyclopaedias and publications of more general interest related to dosimetric dating

Bahain, J. J., Falguères, C., Shao, Q., Tombret, O., Duval, M., and Dolo, J. M. (2015). ESR/U-series dating of fossil teeth: A useful tool to estimate the reworking state of the archaeological layers? *Quaternaire* **26,** 213-223.

Chaudhary, S. (2015). Optically Stimulated Luminescence (OSL) Dating of Sediments from Himalaya. *Journal of the Indian Institute of Science* **95,** 135-145.

Chauhan, N. (2014). Luminescence dating: Basic approach to geochronology. *Defect and Diffusion Forum* **347,** 111-137.

Duval, M. (2014). Dating fossil teeth by electron paramagnetic resonance: How is that possible? *Spectroscopy Europe* **26,** 6-13.

Feathers, J. K., Zedeño, M. N., Todd, L. C., and Aaberg, S. (2015). Dating Stone Alignments by Luminescence. *Advances in Archaeological Practice* **3,** 378-396.

Gray, H. J., Mahan, S. A., Rittenour, T., and Nelson, M. (2015). Guide to luminescence dating techniques and their applications for paleoseismic research. *In* "Basin and Range Province Seismic Hazards Summit III." (W. R. Lund, Ed.). Utah Geological Survey Miscellaneous Publication.

Jones, A. F., Macklin, M. G., and Benito, G. (2015). Meta-analysis of Holocene fluvial sedimentary archives: A methodological primer. *Catena* **130,** 3-12.

Liritzis, I., and Droseros, N. (2015). Light emitting diodes and optically stimulated luminescence dating in archaeology: An overview. *Mediterranean Archaeology and Archaeometry* **15,** 277-291.

Lowe, J., and Walker, M. (2015). Measuring Quaternary time: A 50-year perspective. *Journal of Quaternary Science* **30,** 104-113.

Lund, A., and Shiotani, M. (2014). "Applications of EPR in radiation research." Springer, Cham.

Munyikwa, K. (2014). Luminescence Chronology. *In* "Geochronology - Methods and Case Studies." (N.-A. Morner, Ed.), pp. 31-71. InTech.

Nelson, M. S., Gray, H. J., Johnson, J. A., Rittenour, T. M., Feathers, J. K., and Mahan, S. A. (2015). User Guide for Luminescence Sampling in Archaeological and Geological Contexts. *Advances in Archaeological Practice* **3,** 166-177.

Richter, D., and Wagner, G. A. (2014). Chronometric Methods in Paleoanthropology. *In* "Handbook of Paleoanthropology." (W. Henke, and I. Tattersall, Eds.), pp. 317-350. Springer Berlin Heidelberg.

Roberts, R. G., and Lian, O. B. (2015). DATING TECHNIQUES: Illuminating the past. *Nature* **520,** 438-439.

Sunta, C. (2015). Unravelling thermoluminescence. *In* "Springer Series in Materials Science." Springer, New Delhi.

Tschinkel, W. R., Rink, W. J., and Kwapich, C. L. (2015). Sequential Subterranean Transport of Excavated Sand and Foraged Seeds in Nests of the Harvester Ant, *Pogonomyrmex badius*. *PLoS ONE* **10,** e0139922.

Wintle, A. G. (2014). Luminescence Dating Methods. *In* "Treatise on Geochemistry (Second Edition)." (H. D. Holland, and K. K. Turekian, Eds.), pp. 17-35. Elsevier, Oxford.

Encyclopedia of Scientific Dating Methods

Rink, W. J., and Thompson, J. W. (2015). Encyclopedia of Scientific Dating Methods. *In* "Encyclopedia of Earth Sciences Series." (C. W. Finkl, Ed.). Springer, Dordrecht.

Adamiec, G. (2015). Radiation Dose Rate. 658-660.

Bailiff, I. (2015). Luminescence, Pottery and Bricks. 481-485.

DeWitt, R. (2015). Luminescence, Martian Sediments. 478-481.

DeWitt, R. (2015). Radiation and Radioactivity. 660-666.

Duller, G. A. T. (2015). Luminescence, Glacial Sediments. 475-478.

Duller, G. A. T. (2015). Luminescence Dating. 390-404.

Duller, G. A. T. (2015). Luminescence, Biogenic Carbonates. 445-446.

Duval, M. (2015). Electron Spin Resonance (ESR) Dating of Fossil Tooth Enamel. 239-246.

Fattahi, M. (2015). Luminescence, Earthquake and Tectonic Activity. 456-460.

Feathers, J. (2015). Luminescence Dating of Archaeological Sediments. 404-409.

Guérin, G. (2015). Luminescence Dating, Dose Rates. 414-417.

Heaney, P. J. (2015). Quartz. 649-650.

Heimsath, A. (2015). Luminescence, Soils. 489-493.

Hendricks, R., and Hodson, A. (2015). Luminescence Dating, Shell-Rich Deposits. 431-435.

Jain, M. (2015). Feldspar, Infrared-Stimulated Luminescence. 279-284.

Keen-Zebert, A. (2015). Luminescence, Fluvial Sediments. 465-469.

Lamothe, M. (2015). Feldspars. 284-285.

Lang, A. (2015). Luminescence, Colluvial Sediments. 450-452.

Lauer, T. (2015). Radioluminescence (RL). 685-685.

Martini, M. (2015). Quartz Defects, Optically Stimulated Luminescence and Thermoluminescence. 650-656.

Mauz, B. (2015). Luminescence, Coastal Sediments. 446-450.

Richter, D. (2015). Luminescence, Flints and Stones. 460-465.

Rink, W. J., and Heaman, L. M. (2015). Radioactive Decay Constants: A Review. 666-669.

Roberts, H. (2015). Luminescence Dating, Deep-Sea Marine and Lacustrine. 409-414.

Roberts, H. (2015). Luminescence Dating, Loess. 425-430.

Roberts, R., and Jacobs, Z. (2015). Luminescence Dating, Single-Grain Dose Distribution. 435-440.

Schellmann, G., and Radtke, U. (2015). Electron Spin Resonance (ESR) Dating of Coral. 234-239.

Sears, D. G. (2015). Luminescence Dating, Meteorites. 430-431.

Skinner, A. (2015). Electron Spin Resonance (ESR) Dating, General Principles. 246-255.

Sohbati, R. (2015). Luminescence, Rock Surfaces. 485-488.

Telfer, M. (2015). Luminescence, Desert Dunes. 452-456.

Thompson, J. (2015). Band Structure. 81-81.

Thompson, J. (2015). Beta Counter. 82-82.

Thompson, J. (2015). Radiation Defect. 657-657.

Thomsen, K. (2015). Luminescence Dating, Instrumentation. 422-425.

Tooth, S. (2015). Luminescence, Geomorphological Processes. 470-475.

Tsukamoto, S. (2015). Luminescence, Volcanic Rocks. 493-495.

Wallinga, J., and Cunningham, A. (2015). Luminescence Dating, Uncertainties and Age Range. 440-445.

Zöller, L., and Wagner, G. (2015). Luminescence Dating, History. 417-422.

Conference Announcements: SSD 18

We are pleased to announce the 18th International Conference on Solid State Dosimetry, SSD18, which will be held in Munich, Germany, 3 July - 8 July, 2016.

This series of conferences began in 1965 at Stanford, USA, and since then has expanded its initial scope from luminescence dosimetry to the current variety of solid state processes and methods available for radiation dosimetry.

In 2016, the main topics of the conference will be:

- Basic physical processes
- Material characteristics
- Monitoring and detection
- Clinical dosimetry
- Dating and Dose reconstruction
- Instrumentation/detectors

A School on Solid State Dosimetry will be offered 29 June - 2 July, 2016. The School is intended for scientist who are new in the field and for those who like to deepen their knowledge.

The submission of abstracts for the 18th International Conference on Solid State Dosimetry is now possible. The Deadline for the submission of abstracts is

15 January 2016!

For more information on the conference, please visit the conference homepage

www.ssd18.org

We are looking forward to welcoming you to Munich, Germany!

Dr. Clemens Woda

Conference Announcements: NWLDW 11

The University of Nebraska-Lincoln is pleased to announce the

11th New World Luminescence Dating Workshop (NWLDW)
in Lincoln, Nebraska May 19-21, 2016.

Both poster and oral presentations are planned for Thursday May 19th and Friday May 20th.

We will also be offering an optional overnight field trip to the Nebraska Sand Hills and adjacent loess hills that will leave Lincoln Friday afternoon and return Saturday evening. We will visit several sites from the Sand Hills as well as thick loess deposits (> 20 meters) and perhaps needless to say, many of these sites have OSL chronologies.

Lincoln (population = ~250,000) is served by a small airport in town (LNK), and a larger airport (OMA) one hour drive away in Omaha (population = ~410,000). Shuttles are available for transport between Lincoln and Omaha, if needed. The meeting location and lodging accommodations have not yet been chosen, but we expect to keep costs in mind when choosing these venues.

Please share this first announcement with colleagues who may be interested and let us know if we should add someone to this mailing list. Also, if you could let Paul (phanson2@unl.edu) know approximately how many from your lab are expected to attend the meeting we would appreciate it.

Please let us know if you have any questions or comments and we look forward to seeing you in May!

Paul and Shannon

Book Announcements: Springer Encyclopedia

Note: Ancient TL does not endorse this product nor encourage readers to buy the book. However, we realize it will be a useful and interesting product to many in the luminescence and ESR community.

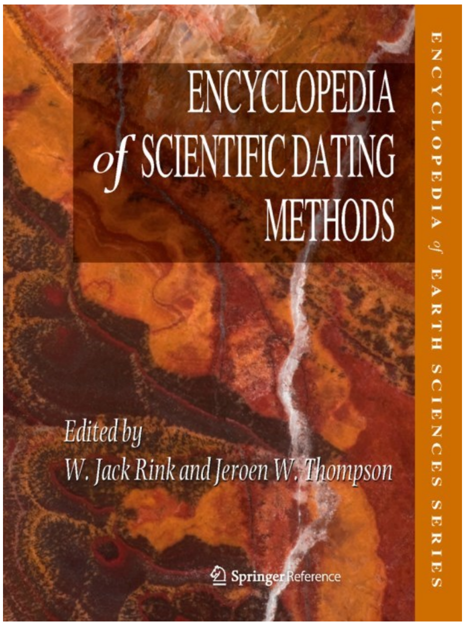

ENCYCLOPEDIA OF SCIENTIFIC DATING METHODS

Editors: **Rink**, W. Jack, **Thompson**, Jeroen W. (Eds.)

2015, Springer Netherlands, Dordrecht, 978p.

A list of ESR and luminescence related entries from this book can be found in the Bibliography of this issue (p. 49 - 50).

More information is available at www.springer.com/978-94-007-6303-6

From the publisher:

This volume provides an overview of (1) the physical and chemical foundations of dating methods and (2) the applications of dating methods in the geological sciences, biology, and archaeology, in almost 200 articles from over 200 international authors. It will serve as the most comprehensive treatise on widely accepted dating methods in the earth sciences and related fields. No other volume has a similar scope, in terms of methods and applications and particularly time range. Dating methods are used to determine the timing and rate of various processes, such as sedimentation (terrestrial and marine), tectonics, volcanism, geomorphological change, cooling rates, crystallization, fluid flow, glaciation, climate change and evolution. The volume includes applications in terrestrial and extraterrestrial settings, the burgeoning field of molecular-clock dating and topics in the intersection of earth sciences with forensics. The content covers a broad range of techniques and applications. All major accepted dating techniques are included, as well as all major datable materials.

Ancient TL

ISSN 0735-1348

Aims and Scope

Ancient TL is a journal devoted to Luminescence dating, Electron Spin Resonance (ESR) dating, and related techniques. It aims to publish papers dealing with experimental and theoretical results in this field, with a minimum of delay between submission and publication. Ancient TL also publishes a current bibliography, thesis abstracts, letters, and miscellaneous information, e.g., announcements for meetings.

Frequency

Two issues per annum in June and December

Submission of articles to Ancient TL

Ancient TL has a reviewing system in which direct dialogue is encouraged between reviewers and authors. For instructions to authors and information on how to submit to Ancient TL, please visit the website at:
http://www.ecu.edu/cs-cas/physics/ancient-timeline/ancient-tl1.cfm

Journal Enquiries

For enquiries please contact the editor:
Regina DeWitt, Department of Physics, East Carolina University, Howell Science Complex, 1000 E. 5th Street, Greenville, NC 27858, USA; Tel: +252-328-4980; Fax: +252-328-0753 (dewittr@ecu.edu)

Subscriptions to Ancient TL

Ancient TL Vol. 32 No.2 December 2014 was the last issue to be published in print. Past and current issues are available for download free of charge from the Ancient TL website:
http://www.ecu.edu/cs-cas/physics/ancient-timeline/ancient-tl5.cfm